# A MICROWAVE TOMOGRAPHY SYSTEM FOR FORESTRY APPLICATIONS

By

John James Doroshewitz

### A THESIS

Submitted to
Michigan State University
in partial fulfillment of the requirements
for the degree of

Electrical Engineering – Master of Science

2019

#### **ABSTRACT**

# A MICROWAVE TOMOGRAPHY SYSTEM FOR FORESTRY APPLICATIONS

By

#### John James Doroshewitz

A healthy urban forest is important for both human health and environmental quality. There is currently a lack of technology that can analyze living trees in their natural environment without destroying them.

This thesis presents a microwave tomography imaging system that is intended for use in several forestry applications. Recently, there has been an increased demand for imaging systems that do not use ionizing radiation but produce comparable accuracy and sensitivity to traditional imaging techniques. Microwave tomography is an emerging medical imaging research area that has rarely been used for anything besides human tissue imaging. The system described in this thesis was specifically designed for in vivo measurement of tree trunks and is one of the first of its kind.

The system forms an image by using frequency domain sampling over a wide bandwidth (1-5 GHz) and a ring of antennas. Microstrip monopole antennas specifically designed for use in microwave tomography systems are used and their design is presented. The system also uses a microwave switch matrix to switch between active pairs of antennas. The design of this switch matrix and the controlling software is also presented. Lastly, this thesis discusses the use of time reversal image reconstruction and the signal processing involved to create an image. Measured results of simple targets and preliminary measurements of tree trunk samples are both included.

#### **ACKNOWLEDGMENTS**

The first of many thanks has to go to my entire family. As the 13th member of my family to receive a Bachelor's degree from Michigan State and the second to receive a Master's, my destiny as a Spartan was written from birth. My parents, Jeri and John, and both my sisters, Jessica and Jackie, have been every kind of support that I could ask for during this process. Our family identifies as Spartans and it is truly a privilege to walk out of here with a second degree from the school I have always loved.

Of course, none of this is possible without the support, guidance, and pushing for excellence from my advisor, Dr. Jeffrey Nanzer. You care deeply about providing your students with the best opportunity and education possible. From the student design competition at APS as an undergrad up until the last day of graduate school you always pushed me to be the best engineer, scientist, and student that I could be.

I would also like to thank the rest of the faculty in the EMRG. Thank you to Dr. Ed Rothwell for first introducing me to electromagnetics and sparking my interest in this topic (big loops=bad, small loops=good) as well as for your guidance throughout both undergraduate and graduate school, you were always a trusted person to come to for advice on any topic. Thank you to Dr. Prem Chahal, the first EMRG professor that I did research under. Your experimental approach pushed my creativity and problem solving skills essential to research. And lastly, a thank you to Dr. Shanker Balasubramaniam, who was always available to ask theoretical EM questions or lecture me about something computational (although you are still disappointed in my first 280 exam score).

A big thank you to Chris Oakley for his help with the creation of the switch matrix, to Vinny Gjokaj and Brian Wright for their help in the antenna fabrication, and to Jason Merlo for his advice on the entire system design. Without you guys, the tomography system would still not be functional. Also, thank you to Saptarshi Mukherjee whose time reversal code and knowledge of image reconstruction was essential to this project.

This work was supported in part by the MSU Forestry Department, which gave me a unique opportunity to research a non-traditional area of electromagnetics. Thank you to Dr. David Macfarlane and Dr. Emily Huff for their support and advice on the forestry end of this work, and a huge thank you to Sam Clark of the Kellogg Experimental Forest who cut and prepared the wood samples for measurement. His work and willingness to drive the samples to East Lansing were vital to the success of this research. Thank you Dan Brown for allowing us to use his oven in the Forestry Wood Shop.

Lastly, I would like to thank the students of the EMRG. Without your friendship and support, this work would have never been possible.

# TABLE OF CONTENTS

LIST OF FIGURES	⁄ii
CHAPTER 1 INTRODUCTION	1 1 2 6
CHAPTER 2 TOMOGRAPHY SYSTEM DESIGN	10 12 17
CHAPTER 3 SIGNAL PROCESSING	24 24 25 26 27 28 30 32
CHAPTER 4 MEASURED RESULTS  4.1 Introduction	45 45 50 57 57
CHAPTER 5 CONCLUSION	76

APPENDICES	
APPENDIX A	PYTHON CODE TO TAKE DATA OFF HP8753D
	NETWORK ANALYZER 80
APPENDIX B	SWITCH MATRIX SCHEMATIC AND PART
	NUMBERS 87
APPENDIX C	NUCLEO CODE FOR CONTROLLING SWITCH
	MATRIX
APPENDIX D	MATLAB CODE TO PLACE ANTENNA LO-
	CATIONS
APPENDIX E	MATLAB CODE TO READ IN DATA 103
APPENDIX F	MATLAB CODE TO BACK PROPAGATE
	THE MEASURED DATA
	120
BIBLIOGRAPHY.	

# LIST OF FIGURES

1.1	Proposed mockup of the microwave tomography system intended to nondestructively evaluate tree trunks.	9
2.1	Realized microwave tomography system.	11
2.2	Ring of antennas used to perform microwave tomography on samples under testing.	11
2.3	Copper patterning of the monopole imaging antenna. Top copper (conductor) is in blue and bottom copper (ground plane) is in orange.	13
2.4	Fabricated antenna design on Rogers 3006. The conducting (left) and ground (right) planes are both shown.	14
2.5	Simulated and measured $S_{11}$ for the tomography measurement antennas.	15
2.6	Simulated (a) and measured (b) antenna patterns of the tomography measurement antennas.	16
2.7	Front side of the switch matrix.	18
2.8	Output ports on the rear of the switch matrix.	19
2.9	Schematic of switch tree to create a 2x16 switch matrix connecting Tx and Rx to any pair of ports 1-16. Switches labeled "A" are HMC270AMS8GE switches and those labeled "B" are HMC322ALP4E switches.	20
2.10	The Nucleo F411RE used to control the microwave switch matrix.	20
2.11	Inside of the switch matrix.	21
2.12	The Hewlett-Packard 8753D network analyzer and its controlling computer.	22
3.1	Test setup of a brass cylinder being imaged by the microwave to- mography system.	33

3.2	Measured frequency data in dB (top), zero padded and conjugate mirrored frequency data in dB (middle), and time domain pulse after the IFFT processing (bottom).	34
3.3	Time domain waveform of the measured empty environment.	35
3.4	Time domain waveform of the measured cylinder environment.	36
3.5	Time domain waveform of the measured empty environment subtracted from the measured cylinder environment.	37
3.6	Location of each of the antennas in the ring.	39
3.7	Sub-optimal reconstructed images of antennas 1 (a), 2 (b), 3 (c), and 4 (d) transmitting.	40
3.8	Sub-optimal reconstructed images of antennas 5 (a), 6 (b), 7 (c), and 8 (d) transmitting.	41
3.9	Sub-optimal reconstructed images of antennas 9 (a), 10 (b), 11 (c), and 12 (d) transmitting.	42
3.10	Sub-optimal reconstructed images of antennas 13 (a), 14 (b), 15 (c), and 16 (d) transmitting.	43
3.11	Total reconstructed image obtained from averaging the total energy in all 16 of the previous images, producing the brass cylinder shape.	44
4.1	Imaging results of a brass cylinder using pairwise measurement technique. (a) Measurement setup. (b) Reconstruction.	48
4.2	Imaging results of a plastic cylinder ( $\epsilon_r = 3.8$ ) using pairwise measurement technique. (a) Measurement setup. (b) Reconstruction.	49
4.3	Imaging results of a brass cylinder using the entire measurement system. (a) Measurement setup. (b) Reconstruction.	52
4.4	Imaging results of a plastic cylinder ( $\epsilon_r = 3.8$ ) using the entire measurement system. (a) Measurement setup. (b) Reconstruction.	53
4.5	Imaging results of a plastic square prism ( $\epsilon_r = 3.7$ ) using the entire measurement system. (a) Measurement setup. (b) Reconstruction.	55

4.6	Imaging results of a wood block using the entire measurement system. (a) Measurement setup. (b) Reconstruction.	56
4.7	Imaging results of a 1" diameter hole in a green basswood sample. The solid portion of the trunk (left (a)) was subtracted from the portion with the hole (right (a)). (b) Reconstruction.	59
4.8	Imaging results of a solid, green basswood sample. Two solid portions of the trunk (a) were subtracted from each other and only noise remains in the reconstructed image (b).	60
4.9	Imaging results of a 2" diameter hole in a green sugar maple sample. The solid portion of the trunk (left (a)) was subtracted from the portion with the hole (right (a)). (b) Reconstruction.	62
4.10	Imaging results of a solid, green sugar maple sample. Two solid portions of the trunk (a) were subtracted from each other and only noise remains in the reconstructed image (b).	63
4.11	Imaging results of a 2" diameter hole in a completely dried basswood sample. The solid portion of the trunk (left (a)) was subtracted from the portion with the hole (right (a)). (b) Reconstruction.	65
4.12	Imaging results of a 2" diameter hole in a completely dried sugar maple sample. The solid portion of the trunk (left (a)) was subtracted from the portion with the hole (right (a)). (b) Reconstruction.	66
4.13	Imaging results of a solid, fully dried basswood sample. Two solid portions of the trunk (a) were subtracted from each other and only noise remains in the reconstructed image (b).	67
4.14	Imaging results of a bolt added to a 1" hole in a completely dried basswood sample (a). (b) Reconstruction.	69
4.15	Imaging results of a bolt added to a 1" hole in a completely dried sugar maple sample (a). (b) Reconstruction.	70
4.16	Imaging results of a nail in a completely dried basswood sample. The solid portion of the trunk (right (a)) was subtracted from the portion with the nail (left (a)). (b) Reconstruction.	72
4.17	Imaging results of nails in a completely dried sugar maple sample. The solid portion of the trunk (left (a)) was subtracted from the portion with nails (right (a)). (b) Reconstruction.	73

4.18	Imaging results of a horizontal nail (illustrated by the red line) in a completely dried basswood sample. The solid portion of the trunk (right (a)) was subtracted from the portion with the nail (left (a)). (b) Reconstruction.	74
B.1	Switch matrix schematic.	87

#### **CHAPTER 1**

#### INTRODUCTION

## 1.1 Introduction

A microwave tomography system designed for imaging tree trunks using non-ionizing radiation is presented in this work. The realization of this system, including the hardware design and the signal processing is described in detail. Measured results for simple targets such as cylinders are presented as well as more complex targets, specifically tree trunk samples with simulated health issues in them. Tree health is the primary motivation for this work, discussed in Section 1.1.1.

## 1.1.1 Forestry Motivation

The primary focus of this work is creating a tomography system to image the inside of tree trunks without having to do any destructive evaluation to any components of the tree. As urban population continues to increase, the degradation of urban forests raises a concern regarding the impacts on human health and the overall quality of the environment. In 2012, Nowak and Greenfield wrote about the positive benefits of preserving a healthy urban tree canopy and its ability to mitigate some of the concerns [1]. Benefits of a healthy urban forest can yield positive effects on not only the environment, but also a community's economy due to the increase in energy efficiency [2] and its overall societal well-being by adding recreational opportunities and positive emotional effects [3].

Preserving a healthy urban forest requires an effective and efficient technique to evaluate the risk posed by each individual tree. The largest risk presented from trees in an urban area is stem and branch breakage or even whole-tree failure and toppling, often caused by wind and ice storms [4]. Currently, there are few options to properly evaluate the risk presented by a living, standing tree. Dahle et. al identifies several defects such as decay, cavities, cracks, splits, among others as indicators of trees at risk to fall. These characteristics are more qualitative and very difficult to translate into a reliable risk analysis procedure. They also discussed quantitative measurements such as aspect ratio (the ratio of branch diameter to stem diameter, with a large ratio being more at risk) or the angle of attachment of branches to trunk. Despite being numerical values, these measurements, again, are difficult to translate into a risk analysis [5]. Other than these parameters, there are no other accepted ways to determine the risk of failure of a living tree without destructively sampling the tree in some form.

## 1.1.2 Wood Imaging Review

In 2003, Bucur published a detailed review of the ability to image wood structures at a high resolution [6]. He organizes the imaging techniques into five main categories: ionizing radiation, thermal techniques, ultrasonic, nuclear magnetic resonance (NMR) imaging, and microwave techniques. Research done in this area and pros and cons of each technique is discussed:

**Ionizing Radiation** Ionizing radiation, such as x-ray or  $\gamma$ -ray radiation is one of the more traditional imaging techniques used in biological imaging. The use of x-ray radiation as an imaging technique was famously first discovered by Röntgen in 1895. The technology and its development continued through the 20th century as the most prominent medical imaging technique [7]. X-ray or  $\gamma$ -ray imaging has two major drawbacks: cost of system and health risks. Since the imaging system described in this work

is designed for the imaging of trees, cost is a major issue. The end-user of these products typically do not have huge budgets for imaging the inside of trees. Although there is a benefit of adding this imaging system, there is not a dire need for sophisticated imaging systems as compared to other places that would utilize x-ray imaging, i.e. hospitals. The second, more important, drawback is the fact that this radiation is ionizing. Using x-ray for imaging of living things ionizes the tissue which presents a major health risk [8]. Clearly, this goes against the goal of non-destructively evaluating the sample.

Despite these drawbacks, x-ray and  $\gamma$ -ray imaging have been used in previous application to image tree samples. Most work has been in the field of computed tomography (CT), which is preferable to conventional radiography for various reasons such as the lack of need for film, receiving data in near-real-time, improved calibration procedures, among numerous others [9]. In 1983, Onoe et. al created a portable x-ray CT scanner that could be used for measuring the annual rings inside of a living tree without destructively evaluating it (besides the unavoidable radiation exposure when using this imaging method) [10]. In 1989, Wagner et. al created a CT scanner that was able to scan logs for internal defects as they came into sawmills [11]. Rust also used x-ray CT to estimate the xylem, the tissue that transports water and minerals to the rest of the tree, of living trees [12].

Thermal Techniques Thermography is a term for techniques used that evaluate the sample using its surface temperature. Complex relationships are then drawn between the temperature distribution and the potential presence of different materials, defects, etc. Thermography is not an extensively studied field, largely due to these relationships. It relies on a largely exter-

nal physical property to predict internal properties and defects. Although this is a more quantitative measurement than things like decay and cavities discussed in the previous section, it still lacks concrete relationships between external and internal characteristics and relies on guesswork. In addition, thermography is a generally slow process and some of the most interesting results obtainable from this method need rapid capture times, which is difficult to achieve.

Some early work has been done in thermography to characterize living trees and their defects. Catena has published several works on using thermography to detect hidden cavities inside of the trunks of trees [13, 14]. Although this requires very large cavities to provide useful results, it can be very useful as these are the trees most at risk to fall and cause damage. Wyckhuyse et. al were able to show signs of wood decay and rotten wood using thermography by estimating moisture content of the samples. This is a step in the right direction towards characterizing the trees but in published literature it seems to be the maximum achievable result using this technique. Although it is useful for some low-level preliminary tests, there is still further demand for more accurate and robust systems.

Ultrasonic Ultrasonic imaging is similar to ionizing radiation imaging as it returns cross-sectional images by using transmission or reflection data from all directions surrounding the sample. In contrast to ionizing radiation, however, ultrasound uses high frequency pressure, or sound, waves for its characterization. The advantage of these pressure waves is they are completely safe and non-destructive to biological tissue when they are administered at low intensities. Ultrasound, however, does require direct contact between its transceivers and the sample in order to properly transmit the sound waves. In a forestry application this is not a huge issue as the

outside of the tree can easily be accessed and patient comfort is not a concern. These factors, as well as the generally low price of equipment [15], point towards ultrasound being a promising imaging technique. However in comparison with x-ray CT, ultrasound CT is inferior in both sensitivity and ability to specify inconsistencies [15].

In tree imaging, ultrasound has been used to test wood samples in various ways. In 1994, Biagi et. al used ultrasound to characterize wood poles and timber as it entered a sawmill [16]. Comino et. al performed a similar ultrasonic analysis but instead tested living trees in their natural state in order to detect internal decay and defects [17]. Socco et. al has showed over the course of several papers the feasibility of using ultrasonic tomography for imaging of living trees and has shown that there is ability to detect inconsistencies and decay, but there are limitations to its resolution and accuracy [18–20]. These fundamental limitations are the major reason why ultrasound is not the best option for tree imaging moving forward in research.

Nuclear Magnetic Resonance NMR has proven to be one of the most accurate and powerful characterization techniques developed to date. It uses a strong magnetic field to align the magnetic polarizations of the sample's nuclei and then applies a weak, oscillating magnetic field to the same sample. The response of the aligned nuclei is then measured and the sample is reconstructed from these measured fields [21]. This technique is very involved but it produces extremely accurate results on a relatively real-time basis. In addition, this magnetic resonance does not have any lasting effects on the nuclei so it is not harmful in any way to living tissue. The biggest deterrent to NMR is the cost of the technology. Since there is a demand in forestry applications for measurement equipment to be low-

cost, a consumer product using NMR is not feasible considering current technology.

Despite the high cost, there have been attempts to characterize trees using NMR in field tests. In 1997, Pearce et. al observed water contents in sycamore trees and used this information to be able to diagnose several conditions such as decayed wood, sooty bark disease, and various species of invasive fungi growing in the tree [22]. Merela et. al used NMR to diagnose wounded branch structures in beech trees by identifying areas with decreased moisture content as the tree cuts off water supply to damaged tissue [23]. This research proves to be a promising technique to give accurate and valuable diagnoses to trees but will continue to be unfeasible in most applications due to its high price.

Microwave techniques Microwave tomography is the focus of this work and its benefits and current uses will be discussed in detail Section 1.1.3. It has been studied very little for use in forestry applications prior to this work. There has only been one group that has published work for microwave applications in imaging tree. Pastorino et. al [24] and Boero et. al [25] both have worked on the imaging of the trunks of living trees using microwave tomography. They were able to show simulated and measured results using this technique. This is, to the author's knowledge, the first and only use of microwave tomography for forestry applications to date.

# 1.1.3 Microwave Tomography Review

Microwave tomography is an emerging imaging technique that is proving to be useful for analyzing complex structures, specifically those that contain dielectric inconsistencies inside of them. Using low to medium power frequencies in the

radio or microwave bands provides non-ionizing radiation that is a safe alternate to x-ray or  $\gamma$ -ray imaging. In addition, radio frequency components are cheaper and widely available in comparison to the ionizing radiation or NMR hardware. In terms of sensitivity and accuracy, early data suggests that microwave imaging is better than any of the other proposed methods [26]. Although thermography and ultrasound are cheap and portable methods, the advantages proposed by microwave tomography while still remaining cheap and portable makes it a vital area of research for future biological imaging advancements.

Since microwave tomography is a cheap, safe alternate to traditional imaging techniques, it has become of particular interest to the medical imaging field [27]. Specifically, researchers have attempted to create microwave tomography systems for breast imaging when screening for tumors or other signs leading to breast cancer [28]. Currently, the process involves yearly (or even more frequently in certain cases) x-ray examinations of the breasts, a process called mammography. Researchers have focused much of the effort on this specific image because it is a routine x-ray and it exposes tissue that is already at risk of developing cancer to more of the dangerous ionizing radiation. Whereas many other x-ray examinations are done only when necessary, a routine examination such as a mammogram screening is a logical candidate to be replaced by microwave tomography.

There has been many different uses of microwave tomography for imaging breast tissue. An interesting technique that combines microwave and ultrasound methods called thermoacoustic imaging. The thermoacoustic effect is a phenomenon that causes molecules to vibrate when exposed to heat or other microwave radiation [29]. This vibration, in turn, can be used as an ultrasonic signal to image a medium that was excited by microwave energy. This was of particular interest in the late 90s when microwave imaging was still a relatively

new topic. Kruger et. al [30, 31], Wang et. al [32], and Ku et. al [33], among many others, presented systems and measurements that demonstrate thermoacoustic imaging for breast tissue. There are also examples of using actual microwave tomography for imaging. Meaney et. al [34, 35], Souvorov, et. al [36], and Hagness et. al [37, 38] are some examples of researchers who created microwave simulations and systems to perform such measurements, among many others.

Microwave techniques are proving to be very promising in the area of medical imaging. One drawback, however, is many of the current methods proposed are computationally expensive. These systems rely on non-linear inversion methods to do their image reconstruction [39–41]. These techniques require large computing power, long computation times, or often both to successfully invert the problem and reconstruct an image. Although this is much less of a problem in a medical imaging scenario, where hospitals can store large clusters of computers in house to perform the expensive computations, this becomes a much bigger issue for forestry applications. In order to do in vivo imaging of tree trunks, a computationally cheap solution that can still provide near-real -time images must be created.

#### 1.1.4 Contributions of This Work

In this thesis, a frequency domain sampling microwave tomography system that utilizes time reversal, a less computationally expensive method than a full inverse problem, to perform its reconstruction is presented. This system uses specifically designed planar monopole antennas to perform its data collection, a microwave switch matrix to handle the switching between antennas, and a network analyzer to do its data collection. The system is designed for the intent to use in forestry applications. Unlike the methods that are described in

Section 1.1.2, this uses non-ionizing radiation and cheap components to create a reasonable solution for the forestry experts that would potentially be interested in this final product. In comparison to prior work, the tomography system presented here is a safer, cheaper, and more mobile alternative to image tree trunks.

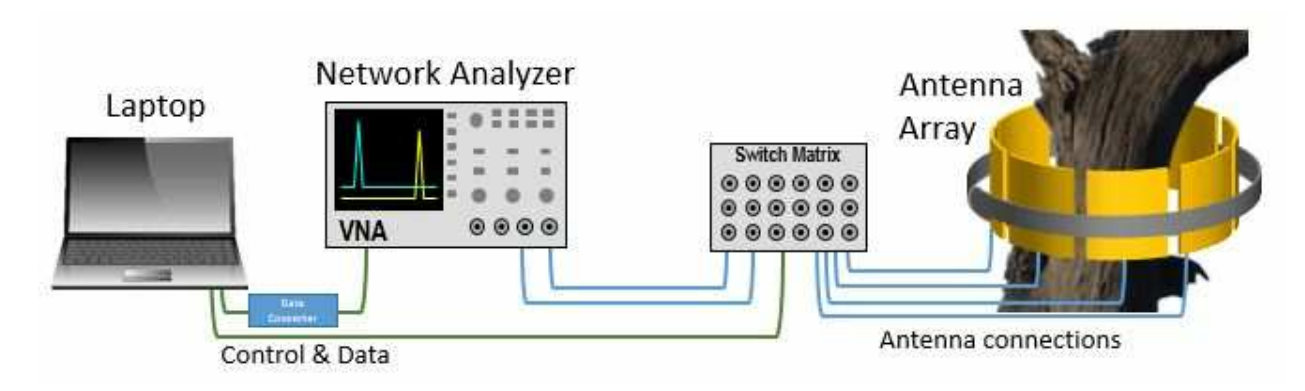


Figure 1.1 Proposed mockup of the microwave tomography system intended to nondestructively evaluate tree trunks.

The design process for the all hardware and software components included in this system, from why each specific method was used to fabrication and testing, is presented in the following chapters. Chapter 2 will cover the hardware design of the system. The design and fabrication of the monopole antennas, the creation of the switch matrix and its programming, and the transceiver used and its motivation are all discussed in this chapter. Chapter 3 will cover the software design of the system. The process of converting data from the frequency domain to the time domain, the time reversal simulation, and the image reconstruction process are included in this chapter. Chapter 4 will present many different measured results from the system. Measured results of both simple targets as well as preliminary measurements of actual tree trunks with simulated defects in them are presented to show the feasibility of this system as a low-cost, portable, near-real-time imaging system for in vivo measurement of tree trunks.

#### **CHAPTER 2**

#### TOMOGRAPHY SYSTEM DESIGN

## 2.1 Overview

This chapter will describe the microwave tomography system used for imaging of wood samples, seen in Fig. 2.1. A ring of antennas, seen in Fig. 2.2, is created that surround the sample under test (SUT) to collect data that will eventually be used to create an image, which is discussed in Chapter 3. In this work, the ring consists of 16 equidistantly spaced antennas that act as both a transmitter and receiver to measure the scattering off of the SUT. This ring is surrounded by microwave absorbing material to block the outside RF interference that could be present in the environment. Although this would not be available in the field testing environment, it helps give the best possible results for a first prototype of a system. Control of these antennas and the data collection is done through a computer connected to both a network analyzer and a microwave switch matrix. The antenna design and the design of the switch matrix will be described in this chapter while the code for the control of the network analyzer and the switch matrix can be seen in Appendices A and C, respectively.

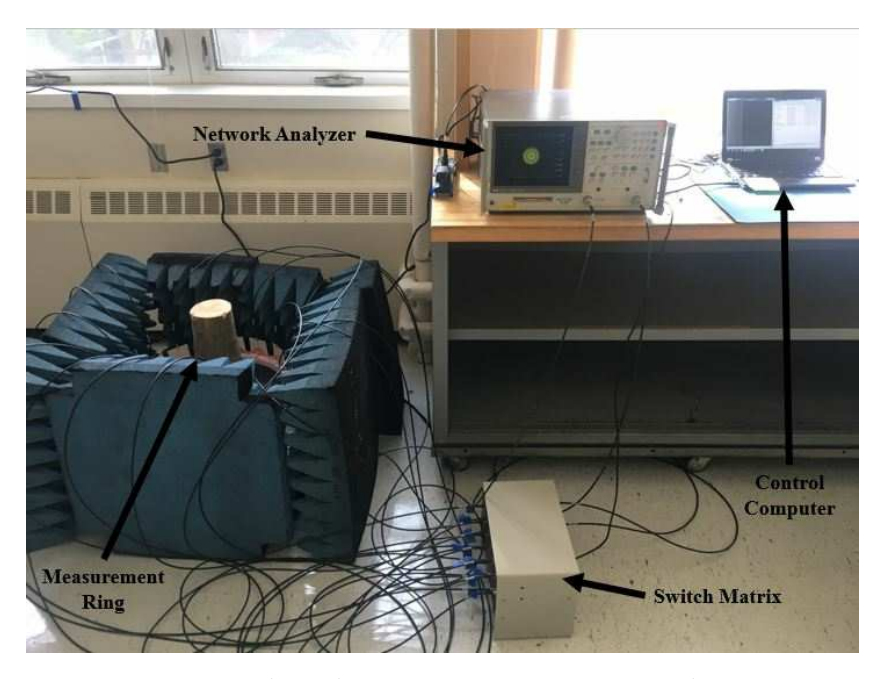


Figure 2.1 Realized microwave tomography system.



Figure 2.2 Ring of antennas used to perform microwave tomography on samples under testing.

# 2.2 Antenna Design

A major component of all microwave systems is the antenna used in the system. As electronic systems become increasingly more digital with the development of high speed digitizers, antennas will remain to be necessary for any wireless system, as a transition from a guided wave to a unbounded wave cannot be avoided until possibly very far in futuristic systems. In microwave tomography systems, it is popular to use antennas that are directional in their pattern in order to collect information from inside the ring and avoid any interference or noise from outside the ring. Due to space constraints in the ring of antennas, it is common to use directional planar antennas as opposed to a simple horn antenna. The most commonly used directional antenna design used in tomography is the Vivaldi, or tapered slot, antenna. This is a planar wideband antenna that creates a highly directive radiation pattern. This antenna was first designed by Gibson in 1979 [42] and improved by Gazit in 1988 [43]. Medical imaging using microwave tomography have utilized Vivaldi antennas in many different applications [44, 45]. Other directive planar antenna designs, such as the patch antenna [46, 47] or more complex designs such as the folded quasi self complementary antenna (FQSCA) [48] have been utilized in [49, 50].

The antennas used for this design are wideband planar monopole antennas often used for imaging. In contrast to what is discussed above, these antennas display more of a omnidirectional antenna pattern in the x-y plane. Non-directive antennas are less typical in the microwave tomography research field due to the collection of data from areas not in the center of the ring. In addition, there is increased coupling between the antennas if neighboring antennas have overlapping beams. Despite these drawbacks, prior research has been conducted using non-directive antennas. The most popular omnidirectional antenna used in all wireless applications, microwave tomography included, is the dipole

antenna [51] or its equivalent; a monopole antenna above a ground plane reflection [52, 53].

An omnidirectional radiation pattern was chosen for this application due to the use of time reversal imaging, discussed in detail in Chapter 3. This imaging process assumes that the antennas radiate in an omnidirectional pattern. In order to mimic this sitatuion as closely as possible, the pattern was chosen as such. This particular antenna design was specifically published for wideband imaging in circular imaging systems [54]. This antenna consists of a semi-circular patch antenna fed by a microstrip transmission line over a semi-circle of the same size on the rear side that acts as a partial ground plane, which can be seen in Fig. 2.3. This antenna acts as a monopole that creates a dipole-like antenna with its image above the ground plane.

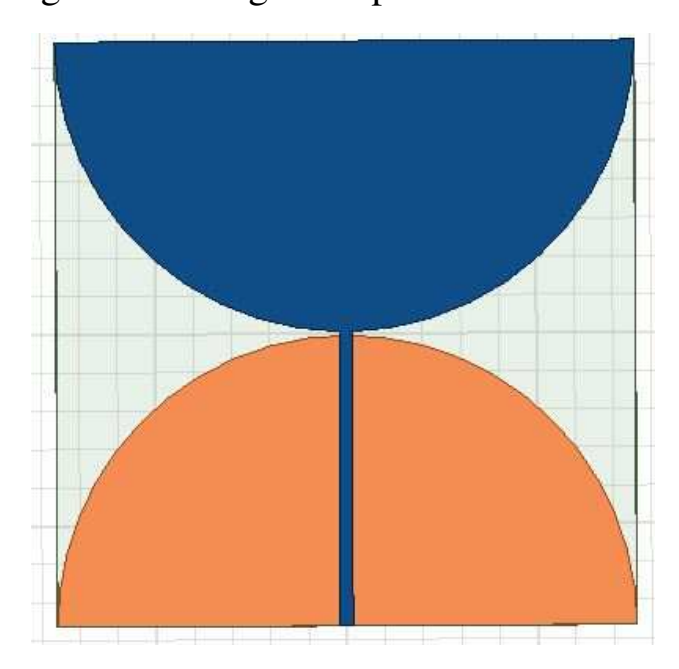


Figure 2.3 Copper patterning of the monopole imaging antenna. Top copper (conductor) is in blue and bottom copper (ground plane) is in orange.

The antenna design was modified and optimized using Ansys HFSS. Once final dimensions were optimized, 16 of the antennas were fabricated and tested. In order to limit the physical size of the antennas, they were fabricated on Rogers

3006 dielectric board, which has a moderately high dielectric constant ( $\epsilon_r$  = 6.15). A board height of 1.27 mm was chosen and end-launch SMA connectors were added to the edge of the antenna feed line. In order to compensate for the gap of the connector being larger than the thickness of the substrate, copper tape was added to increase the stability of the connection. The copper material was cut on a CNC milling machine and the excess copper removed, leaving only the pattern behind. An image of the front and rear of the fabricated antennas can be seen in Fig. 2.4.

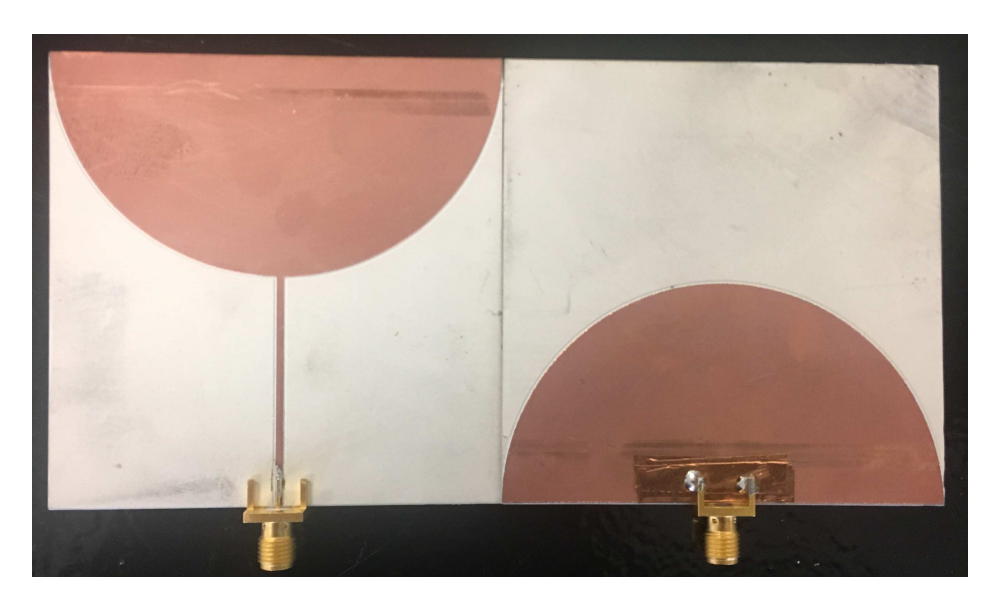


Figure 2.4 Fabricated antenna design on Rogers 3006. The conducting (left) and ground (right) planes are both shown.

The simulated and measured  $S_{11}$  and antenna patterns can be seen in Figs. 2.5 and 2.6, respectively. Nearly the entire bandwidth of 1 to 5 GHz measured below -10 dB, besides the lowest frequencies and a small frequency range between 3 and 3.5 GHz. The resonance ship upwards around 1 GHz accounts for the lack of gain at that frequency in the pattern. Besides this difference in the 1 GHz pattern, the antenna trends well with simulation and shows the dipole-like characteristics that were targeted in this design.

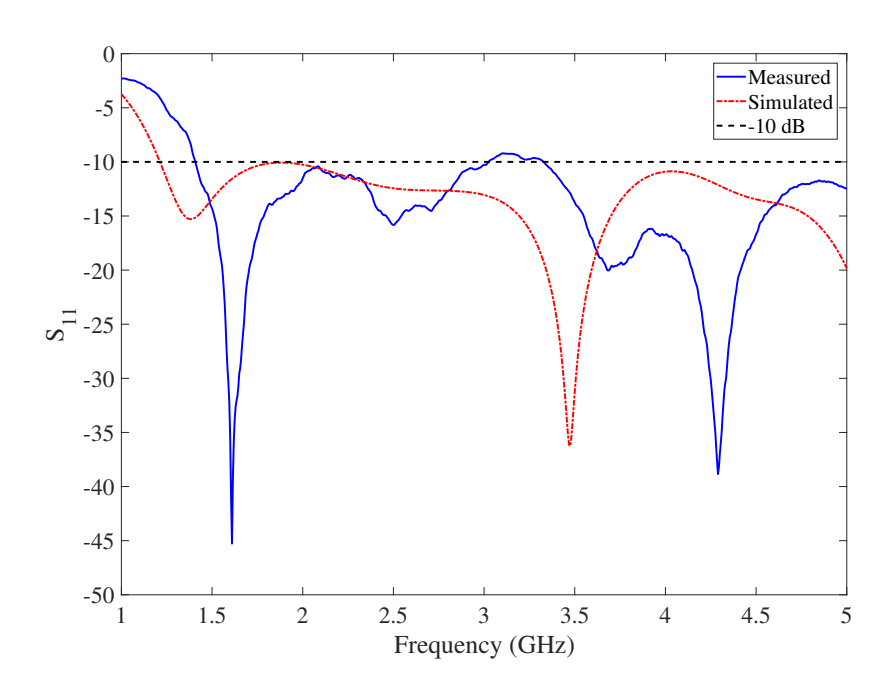


Figure 2.5 Simulated and measured  $S_{11}$  for the tomography measurement antennas.

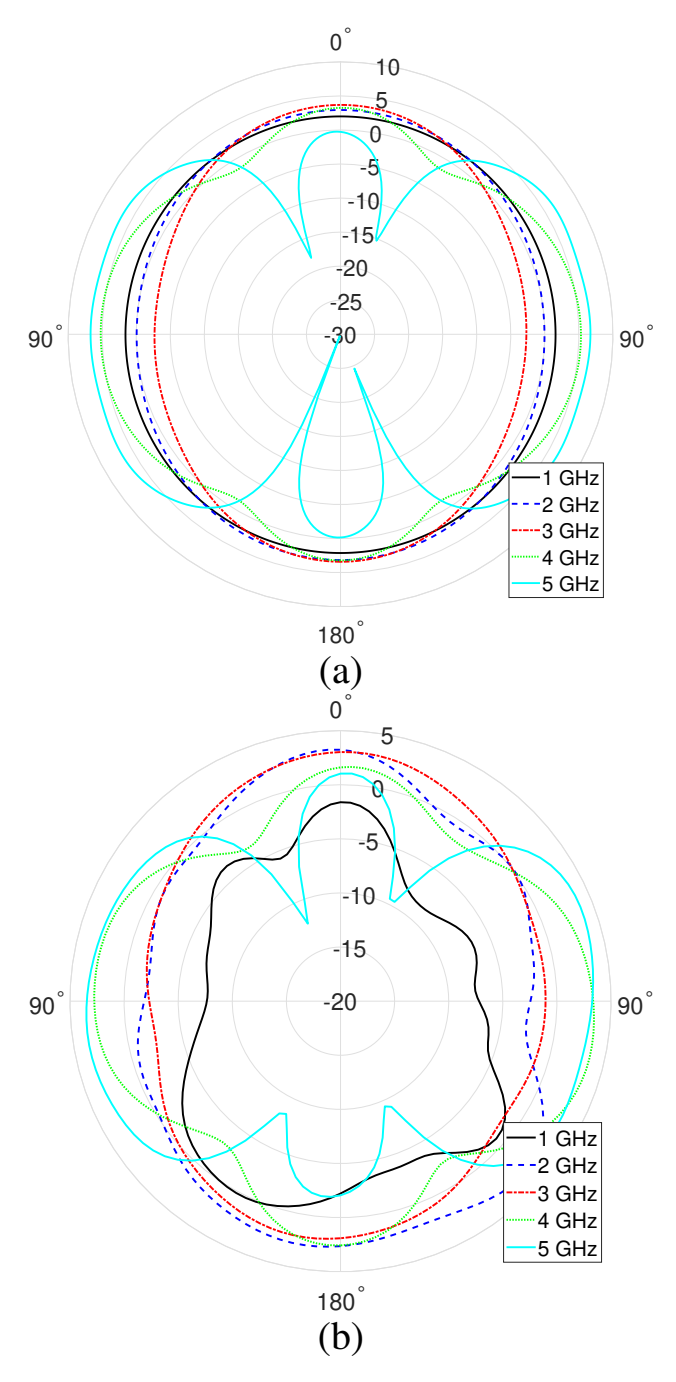


Figure 2.6 Simulated (a) and measured (b) antenna patterns of the tomography measurement antennas.

# 2.3 Switch Matrix Design

Another important piece of this system design is the microwave switch matrix. This switch matrix consists of 22 switches, 4 single pole eight throw (SP8T) switches and 18 single pole double throw (SPDT) switches, that can quickly connect any of the 16 antennas to any of the other remaining 15. On one side of the housing box has two ports, one for transmit and one for receive, as seen in Fig. 2.7, and the other side has the 16 ports for each of the outputs to the antennas, seen in Fig. 2.8. The switch tree that connects these two sides can be seen in Fig. 2.9. Each signal route passes through three switches from transmit to antenna and three from antenna to receive. In order to help mitigate some of this insertion loss from the three switches, a Mini-Circuits ZX60-V82+ amplifier was added to the transmit stage before the signal is passed through any switch. Since the switching would be happening many times and to create the most robust switch matrix as possible, high speed solid state switches were selected. The SP8T switches used are HMC322ALP4E and the SPDT switches used are HMC270AMS8GE.

These switches have many DC voltage control lines that are used to control the logic. To properly handle these voltages, a PCB was designed, fabricated, and populated with surface mount devices. The schematic and part numbers of this PCB can be referenced in Appendix B. This circuit board is controlled through a Nucleo F411RE development board from STMicroelectronics, seen in Fig. 2.10. The Nucleo F411RE runs C++ code on the Mbed platform. The Nucleo is connected to a controlling laptop through a USB hub, allowing for easy control of the connected ports of the switch matrix. The computer connects with the Nucleo through a serial connection and simply accepts two hexadecimal characters, first one for transmit connection and second one for receive connection, as its input for control. The input hexadecimal characters

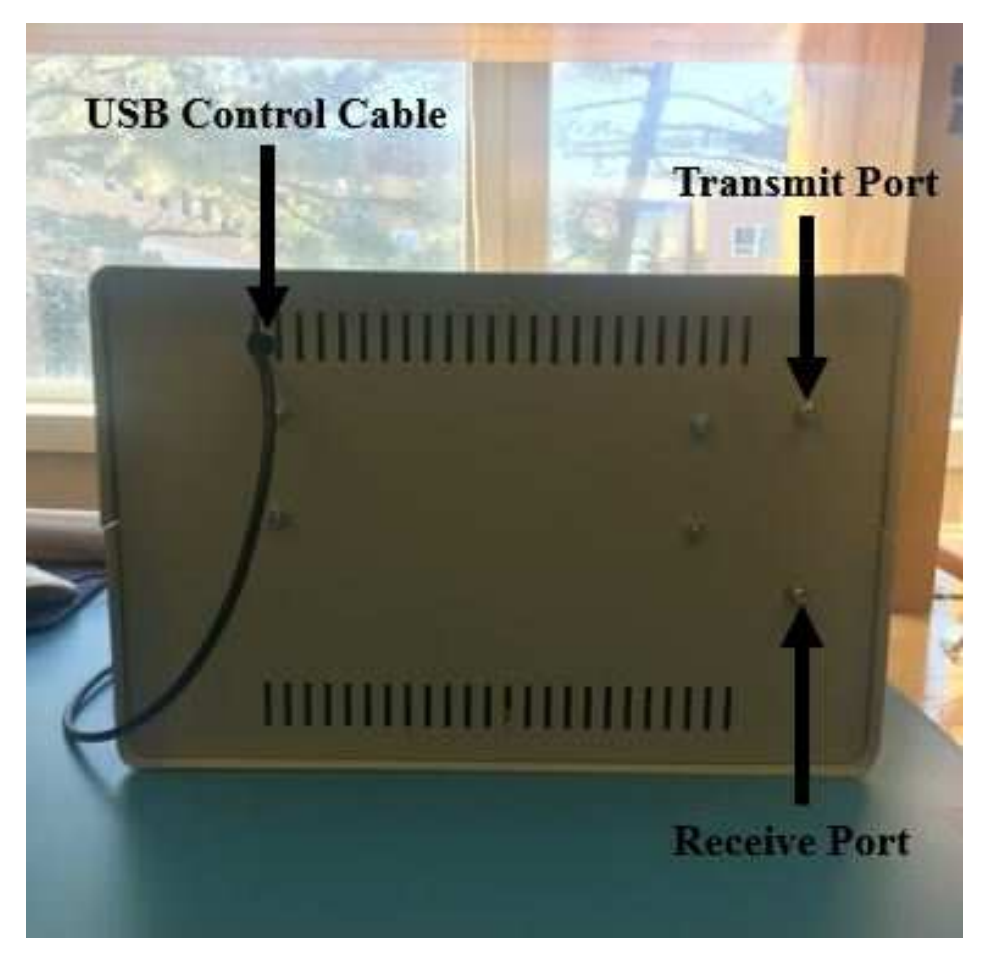


Figure 2.7 Front side of the switch matrix.

0-9 correspond with ports 1-10 and characters A-F correspond with ports 11-16, all respectively. The C++ code installed on the Nucleo can be seen in Appendix C. The complex arrangement of the inside of this system can be seen in Fig. 2.11.

Overall, there are 240 measurements that are recorded per scan, 16 antennas paired with each of the other 15. In order to do a complete scan of a sample, the system takes approximately 18.5 minutes, providing near-real-time imaging of the sample.

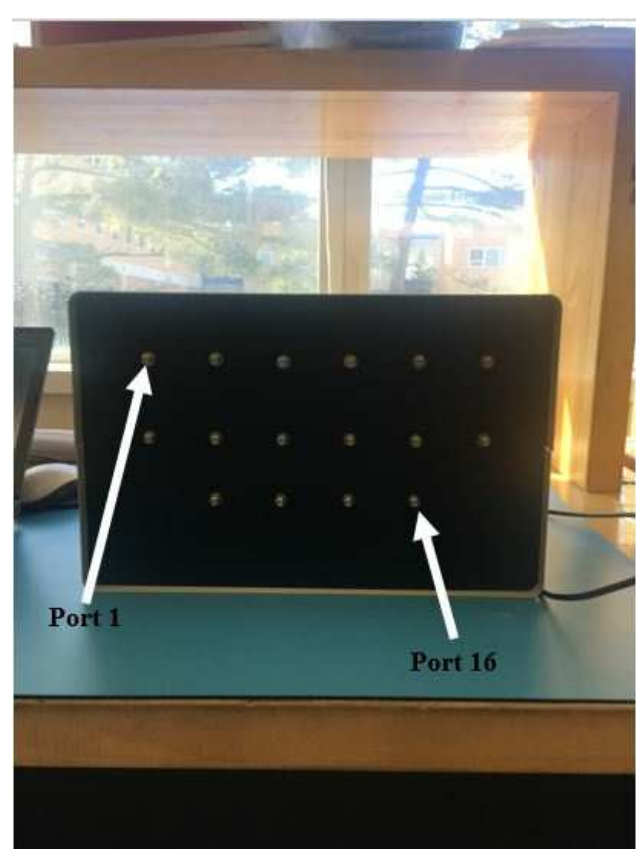


Figure 2.8 Output ports on the rear of the switch matrix.

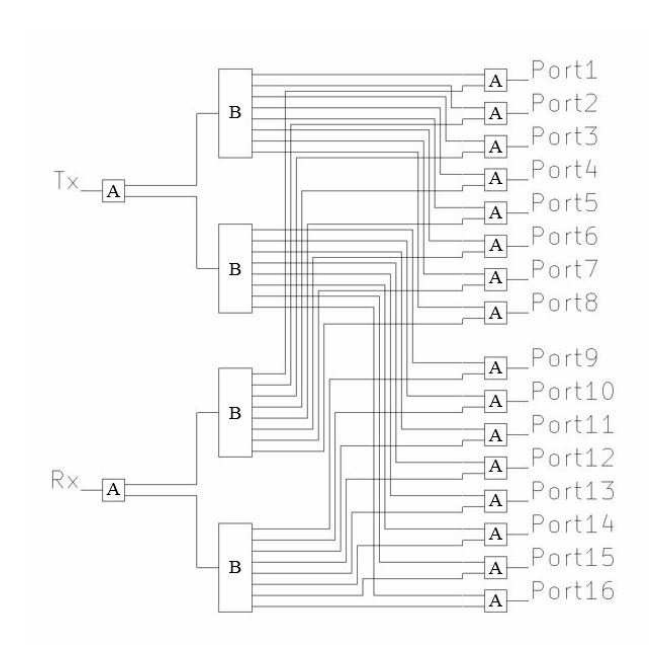


Figure 2.9 Schematic of switch tree to create a 2x16 switch matrix connecting Tx and Rx to any pair of ports 1-16. Switches labeled "A" are HMC270AMS8GE switches and those labeled "B" are HMC322ALP4E switches.



Figure 2.10 The Nucleo F411RE used to control the microwave switch matrix.

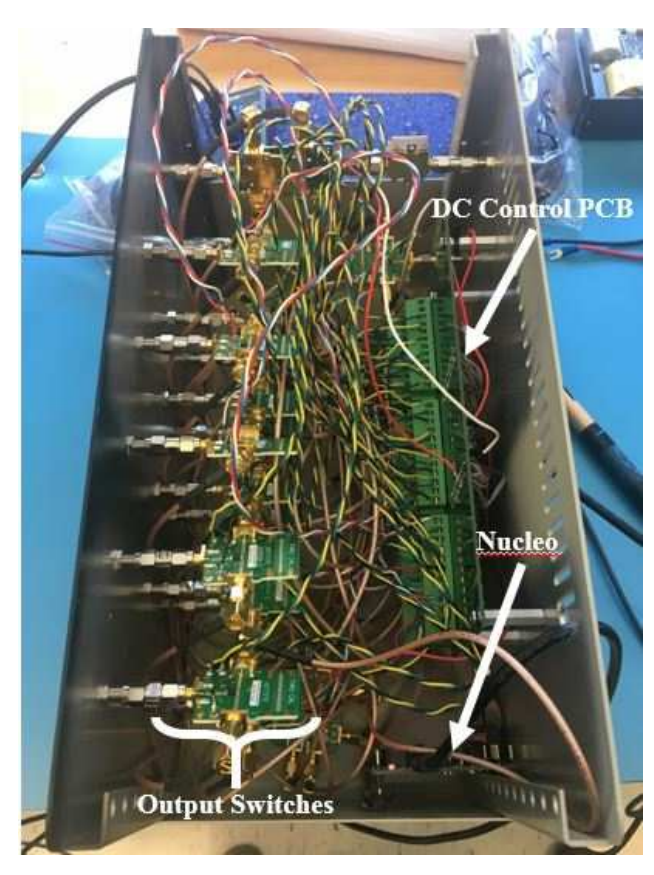


Figure 2.11 Inside of the switch matrix.

## 2.4 Transceiver

For this research, a Hewlett-Packard 8753D network analyzer, seen in Fig. 2.12, is used. A network analyzer measures the scattering parameters of a one or two port network. This analyzer also has the ability to collect the complex scattering parameters of the network it is measuring. This network analyzer is connected to the switch matrix discussed in the previous section that connects it to each of the 16 antennas in the ring. This network analyzer measures  $S_{21}$  for each pair of antennas, recording  $S_{ij}$  (i = [1, 16]; j = [1, 16];  $i \neq j$ ) for the SUT. Data is collected from 1 to 5 GHz over 1601 points, yielding a step size of 2.5 MHz. The decision to use these sampling parameters and its consequences will be further discussed in Chapter 3.

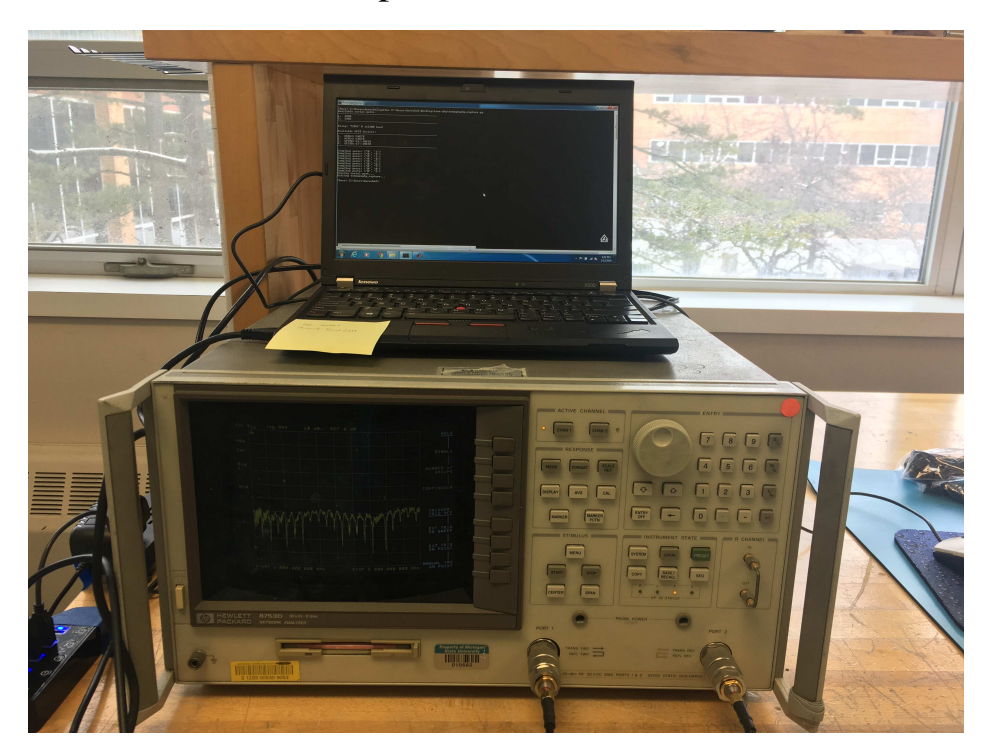


Figure 2.12 The Hewlett-Packard 8753D network analyzer and its controlling computer.

Using a network analyzer for the measurement is an important factor in future iterations of this system. The goal of the final product is to have a

low-cost, portable measurement system for use in field testing of tree trunks. Using a frequency domain measurement of scattering parameters with a network analyzer allows for the implementation of a software defined radio (SDR). Using an SDR to sweep across a wide bandwidth as an alternative to an expensive network analyzer can provide a cheap, portable alternative to the current system design. Although SDRs are generally instantaneously narrowband, they have a wide operational bandwidth so the wide frequency sweep can be done in a similar manner to the network analyzer.

SDRs have only recently become an area of research in electrical engineering. In 2006, Svensson introduced the idea of using generic hardware that can be programmed in software to manage radio standards across a wide bandwidth [55]. In 2009, Welch et. al explored the possibility of using SDRs as an affordable alternate for radio signal processing instrumentation but acknowledged its shortcomings in the cleanliness of the signal [56]. Regardless, they described SDRs as a cheap and fairly reliable alternative to expensive instrumentation, especially in classroom or academic research areas where budgets are generally tight. More recent research has involved creating special receivers that help create a more reliable receiver across a wide bandwidth [57–59], which will be key to this particular application. It was not until 2016 until Helaly and Adnani explored the possibility of using a software defined radio for spectrum analysis in [60] and [61]. Also in 2016, Marimuthu et. al used an SDR to do basic medical imaging using a wideband sweep similar to the future system proposed in this work [62]. Stancombe is continuing to advance this SDR imaging technology to develop a portable head imaging system in 2019 [63]. In the near future, SDR technology and research will be expanded greatly and its use as a reliable alternative to expensive testing equipment will become a feasible possibility for the tomography system.

#### **CHAPTER 3**

#### SIGNAL PROCESSING

### 3.1 Overview

A major component of the microwave tomography system is the processing of the measured signals to create a reconstructed image. There are three primary sections of signal processing involved in converting measured transmission coefficients in the frequency domain to a coherent reconstructed 2D image: frequency to time domain conversion, time reversal simulation, and energy calculation and reconstruction. Each of these three procedures will be described in detail in this chapter. The MATLAB code for initializing the system setup, preparing the measured data from the frequency to the time domain, and the back propagation and energy calculation can be seen in Appendices D, E, and F, respectively.

# 3.2 Frequency Domain Motivation

The microwave tomography system collects data in the frequency domain in terms of the transmission coefficients  $S_{ij}$  (i = [1, 16]; j = [1, 16];  $i \neq j$ ). This creates a 16 by 16 scattering parameter matrix that contains all the transmission coefficients of each possible pair of antennas. In this case, the reflection coefficients, which are found on the diagonal of the scattering parameter matrix, are set to 0. Although reflection coefficients could possibly be used, this is not traditional in time reversal simulations which will be discussed in the following section.

In order to prepare this data for this time reversal simulation and reconstruction, time domain data must be obtained. Although data could also be obtained in the time domain thus avoiding this step, this requires precise timing equipment and a high speed oscilloscope. In addition, the use of an microwave switch matrix for this system would also add complexity to the analysis. Individual line length and signal paths are not uniform through this switch matrix and each channel would require individual characterization. As an alternative, the data is collected on a network analyzer in steady state and transformed into the time domain. The steady state measurement also generally provides a higher signal-to-noise ratio (SNR).

## **3.2.1** Frequency to Time Domain Conversion

The frequency domain information that is obtained from the network analyzer or SDR must be converted from the frequency domain to the time domain. This section will follow the code included in Appendix E. The previously mentioned 16 by 16 scattering parameter matrix is measured over 1601 frequency points from 1 to 5 GHz, with a frequency step size of 2.5 MHz. In order to obtain strictly real time domain waveforms like those that would be obtained from an oscilloscope, frequency data must be conjugate matched across the zero frequency axis.

First, zeros are added to each S-parameter from 0 to 1 GHz at the same frequency sampling rate used for the collected data. Once the frequency domain is populated from 0 to 5 GHz, this information is reflected over the DC axis and conjugated. This creates frequency domain information from -5 to 5 GHz, containing 4001 points, 2000 points on each side of the DC axis and one point for the DC frequency. From this point, an inverse fast Fourier transform (IFFT) is applied to the data, creating the strictly real time domain waveform. Since the frequency domain waveform was taken across a wide bandwidth, this leads to a narrowband pulse in the time domain.

The last step is to cut the information down to reduce computation time. This process produces a 4001 time step pulse, the vast majority of which are very close to zero. It has been tested and shown that using only 250 time steps where the actual pulses occur in the waveform provides a nearly if not completely identical reconstruction as using the entire waveform and it drastically cuts down on computation time and resources. After the creation of these time domain pulses from the frequency sampled data, the data is ready for the time reversal simulation which will be described in the next section.

In order to create the reconstructed images, a subtraction of these time waveforms is necessary. The scattered field can be calculated using these waveforms by using the equation

$$E^{scat} = E^{tot} - E^{inc} (3.1)$$

where  $E^{scat}$ ,  $E^{tot}$ , and  $E^{inc}$  represent the scattered, total, and incident electric fields, respectively. The total field uses the measured data from the environment with the object being tested inside of it and the incident field is a measurement of the empty field. Subtracting these two fields leaves only the scattered field in the simulation. This, in theory, will create an image of the scatterer with the additional environmental noise subtracted from the empty field calibration step.

# 3.3 Time Reversal Simulation

For this imaging application, the imaging technique selected is time reversal. This theory is well documented as a localization technique for imaging environments in radar applications. The following sections will discuss both its theory and uses in many different microwave and ultrasonic applications followed by its implementation in the microwave tomography system discussed

in this thesis.

### **3.3.1 History**

The first mentioning of time reversal in literature as a electrical engineering concept was in 1957 from Bogert of Bell Labs [64]. It was originally presented as a concept to mitigate phase distortion in communication signals to increase quality of transmission. This technique was used to create digital filters with zero phase shift added to the signal. A similar idea was presented in 1965 using the concept of time reversal as a digital filter [65]. For about 30 years from this publication, the concept of time reversal was used solely for this purpose. It was not used as an imaging technique until much later.

Time reversal technique evolved in the late 1980s and early 1990s as a method for focusing fields to locate targets in an environment as opposed to strictly a filtering technique for phase distortion [66–68]. These works, however, used ultrasonic waves to perform their imaging. It was not until 2004 when Lerosey et al. demonstrated the first use of time reversal focusing using electromagnetic radiation [69]. They used wideband microwave radiation at a central frequency of 2.45 GHz to focus convergence of the waves back to the initial source. Since then, time reversal of electromagnetic fields converging to their source has become the main focus of research. Although there is still some recent use of time reversal at microwave frequencies for delay spread compression of communication signals (e.g. [70]) as it was originally introduced by Bogert, its use as a back propagation of waves to their source has proven to be a much more useful tool in modern research.

The major use of time reversal in recent research has used this back propagation of electromagnetic waves for radar applications and medical imaging problems. For radar applications, the use of time reversal has been demonstrated as the contract of the reversal has the reversal has the contract of the reversal has the

strated for the imaging of targets in cluttered environments [71], as well as for obscured targets [72] such as through-wall [73] or buried [74] targets. Microwave imaging is an important development due to its use of non-ionizing radiation. Consequently, time reversal has been investigated for its use in breast imaging for cancerous tumors [75–77].

Using it for an imaging application is the focus of this thesis due to its relatively easy implementation as well as its low computation cost. As will be discussed in the following section, the low computation cost of this technique is vital for the final system since it provides near-real-time imaging and it limits monetary costs.

## 3.3.2 Theory and Implementation

In this work, time reversal is implemented to the real time domain waveforms to construct an image of the testing environment. The process and theory of electromagnetic time reversal described in this section is based off the development in [78]. Assuming that the imaging environment is lossless and passive, commonly done for air environments, the scalar wave equation can be written as

$$\left(\nabla^2 - \frac{n^2(r)}{c^2} \frac{\partial^2}{\partial t^2}\right) \phi(r, t) = 0, \tag{3.2}$$

where c is the speed of light in a vacuum and n is the refractive index in the medium. In this scenario, the term  $\phi(r,t)$  represents a solution of the scalar wave equation. Since there is a double partial time derivative applied to this solution, that means that an equivalent solution to this wave equation is  $\phi(r,-t)$ . Considering that  $\phi(r,t)$  represents a diverging wave from the transmitting sources, then  $\phi(r,-t)$  is a wave doing the opposite, converging on the transmitting sources. The time reversal operator is indicated as T in this section.

The diverging and converging scenarios can be considered equal in equation form as  $\phi(r,t) = T\phi(r,-t)$  [69]. Since these two solutions equivalently satisfy the scalar wave equation, their simulation in reversed time is a valid physical representation of the measurement scenario.

In order to construct this image, the waveforms are back propagated through a 2D Finite Difference Time Domain (FDTD) simulation [79]. This simulation has been adapted from the work that was done in [80]. The simulation is based upon the solving of the governing equations of electromagnetics, Maxwell's equations:

$$\nabla \cdot \mathbf{E} = \frac{\rho}{\epsilon}$$

$$\nabla \cdot \mathbf{H} = 0$$

$$\nabla \times \mathbf{E} = -j\omega\mu\mathbf{H}$$

$$\nabla \times \mathbf{H} = \mathbf{J} + j\omega\epsilon\mathbf{E}$$
(3.3)

where **E** and **H** are the electric and magnetic fields, respectively, **J** is the electric current source,  $\rho$  is the electric charge density,  $\omega$  is the angular frequency, and  $\epsilon$  and  $\mu$  are the permittivity and permeability, respectively.

In order to numerically simulate this environment, these equations must be discretely solved in time. The time domain version of Equation 3.3 can be obtained by replacing the  $j\omega$  in the third and fourth equation with a time derivative. Maxwell's equations can be solved discretely in time by creating a mesh of Yee cells [81] where the time step is related to time taken for the speed of light to cross one cell. This time step, however is different from the time step derived from the IFFT performed in 3.2.1, which is based upon the 10 GHz bandwidth of the transformation. Consequently, an interpolation of the pulsed waveforms obtained is required to map the IFFT time steps to the FDTD time steps. The numerical model for this simulation uses a TMz mode, where  $H_z$ ,

 $E_x$ , and  $E_y$  are vanishing to zero due to the lack of a transverse magnetic field component [80]. Each cell is created to be a square for simplicity. The length of the side of each square is selected to exactly satisfy the Courant condition for stability  $c\Delta t \leq \frac{\Delta x}{\sqrt{2}}$  [82]. It is a common rule of thumb to select a mesh size of  $\Delta x = \Delta y = \lambda/10$  in order to sufficiently mesh the simulation domain, for the reconstructed images presented in the results chapter a mesh size of  $\lambda/40$  was selected to ensure a well-meshed simulation.

FDTD simulations are used to simulate electromagnetic waves in a domain that can essentially be considered an infinite open space. Since this is clearly computationally impossible, the domain must be bounded by effective boundary conditions. These boundary conditions are necessary to avoid reflections off of the edge of the computational domain, which introduces non-physical energy back into the simulation, skewing results. Although many different boundary conditions have been researched and utilized in electromagnetic simulations [83–86], the Mur absorbing boundary conditions (ABC) [83] was selected for this case. These conditions are designed to avoid reflections off of the boundary interface. Although Mur ABCs can provide inaccuracies when waves hit the boundary at an oblique angle or when the source is close to the boundary [78], these situations are avoidable in the current simulation environment. ABCs are the simplest to implement and standard in simulations so more robust boundary conditions [84–86] were deemed unnecessary. Standard Mur ABCs were imposed on each boundary of the simulation environment.

# 3.4 Energy Calculation and Reconstruction

There are two primary methods for reconstructing an image from the measured results. The first method involves the entropy of the system, using the maximum of the inverse of the normalized variance of the fields. This technique

is known as the inverse varimax norm [75, 87]. Since entropy is colloquially known as "randomness", the electric field is the most focused (least random) at the time instant when the entropy is at a local minimum. At this time instant, a plot of the electric field is concentrated at the scatterers present in the imaging environment. The second method is using the time integrated energy to localize the target [80].

Once the frequency domain information is properly transformed and interpolated into the time domain and the time reversal and FDTD simulation properly prepared, the last step left is to simulate and reconstruct the image. As described before, time reversal simulation back propagates waves from the receivers and they converge onto the transmitters in a antenna system. During the measurement phase, each antenna takes a turn as a transmitter and the other 15 antennas act as receivers, filling the 16 by 16 matrix of each antenna pair. The received signals for one transmitting case is placed at the location of each receiver and the waves are back propagated through the simulation environment for the duration of the time waveforms. As these waves propagate through the environment, the energy at each of the FDTD cells is calculated with each passing time step. The total integrated energy  $(\mathcal{E})$  for each cell is calculated as a running sum per time step:

$$\mathcal{E}(x,y) = \sum_{i=1}^{N} E_z^2(x,y,t_i) \Delta t$$
 (3.4)

where N is the total number of time steps,  $E_z(x, y, t_i)$  is the electric field in the z direction at the (x, y) location at time  $t_i$ , and  $\Delta t$  is the time step.

This simulation is done for each transmitting energy case, giving the total integrated energy at each cell from  $\mathcal{E}_1$  to  $\mathcal{E}_{16}$ . Each of these provides a sub-optimal image of the environment. In order to create a full reconstructed

image, the 16 energy matrices are averaged to create one reconstructed image of the total average time integrated energy of the FDTD simulation environment. Overall, the time it takes for this information to process and to create a reconstructed system is about 60-65 minutes. Examples of this reconstruction will be presented and discussed in the next chapter.

# 3.5 Reconstruction Example

In this section, an example of the signal processing procedure will be outlined from start to finish. The waveforms as they are being processed are included to help better visualize the steps taken to turn measured frequency domain data into a fully processed image. This section will outline the signal processing steps to image a brass cylinder using the full system. This image of the test setup can be seen in Fig. 3.1. This section will cover only the signal processing, the hardware aspect and image quality will be discussed in Section 4.3.1.

# **3.5.1** Frequency to Time Domain Example

Once the frequency domain information is sampled by the network analyzer, the first step is to prepare it for the time reversal simulation. The procedure to do this conversion follows Section 3.2.1 and uses the code that is included in Appendix E. The code takes an input of measured frequency domain data and creates time domain pulses, each waveform can be seen in Fig. 3.2. The time domain waveforms of the measured empty ( $E^{inc}$ ) field, the measured field with the brass cylinder ( $E^{tot}$ ), and the resulting subtracted field ( $E^{scat}$ ) can be seen in Figs. 3.3, 3.4, and 3.5, respectively. These waveforms represent the received signals at antennas 2 through 16 while antenna 1 is transmitting, which is why the first line is set to exactly zero. Note that these waveforms are spaced vertically for visualization purposes only and the y-axis is not scaled to any true



Figure 3.1 Test setup of a brass cylinder being imaged by the microwave tomography system.

### value.

There are two notable aspects of these waveforms that can be used as sanity checks for proper performance of the measurement as well as the frequency to time domain conversion. The first aspect is the extremely large response of antennas 2 and 16 in Figs. 3.3 and 3.4. This is largely due to the fact that antennas 2 and 16 are direct neighbors of antenna 1. The mutual coupling be-

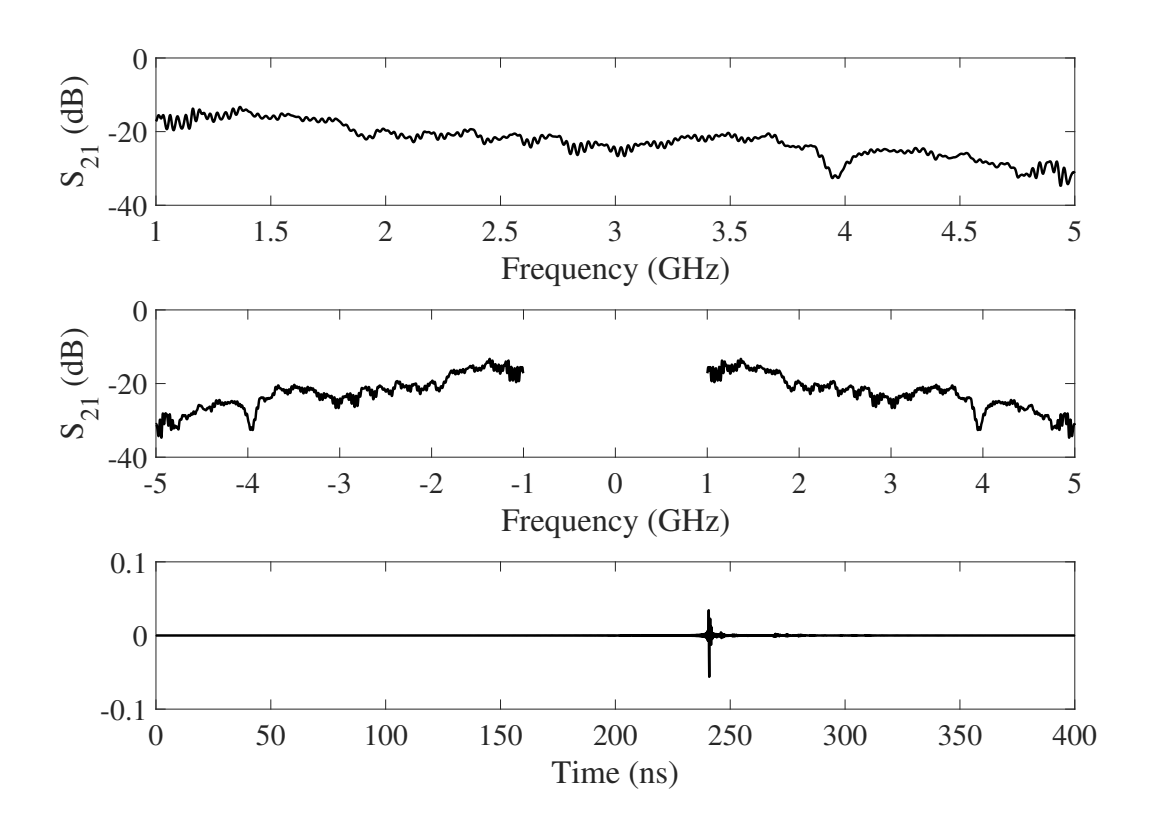


Figure 3.2 Measured frequency data in dB (top), zero padded and conjugate mirrored frequency data in dB (middle), and time domain pulse after the IFFT processing (bottom).

tween these antennas is much higher than the coupling between any of the other antennas. This is a good indication that the measurement was taken correctly since mutual coupling between neighboring antennas is always expected, especially while using planar non-directional antennas. The second sanity check is the moving wavefront of each antenna pair. The arrival time of the pulses starts with the neighboring antennas while antenna 9 receives the pulse last. This is expected due to the physical placement of the antennas. The varying flight time helps confirm that the inverse Fourier transform was performed correctly. After the subtraction, only the information from the added cylinder remains, as seen in Fig. 3.5. The mutual coupling is brought down significantly and only small

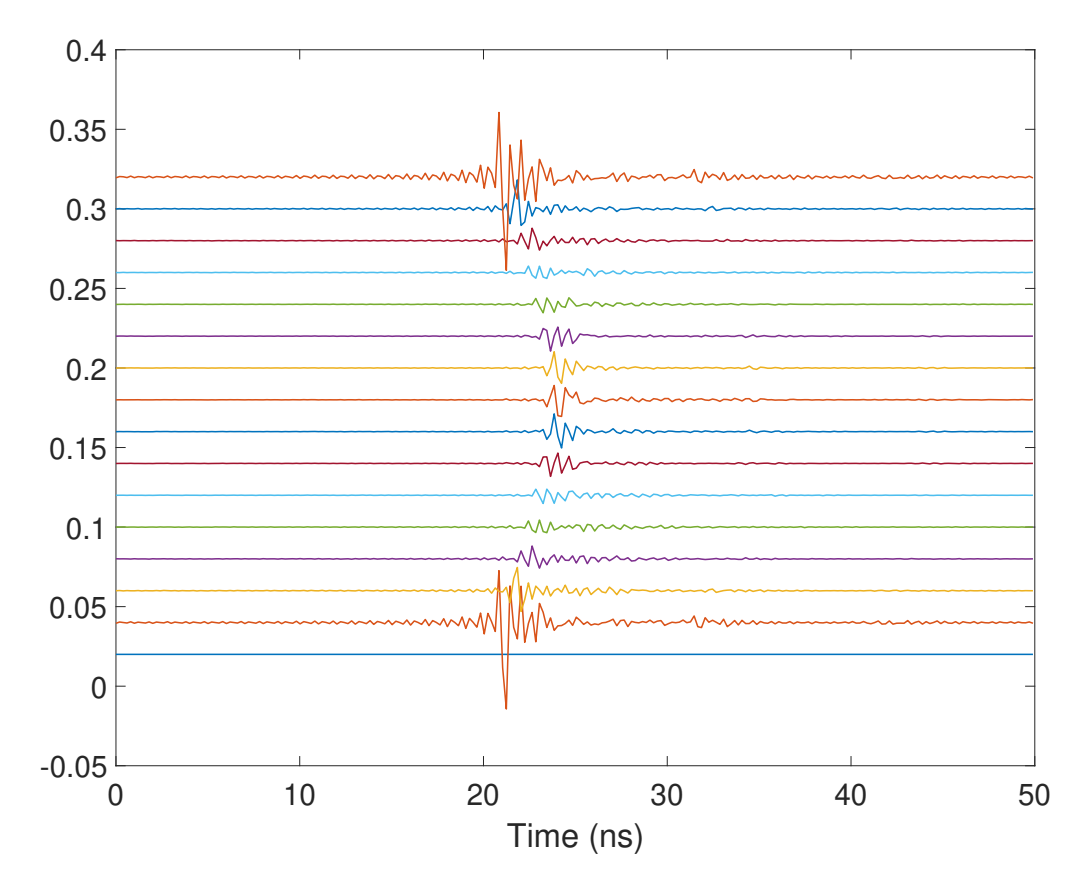


Figure 3.3 Time domain waveform of the measured empty environment.

ripples in the waveforms remain.

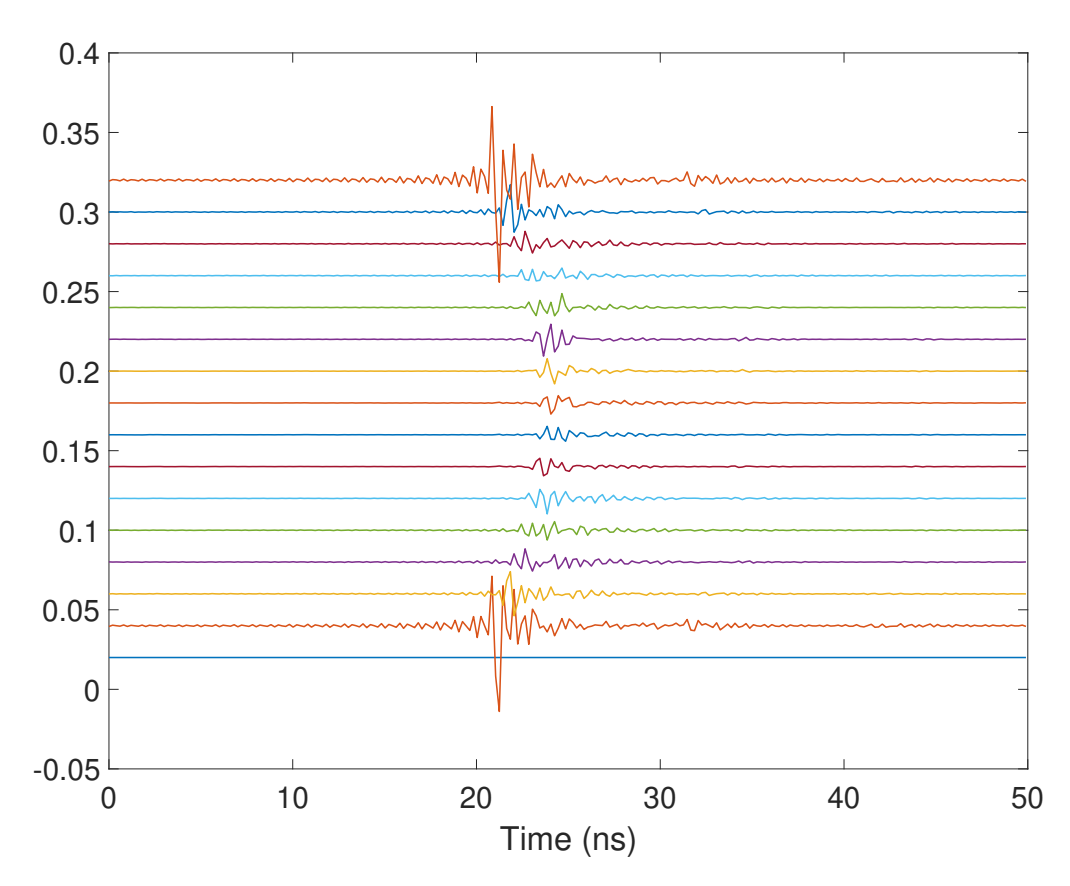


Figure 3.4 Time domain waveform of the measured cylinder environment.

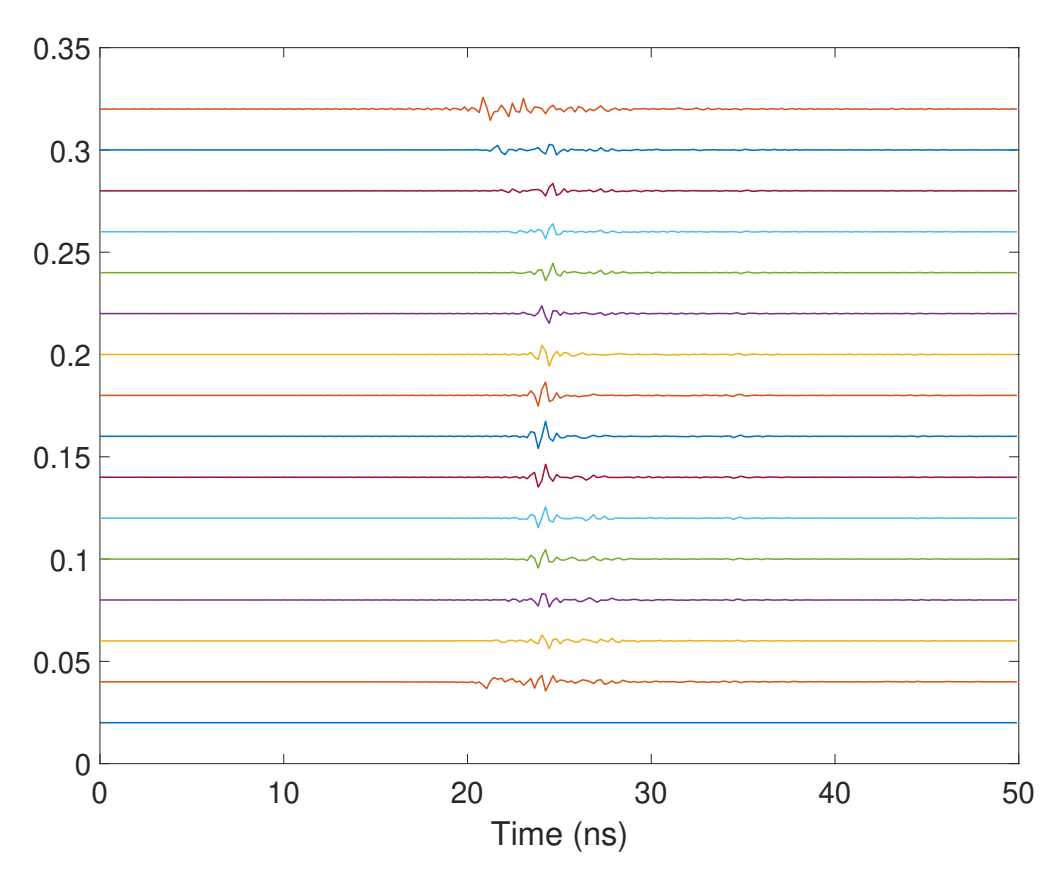


Figure 3.5 Time domain waveform of the measured empty environment subtracted from the measured cylinder environment.

## 3.5.2 Time Reversal and Image Reconstruction

Once the wavefroms are prepared, they are ready to process from time domain pulses to a reconstructed image. This is achieved by the code seen in Appendix F. This code steps through the process of time reversal from the measured results. During this process, the energy is being calculated at each cell in the simulation environment using Equation 3.4. This is done for every transmitting case, which produces a sub-optimal image each time. The sub-optimal images can be seen in Figs. 3.7, 3.8, 3.9, and 3.10. The position of each antenna number is labeled in Fig. 3.6. These locations will be used throughout this entire thesis. Notice that in these images there is no energy focused around the transmitting antenna. Also, depending on the position of the transmitting antenna there is a large amount of energy focused around the antennas that are in direct reflective paths of the cylinder, specifically in (c) and (d) of Fig. 3.10. Regardless, each of these images produces a clear location for the cylinder, so doing it 16 times provides a sufficient amount of information for the final image.

The final image can be seen in Fig. 3.11. This is done by averaging the 16 sub-optimal images created from each transmitting case, creating one image of the final environment. It is clear to locate the cylinder and the energy focused around particular antennas is greatly reduced by this averaging, which helps clean up the image and reduce unwanted noise. The impacts of this image and its comparison to an optical image will be discussed in Section 4.3.1.

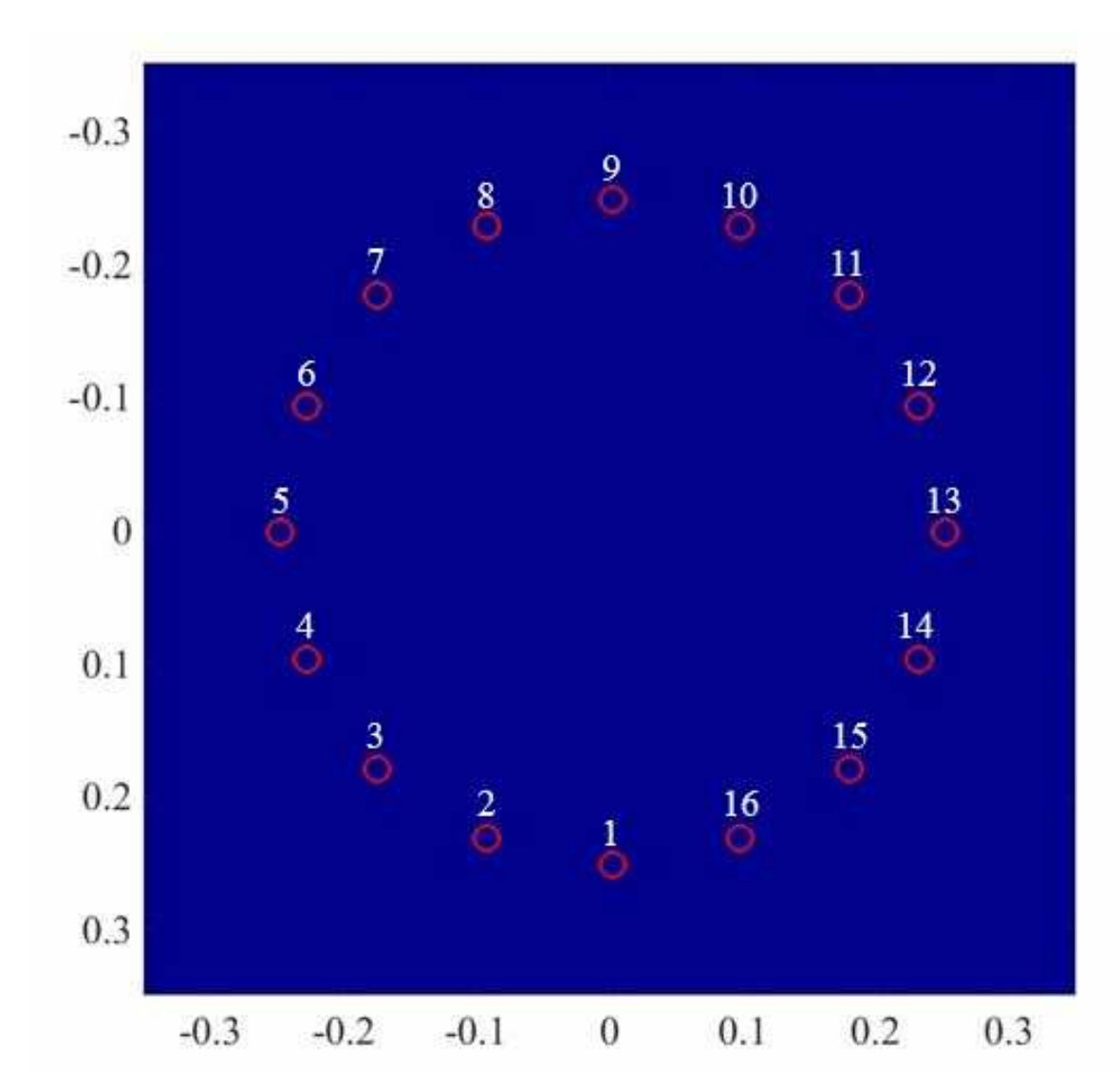


Figure 3.6 Location of each of the antennas in the ring.

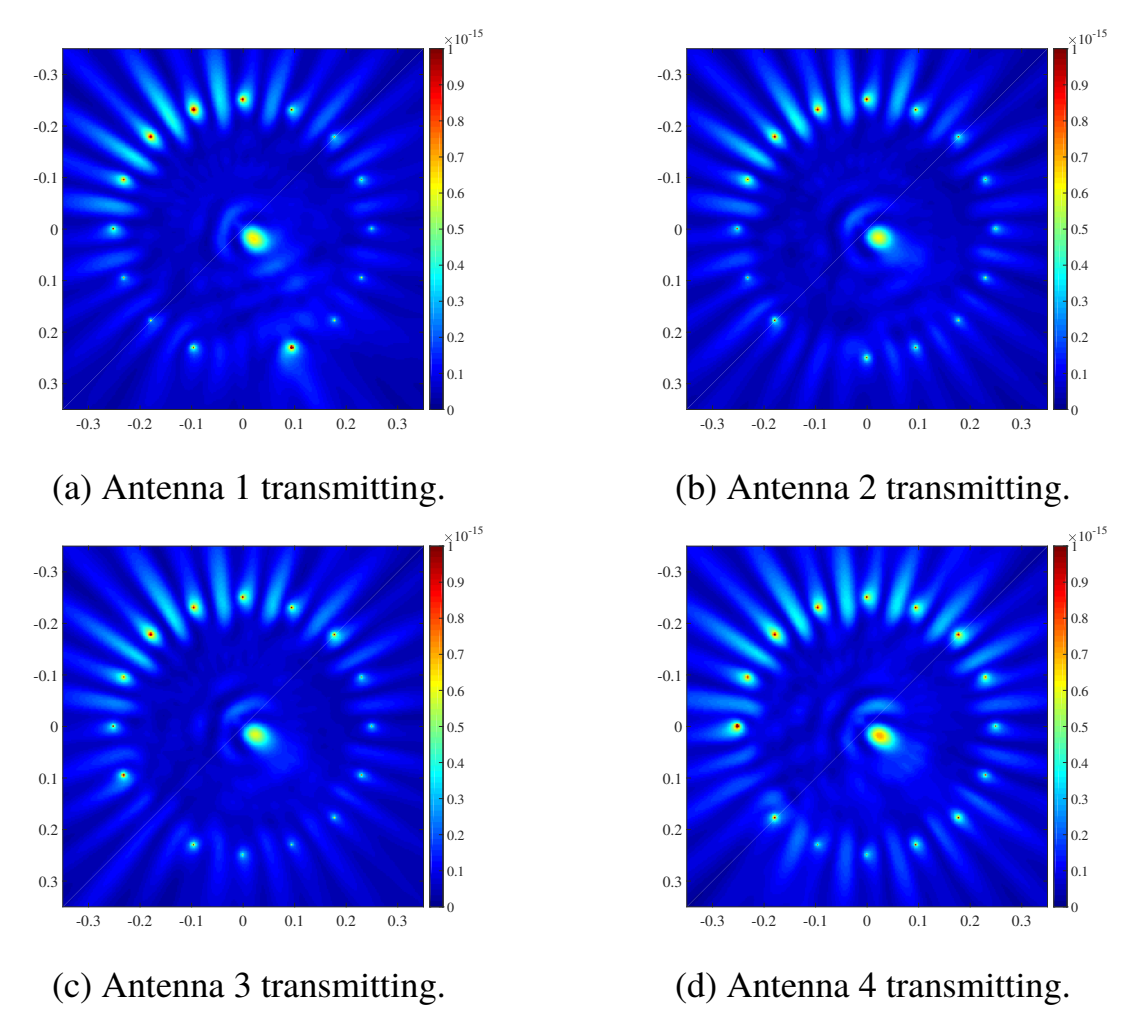


Figure 3.7 Sub-optimal reconstructed images of antennas 1 (a), 2 (b), 3 (c), and 4 (d) transmitting.

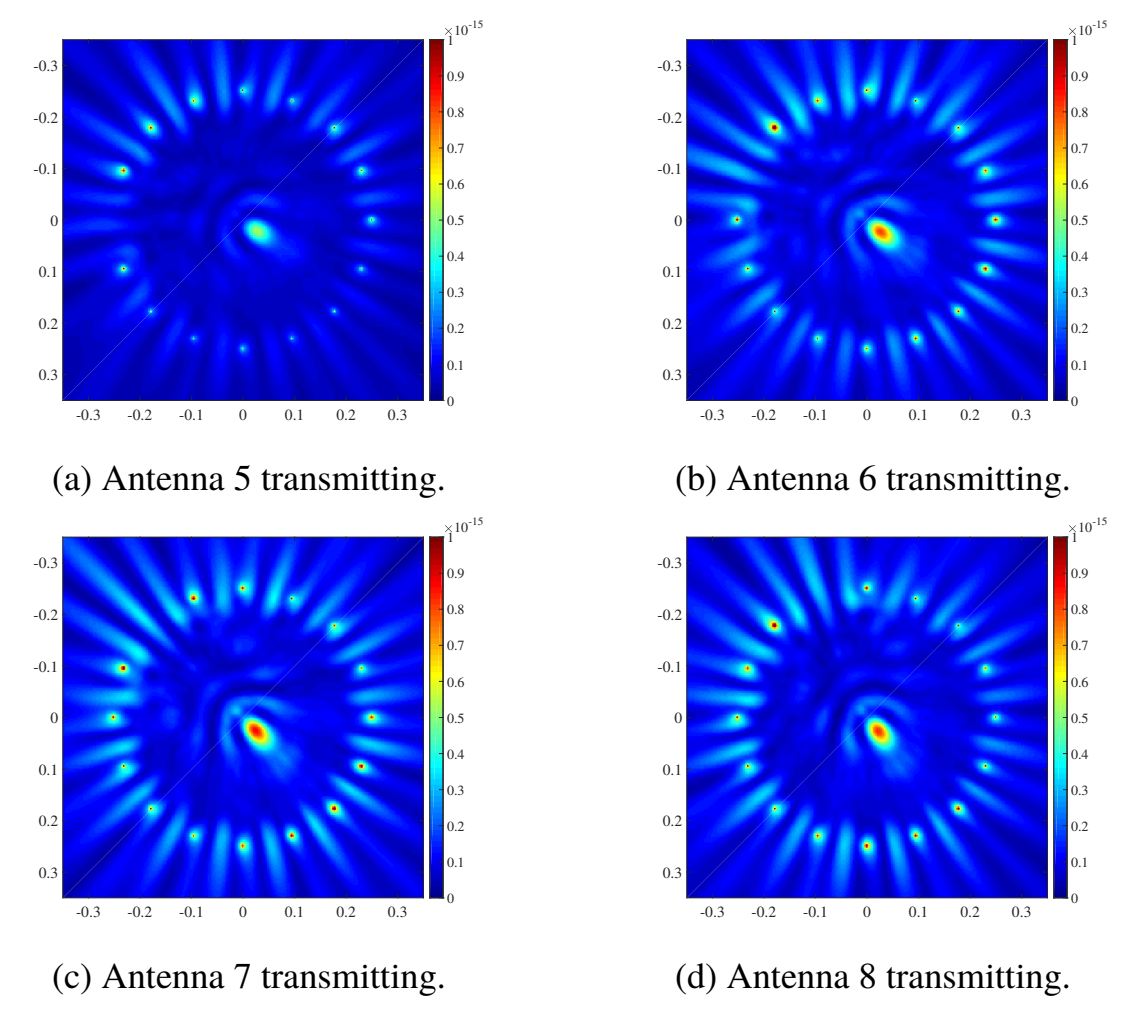


Figure 3.8 Sub-optimal reconstructed images of antennas 5 (a), 6 (b), 7 (c), and 8 (d) transmitting.

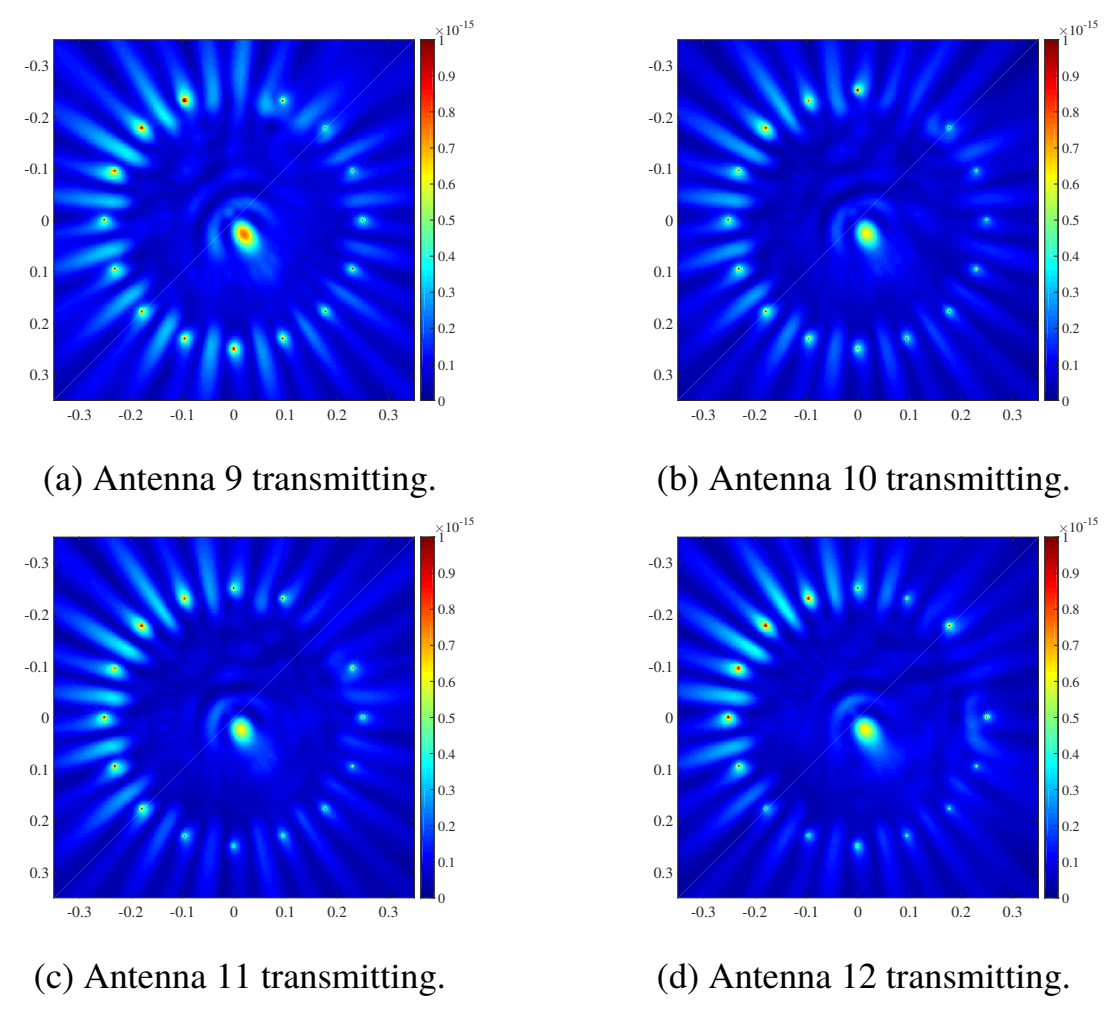


Figure 3.9 Sub-optimal reconstructed images of antennas 9 (a), 10 (b), 11 (c), and 12 (d) transmitting.

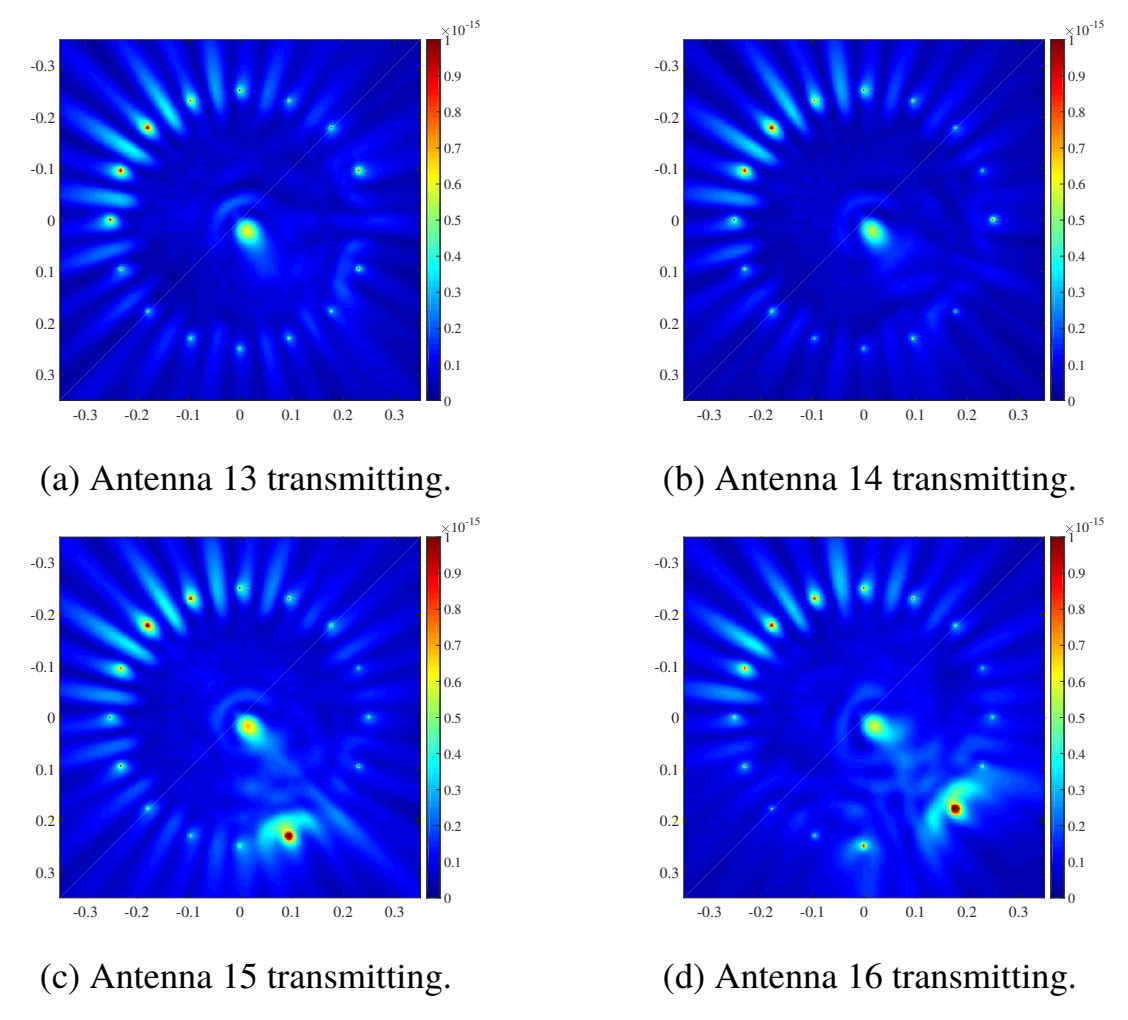


Figure 3.10 Sub-optimal reconstructed images of antennas 13 (a), 14 (b), 15 (c), and 16 (d) transmitting.

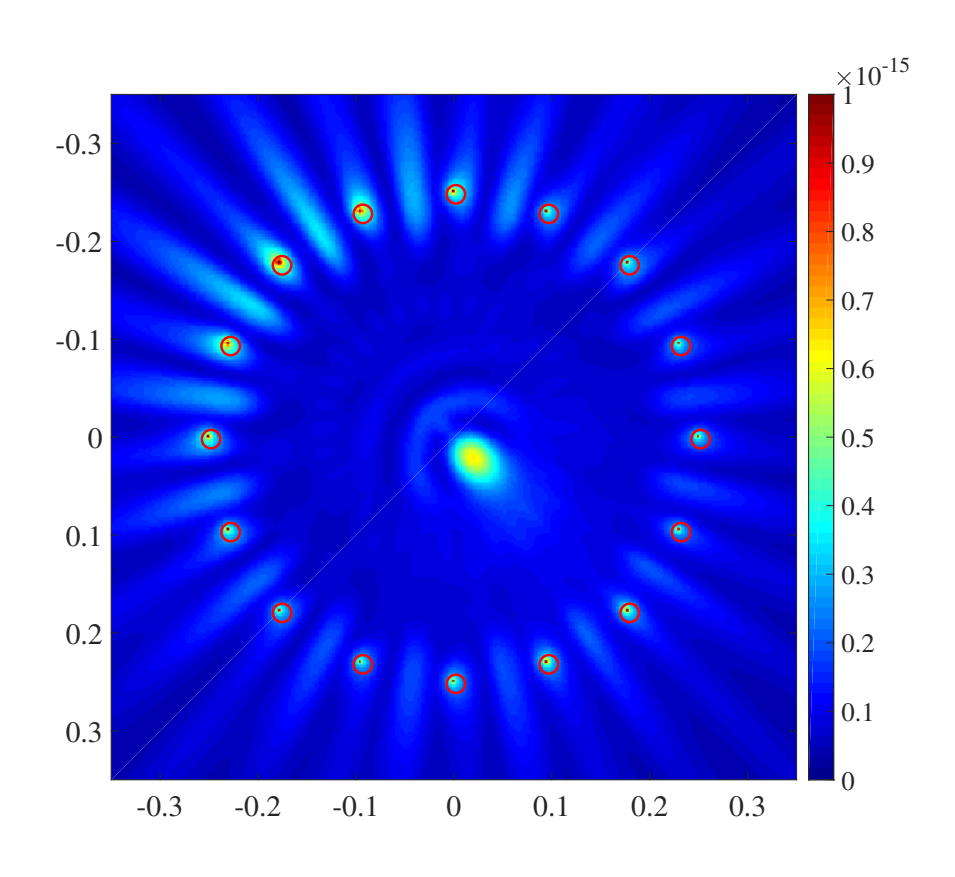


Figure 3.11 Total reconstructed image obtained from averaging the total energy in all 16 of the previous images, producing the brass cylinder shape.

### **CHAPTER 4**

#### MEASURED RESULTS

# 4.1 Introduction

In this chapter, the measured results of the microwave tomography system are presented. There are several variables that were tested using two separate methods. The first method was done using only two antennas and physically moving them to each pair of positions, collecting the frequency data per pair. This is described and the reconstructed images are included in Section 4.2. Simple cylindrical targets are imaged in this section. The other measurements that are presented are all using the system described in Chapter 2, using the switch matrix and the 16 antennas simultaneously. It should be noted in all of these images that there is a large amount of energy focused around the antennas. This is a expected result and will show up in all reconstructed images as there will always be energy around the antennas.

## 4.2 Pairwise Measurements

The pairwise measurement was performed by moving the pair of antennas connected to ports 1 and 2 of the network analyzer and recording  $S_{21}$  at each location, filling the 16 by 16 S-parameter matrix one-by-one. Clearly, this method is extremely time consuming and not a feasible way to execute in vivo measurements of tree trunks but it was an important step to verify the functionality of both the antennas and the imaging code before the switch matrix was fully constructed. A full 240 measurement matrix took between 6 and 7 hours to conduct using this method. The images shown were reconstructed using 500 points of the pulse instead of 250 (see Section 3.2.1 for more on

this), so the reconstruction time was about 90 minutes. Thus, the overall time from the start of measurement to reconstructed image was approximately 8 to 9 hours. This is not accounting for the calibration step of measuring an empty environment that represents the incident field that is subtracted from the scattered field (Equation 3.1) since this only is taken once and then used for all the scattered measurements. If this is factored in, another 6 to 7 hours should be added to the timing.

The first, and potentially easiest, case that was tested was using a brass cylinder. Since metal is very conductive it is often considered a close to real-world example of a perfect electrical conductor (PEC). This cylinder being very reflective is the best chance to successfully reconstruct an image. The optical image and its reconstructed microwave image can be seen in Fig. 4.1. This cylinder has a height of 6" and a dimeter of 1.25". In this image, the energy information had to be normalized per transmitting case, which explains the intensity of the color axis. The normalization was likely required due to the inconsistency of the pairwise measurements, the requirement to move antennas to each location by hand had a lot of variability and inconsistent energy transfer due to antenna positioning, orientation, etc.

The next case that was tested was a plastic cylinder. This is closer to a real world scenario since the signals pass through the object being tested instead of going around them like they do a PEC. The image and its reconstructed microwave image can be seen in Fig. 4.2. This cylinder has a height of 12" and a diameter of 5". This cylinder is black Acetron GP, which has an dielectric constant  $\epsilon_r = 3.8$  and a dissipation factor  $tan\delta = 0.005$ . Again, there is normalization of the energy for the same reasons as listed for the PEC case.

In both of the images, there is a good correlation between the optical image and the microwave reconstructed image. There is some shadowing in the reconstructed picture but for the first run, it pointed to a successfully operating system. Since these measurements took so long to take a single set, these were the only results attained. This merely confirmed the operation of the network analyzer and the antennas in the system and after this the switch matrix was added.

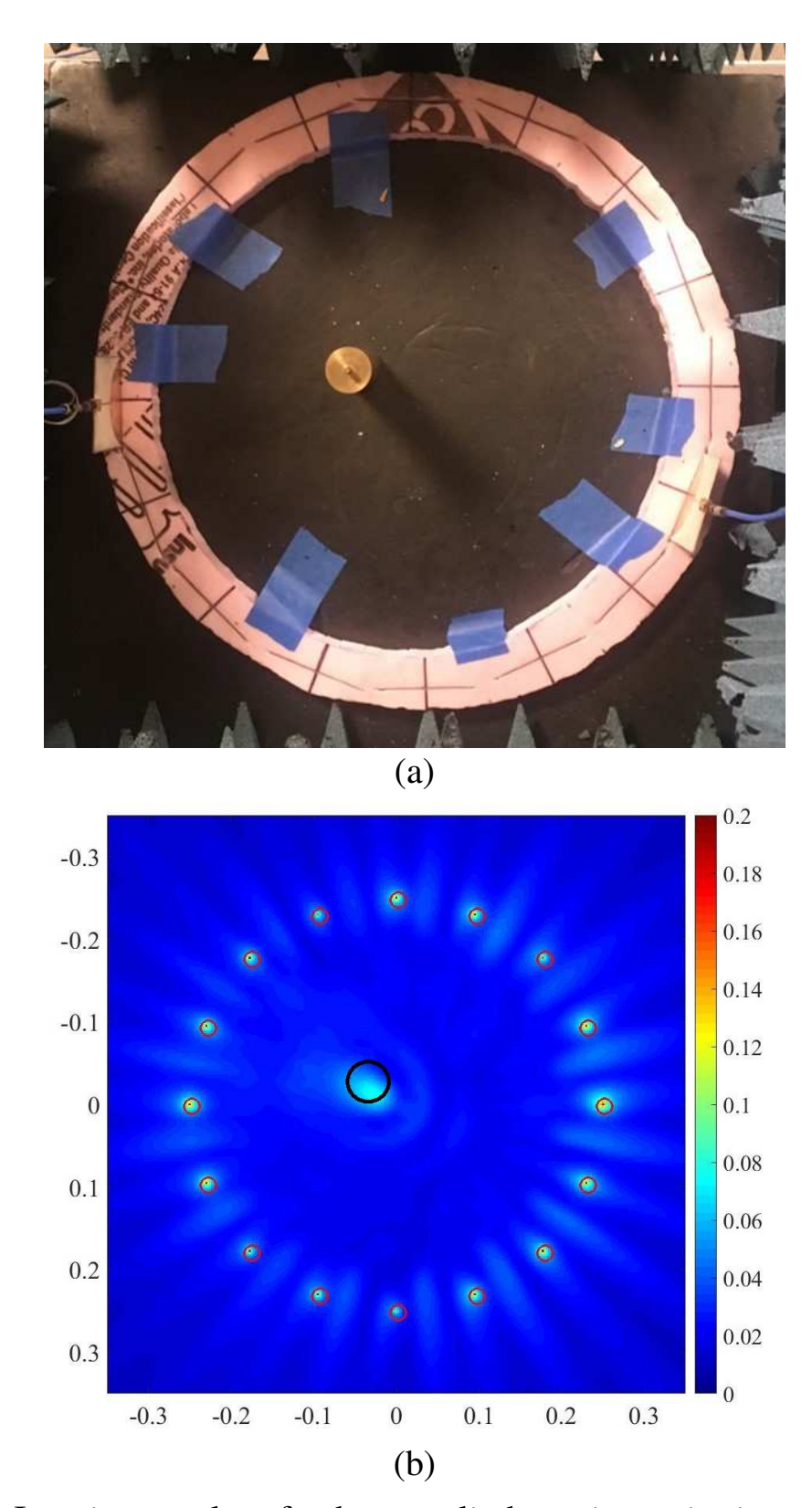


Figure 4.1 Imaging results of a brass cylinder using pairwise measurement technique. (a) Measurement setup. (b) Reconstruction.

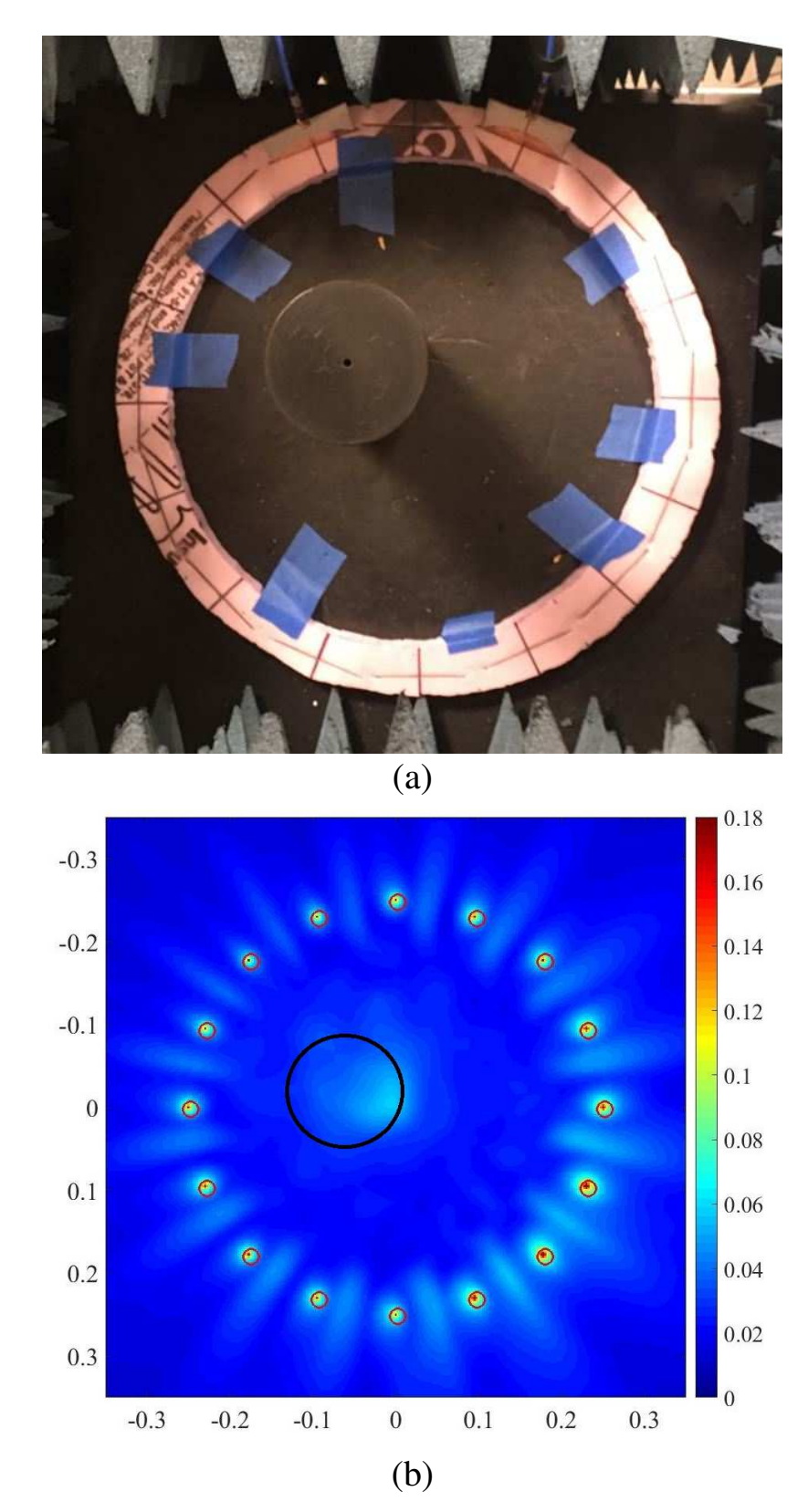


Figure 4.2 Imaging results of a plastic cylinder ( $\epsilon_r = 3.8$ ) using pairwise measurement technique. (a) Measurement setup. (b) Reconstruction.

# 4.3 System Measurements

In this section, the entire system was used for measurements of scatterers. This uses the automated switch matrix (Section 2.3) to take all 240 measurements without the need for human interaction between the sampling, which drastically cuts down on the measurement time. All 16 antennas are in the system simultaneously, as in Fig. 2.2. This is more reflective of the physical system that will be used in the final product. The cut of the measurement time went from 6 to 7 hours for the pairwise measurements to about 18.5 minutes, a huge improvement that allows many measurements to be taken in the course of a day.

### **4.3.1** Simple Scatterers

In this section, only simple, homogeneous, scatterers are used, similar to those seen in Section 4.2. These measurements, again, were used to validate the operation of the system and the reconstruction code. For these experiments, a 250 point pulse was used again, so this reconstruction time took about 45 minutes, for a total reconstruction time of about 60-65 minutes from beginning of measurement to reconstructed image. This is a nearly 90% decrease in total time as compared to the pairwise measurements, showing the value of the switch matrix for this system. For any feasible commercial imaging system it is absolutely essential.

The same brass (pseudo-PEC) and dielectric plastic cylinders were measured as a starting case. The optical images and reconstructed microwave images of the brass and plastic cylinders can be seen in Figs. 4.3 and 4.4, respectively. The color axis for this image does not use the averaging that was used in the pairwise measurements, which is a more accurate simulation representation of

the measurement scenario.

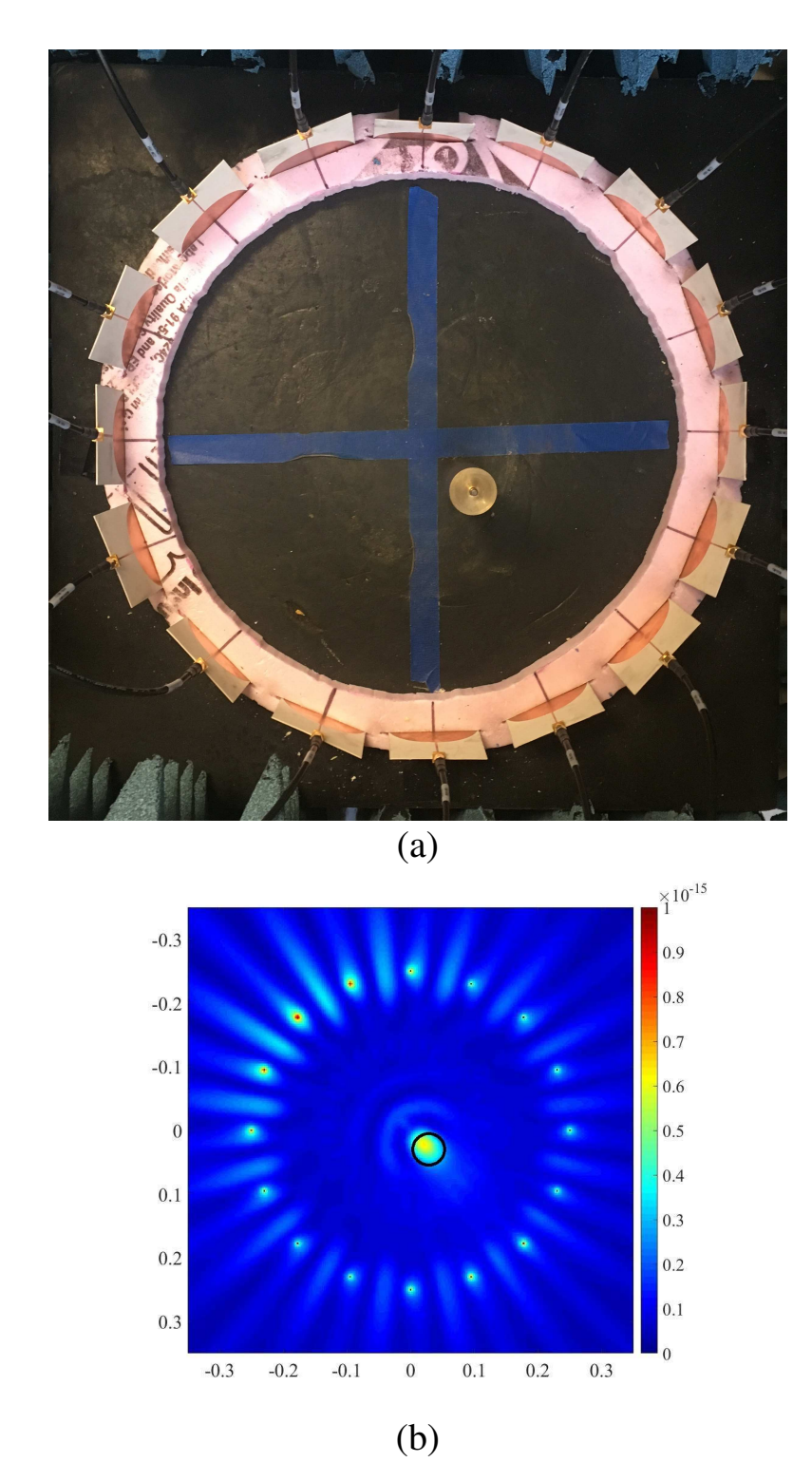


Figure 4.3 Imaging results of a brass cylinder using the entire measurement system. (a) Measurement setup. (b) Reconstruction.

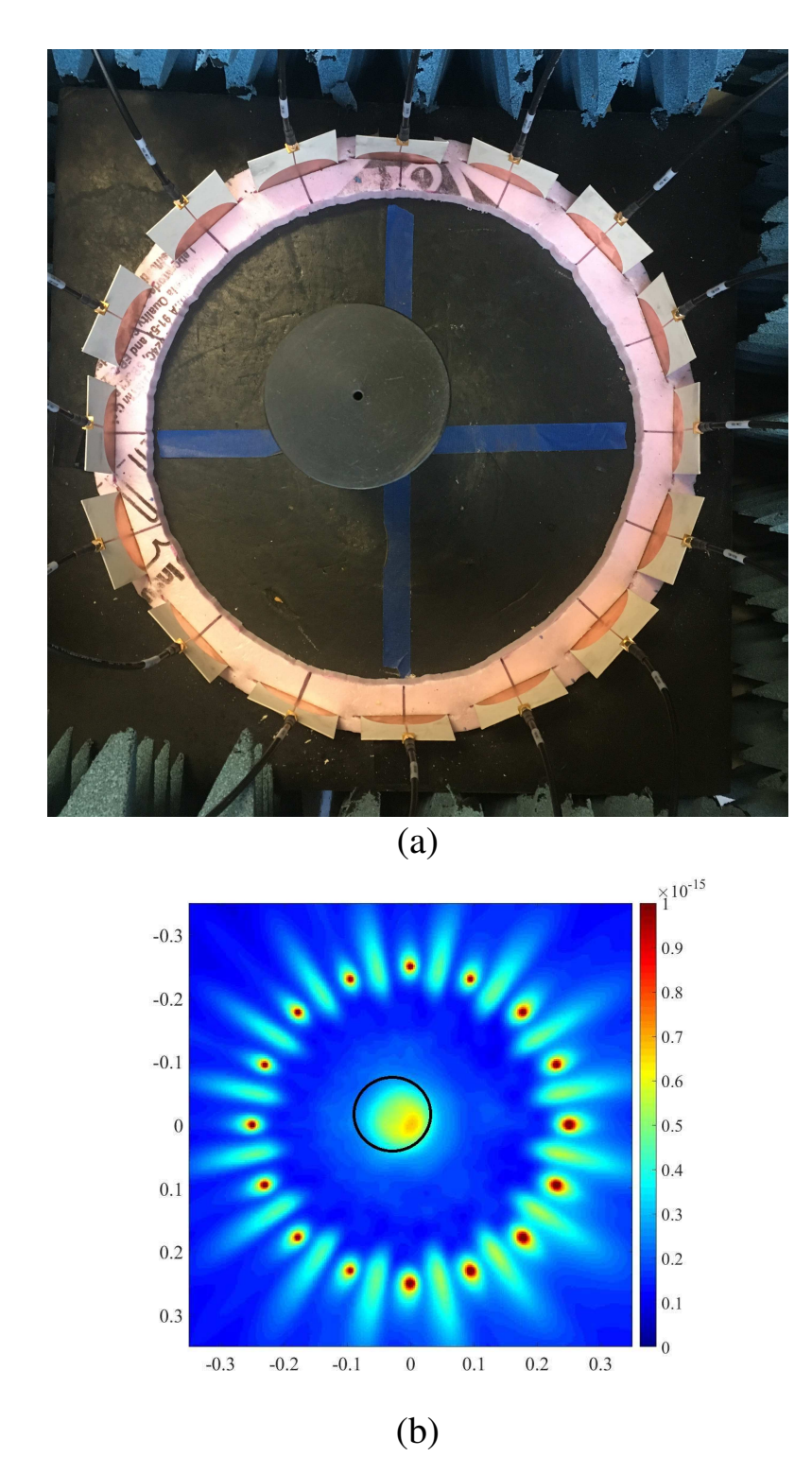


Figure 4.4 Imaging results of a plastic cylinder ( $\epsilon_r = 3.8$ ) using the entire measurement system. (a) Measurement setup. (b) Reconstruction.

After the functionality of the system was confirmed by measuring the cylinders, more complex structures were tested to push the abilities of the system. Fig. 4.5 shows the optical image and reconstructed microwave image of a plastic square prism. This prism is made out of Delrin, an electrically similar material to the cylinder measured above ( $\epsilon_r = 3.7$ ). The square base of the object is 4" by 4". The sharper corners can cause a more difficult imaging problem but the shape seems to appear in the microwave image.

Fig. 4.6 is an optical image and reconstructed microwave image of a wooden block. This block is a painted 4x4 from any typical hardware store (3.5" by 3.5"). The dielectric constant of this type of wood varies since it is generally made from a combination of multiple wood species, but it typically varies from 1.25-5. This ability of this system to image a wood structure is an important step towards the final system goal which is to image tree trunks.

Again, both of these more complex used the same physical parameters as above so the total imaging time was approximately 60-65 minutes. This illustrates an important aspect of the system. Since time reversal is not an inverse problem, the time from measurement to final image is always the same. Whereas an inverse problem would have trouble with a more complex structure compared to a cylinder and a more inconsistent material than the solid plastic or brass samples, these images take the exact same amount of time and computing power as the very simple sample targets. For a portable, low-cost imaging system this characteristic is extremely important.

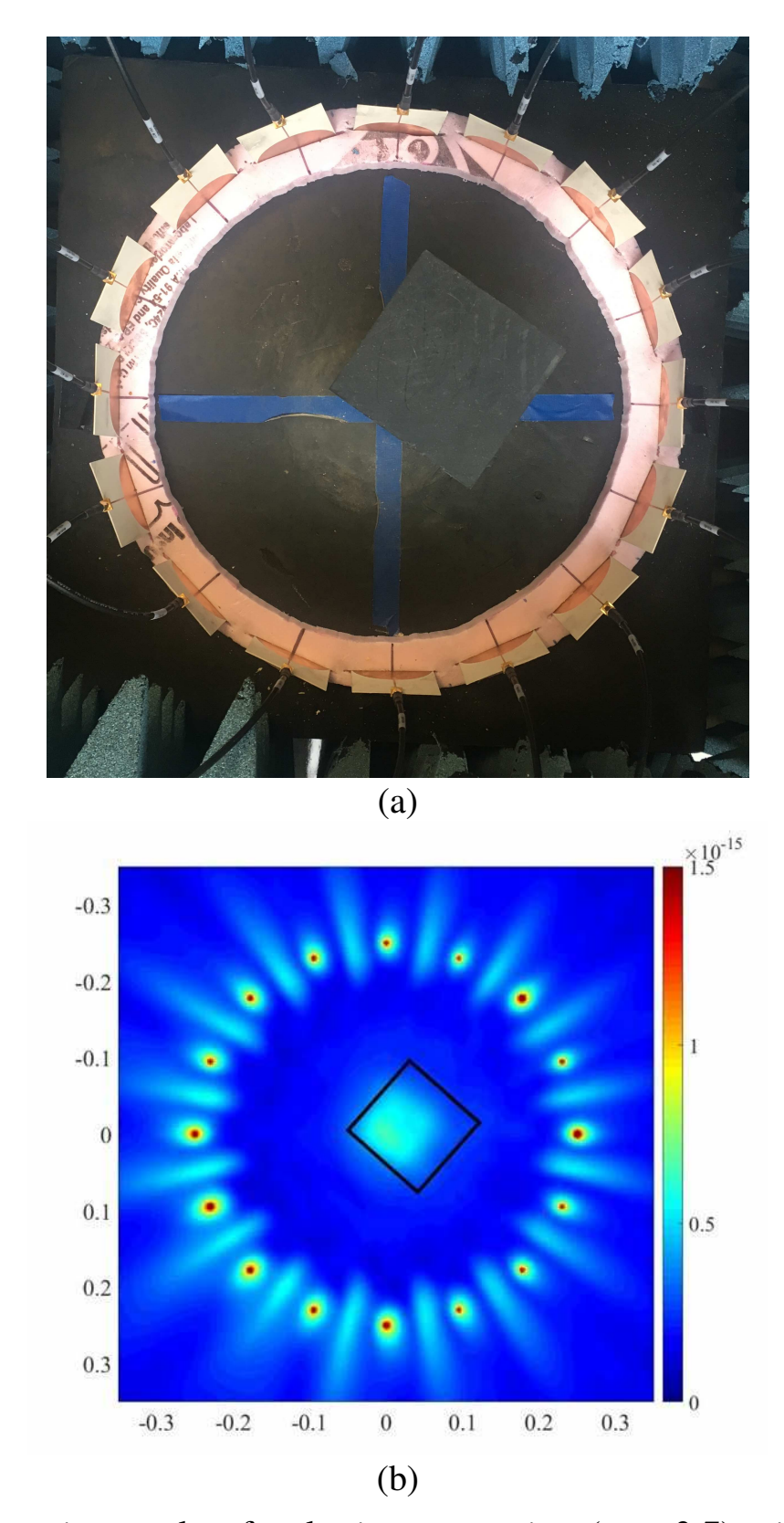


Figure 4.5 Imaging results of a plastic square prism ( $\epsilon_r = 3.7$ ) using the entire measurement system. (a) Measurement setup. (b) Reconstruction.

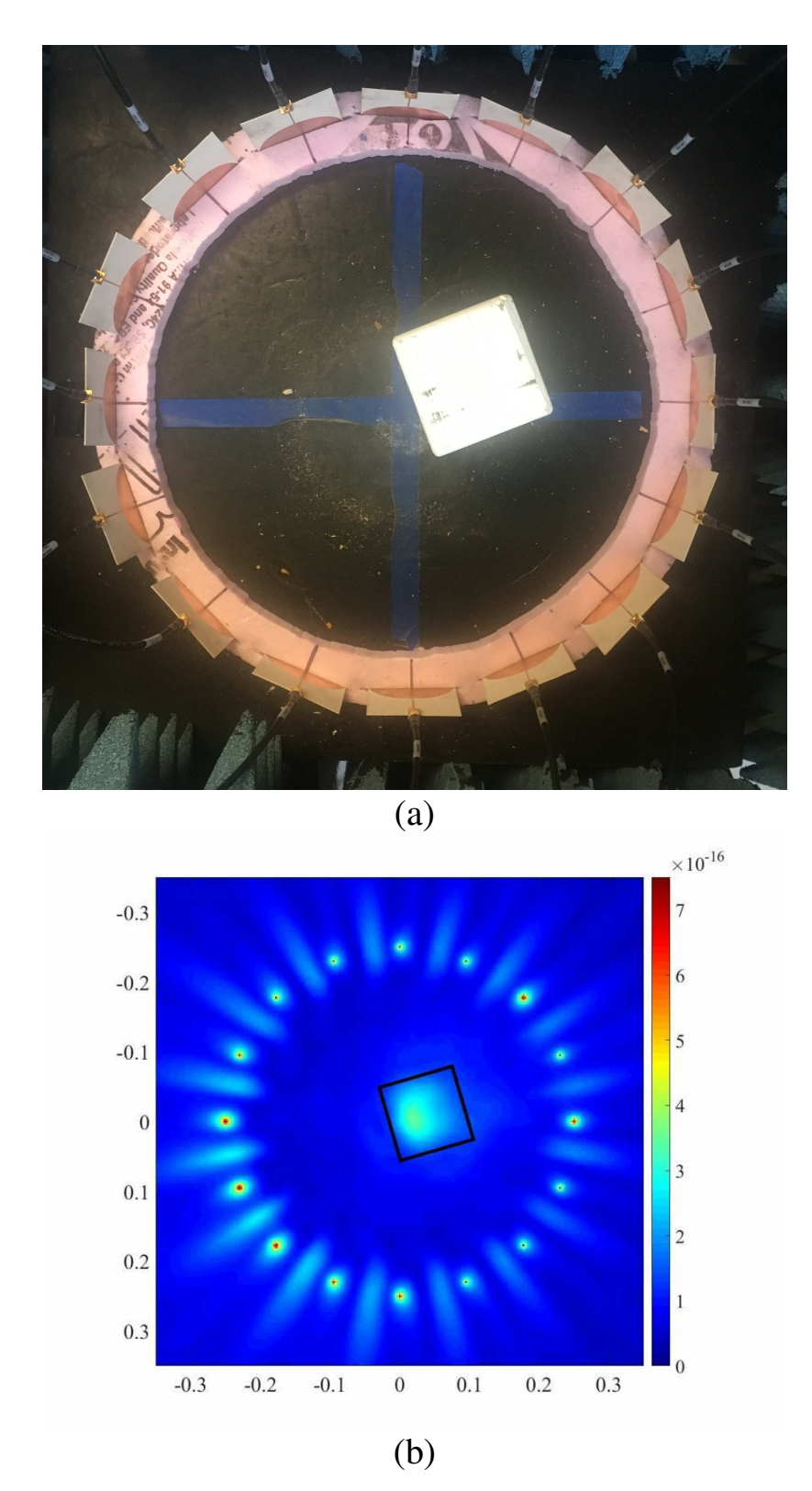


Figure 4.6 Imaging results of a wood block using the entire measurement system. (a) Measurement setup. (b) Reconstruction.

# 4.3.2 Tree Images

This section presents images of tree trunk samples with various types of simulated abnormalities on their inside. The two types of damage that are simulated are drilled holes, which are simulating unhealthy trees that are at risk of falling down in a wind or ice storm due to decay in their trunks, and metal inclusions, which are a threat to the lumber industry because they can damage saw blades and halt production when these blades break. Two species of trees were tested in this section, a basswood tree, which is less dense dicot tree and a sugar maple, which is a dense dicot tree species.

In this section, a different subtract step was taken in the signal processing. Whereas in the simple target case an empty environment was used as an incident field calibration step, other sections of the tree itself were considered the "incident field". Although this is a more complex measurement setup, it is not unrealistic for a real world system. Since decay in trees rarely spans the entire trunk, measurements could be taken at several heights of the trunk and each pair could be subtracted from the other. The subtraction used and optical images of both samples are presented with each presented result. Due to the addition of a second measurement, the time to create these images rises to approximately 80-85 minutes from start of measurement to reconstructed image.

# 4.3.2.1 Air Gap Images

Fig. 4.7 shows the imaging result of a basswood sample with a 1" diameter hole subtracted from a solid sample. The hole appears in the microwave reconstructed image as a small dielectric inconsistency. Although this is not a completely conclusive result and the inconsistency is hard to distinguish from the noise, it is a step in the right direction. For comparison, two portions of solid basswood logs were subtracted from each other. This result can be seen

in Fig. 4.8. As is seen in this reconstructed image, two solid portions of logs produce only noise and no definite inconsistencies can be recognized. Note that all the optical images seen in these two figures were taken after the logs had been completely dried, which explains the cracks and splits seen in the logs. The measurement was taken when the logs were freshly green, so each of the sections were completely solid with no cracks or splits other than the drilled hole. Also, the solid log in Fig. 4.8 has a nail added to it, which was used for the metal inclusions test. Again, this picture was taken much later and the data used for the microwave imaging was a measurement of the solid log with no nail included.

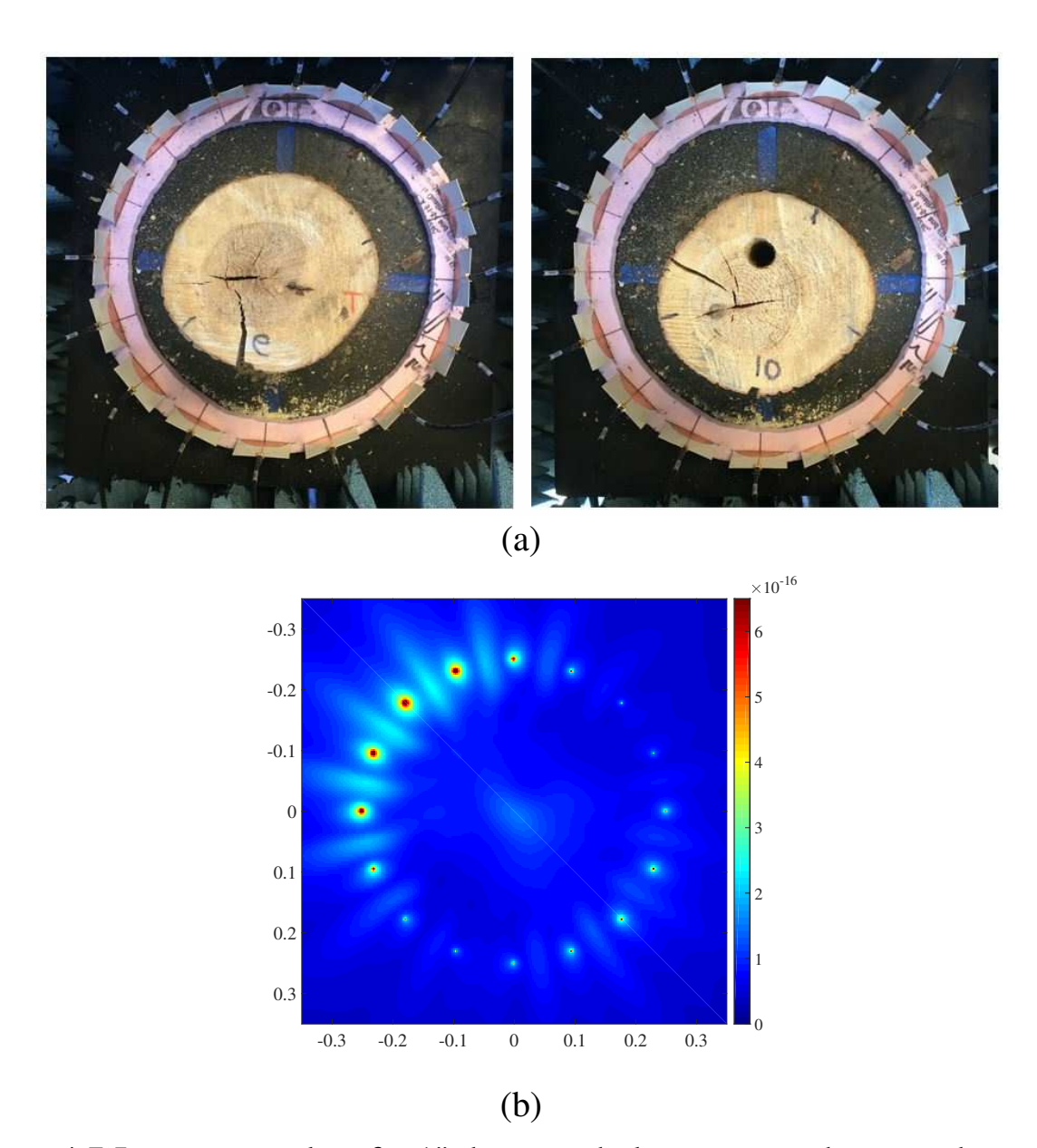


Figure 4.7 Imaging results of a 1" diameter hole in a green basswood sample. The solid portion of the trunk (left (a)) was subtracted from the portion with the hole (right (a)). (b) Reconstruction.

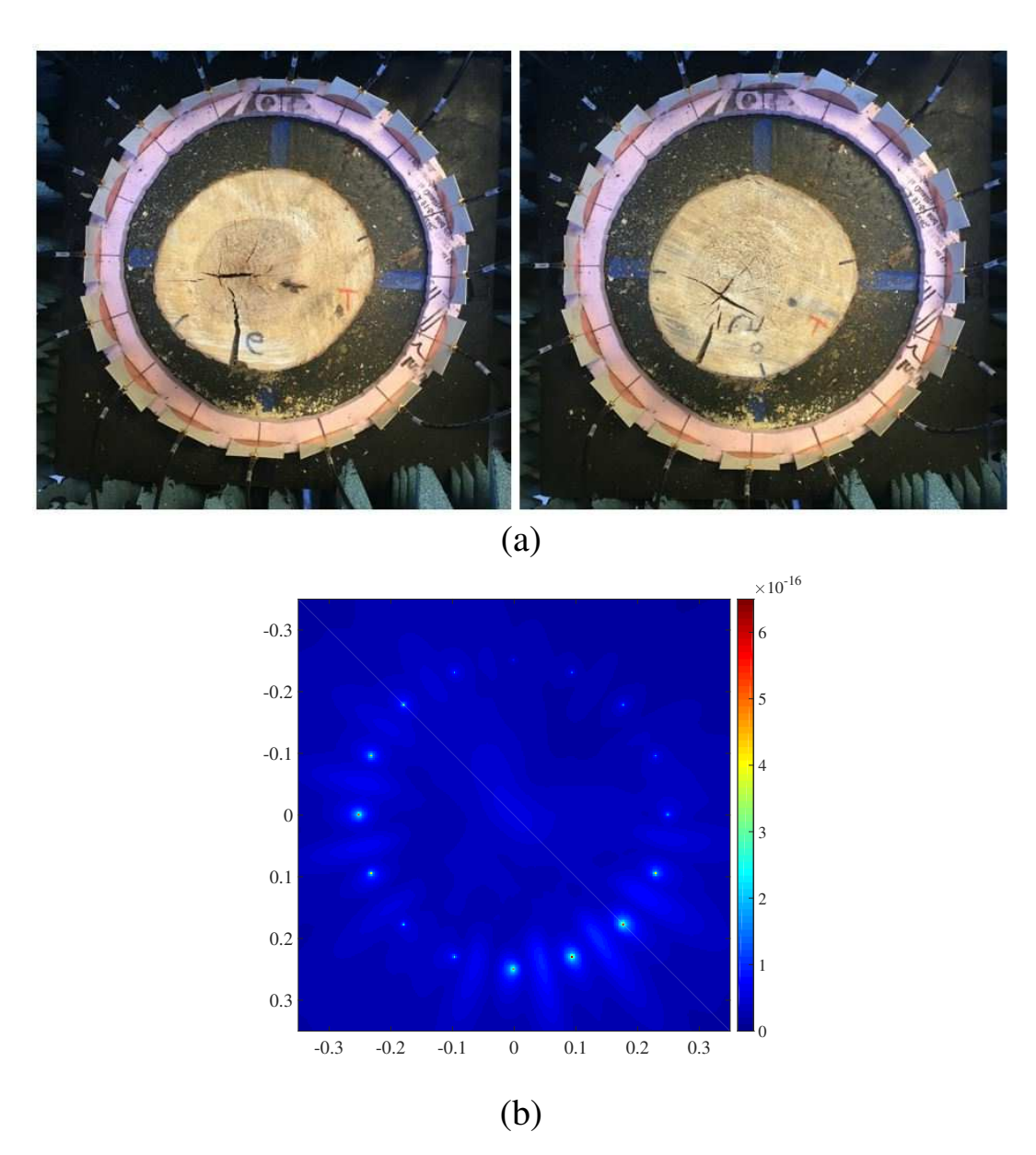


Figure 4.8 Imaging results of a solid, green basswood sample. Two solid portions of the trunk (a) were subtracted from each other and only noise remains in the reconstructed image (b).

Similar results were obtained for a sugar maple sample. The imaging results for a 2" diameter hole and a solid log (again the nails in the optical image were added after the microwave measurement was taken) can be seen in Figs. 4.9 and 4.10, respectively. Again, the results are not conclusive, but there is a definite contrast between the hole gap image and the solid log image. This points to a feasible idea for a future system.

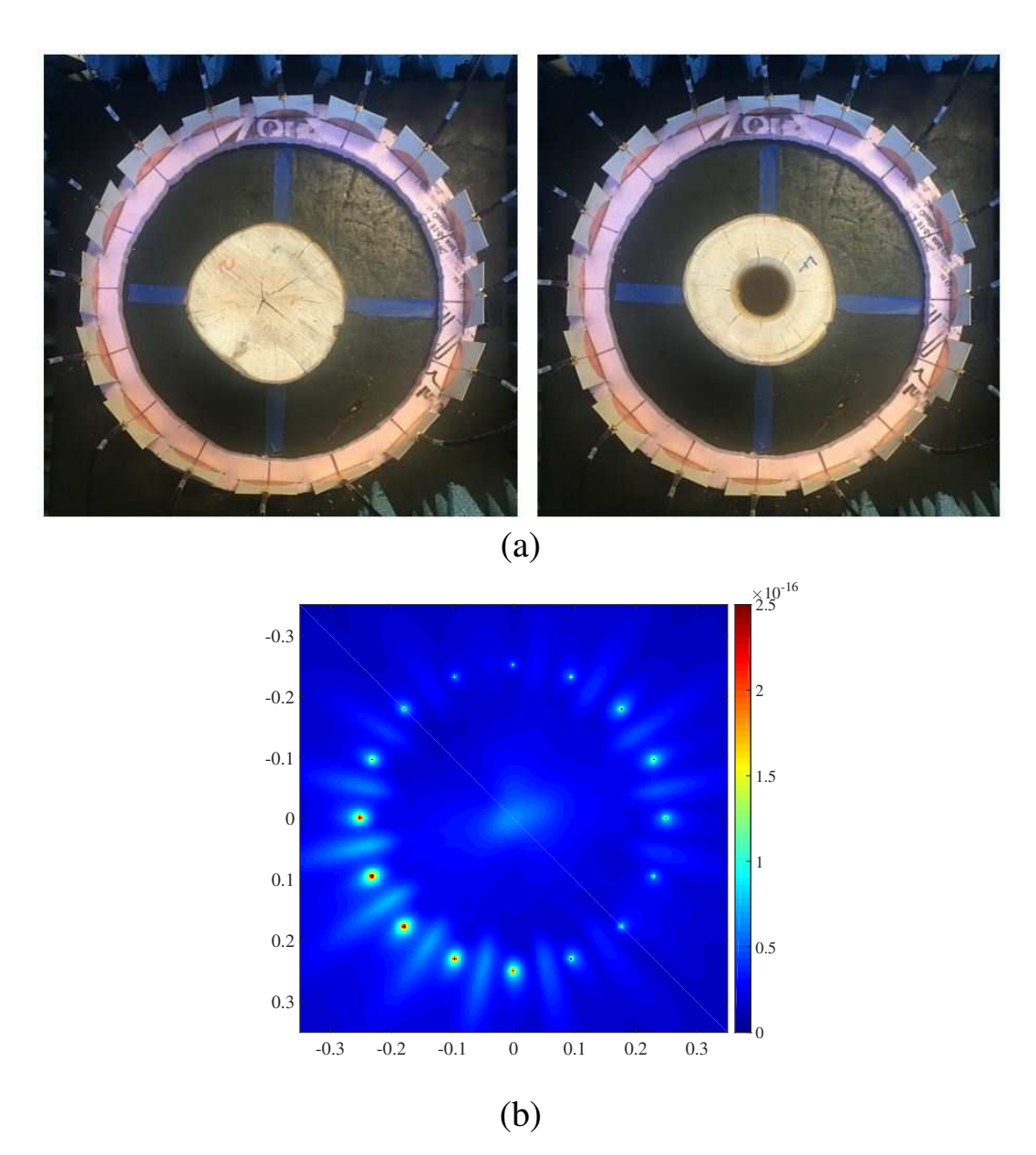


Figure 4.9 Imaging results of a 2" diameter hole in a green sugar maple sample. The solid portion of the trunk (left (a)) was subtracted from the portion with the hole (right (a)). (b) Reconstruction.

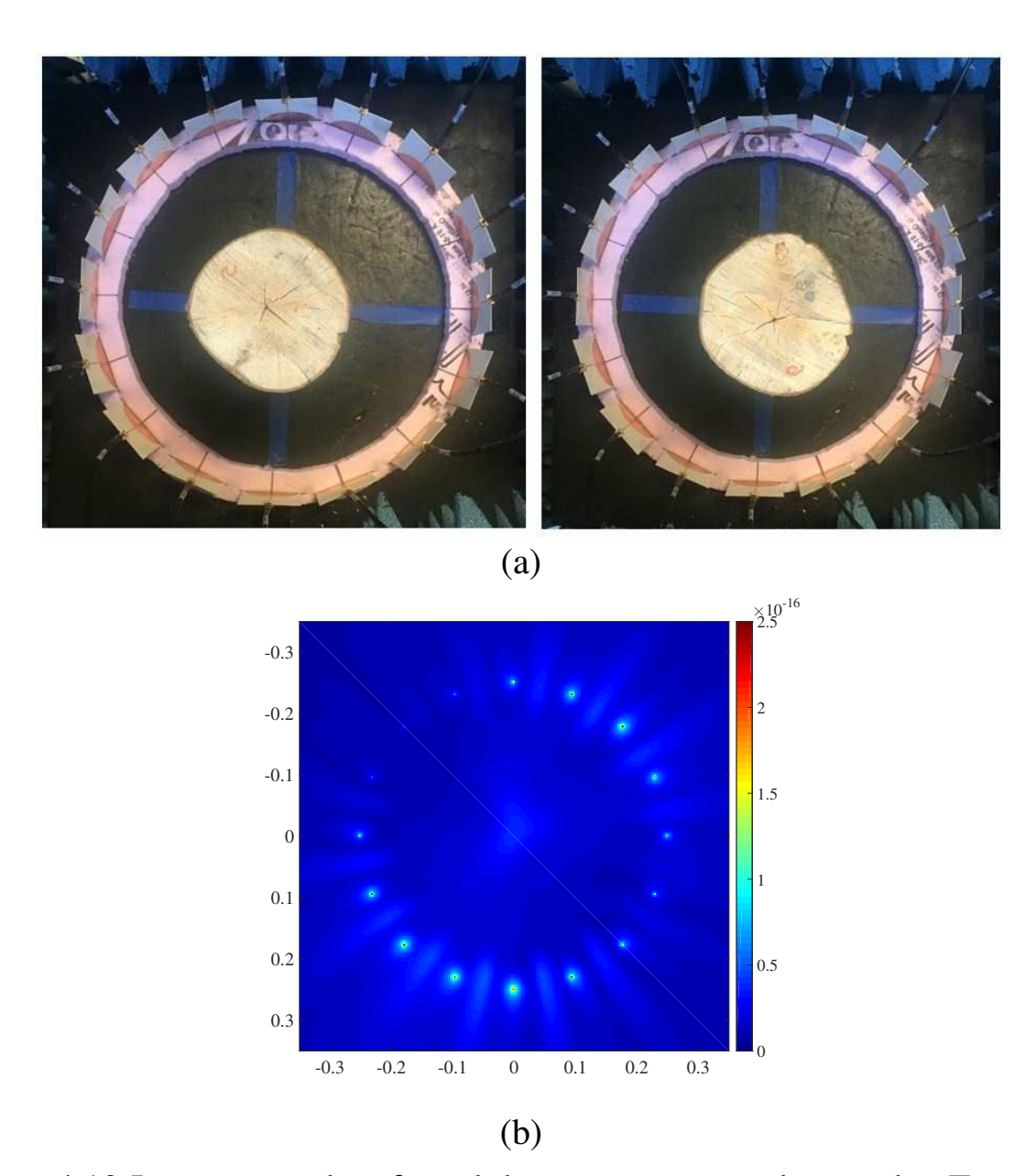


Figure 4.10 Imaging results of a solid, green sugar maple sample. Two solid portions of the trunk (a) were subtracted from each other and only noise remains in the reconstructed image (b).

These images were all obtained using measurements of freshly cut, green tree trunk samples. These samples were measured to contain 50-50% water by weight, clearly a much different dielectric consistency than pure wood. Measurements of air gaps were more successfully obtained after completely drying the samples and measuring only the wood samples. This demonstrates a functioning system and feasible results for using this as a tree imaging system. The following images will present images using completely dried wood.

Figs. 4.11 and 4.12 show the imaging results of holes in a basswood and a sugar maple sample, respectively. As is seen in these images, the results are much more conclusive and the holes are much more evident in the reconstructed image. It is suspected that the penetration of the waves into the sample are to blame for this drastic difference between the green and dry measurements. The addition of water to the trees introduces much more loss into the system and the waves are likely not reaching from one antenna to another in a direct path. This is an issue that will need to be further investigated. Fig. 4.13 presents two solid logs subtracted from each other, in which noise only remains, again demonstrating the feasibility of the measurement technique.

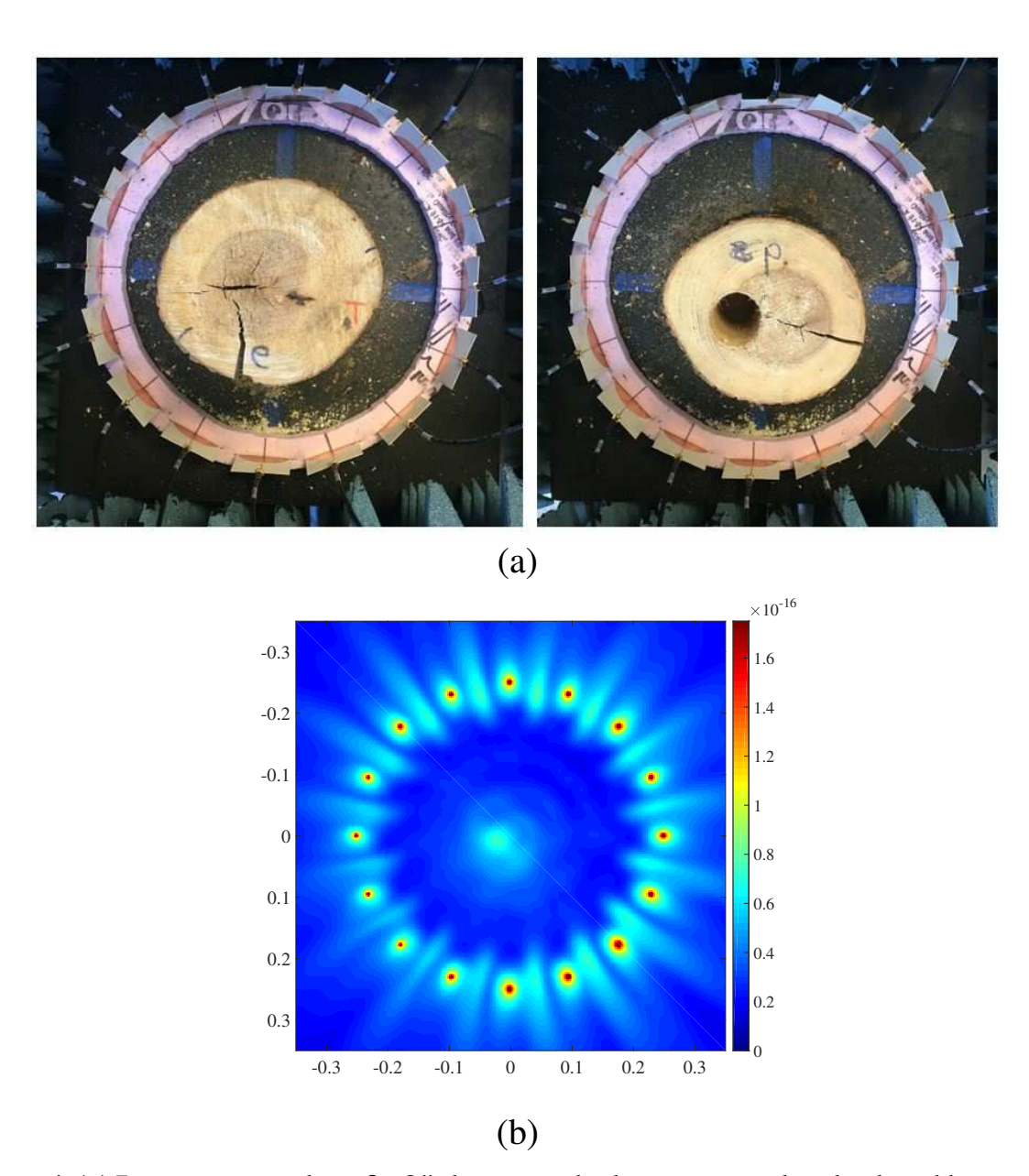


Figure 4.11 Imaging results of a 2" diameter hole in a completely dried basswood sample. The solid portion of the trunk (left (a)) was subtracted from the portion with the hole (right (a)). (b) Reconstruction.

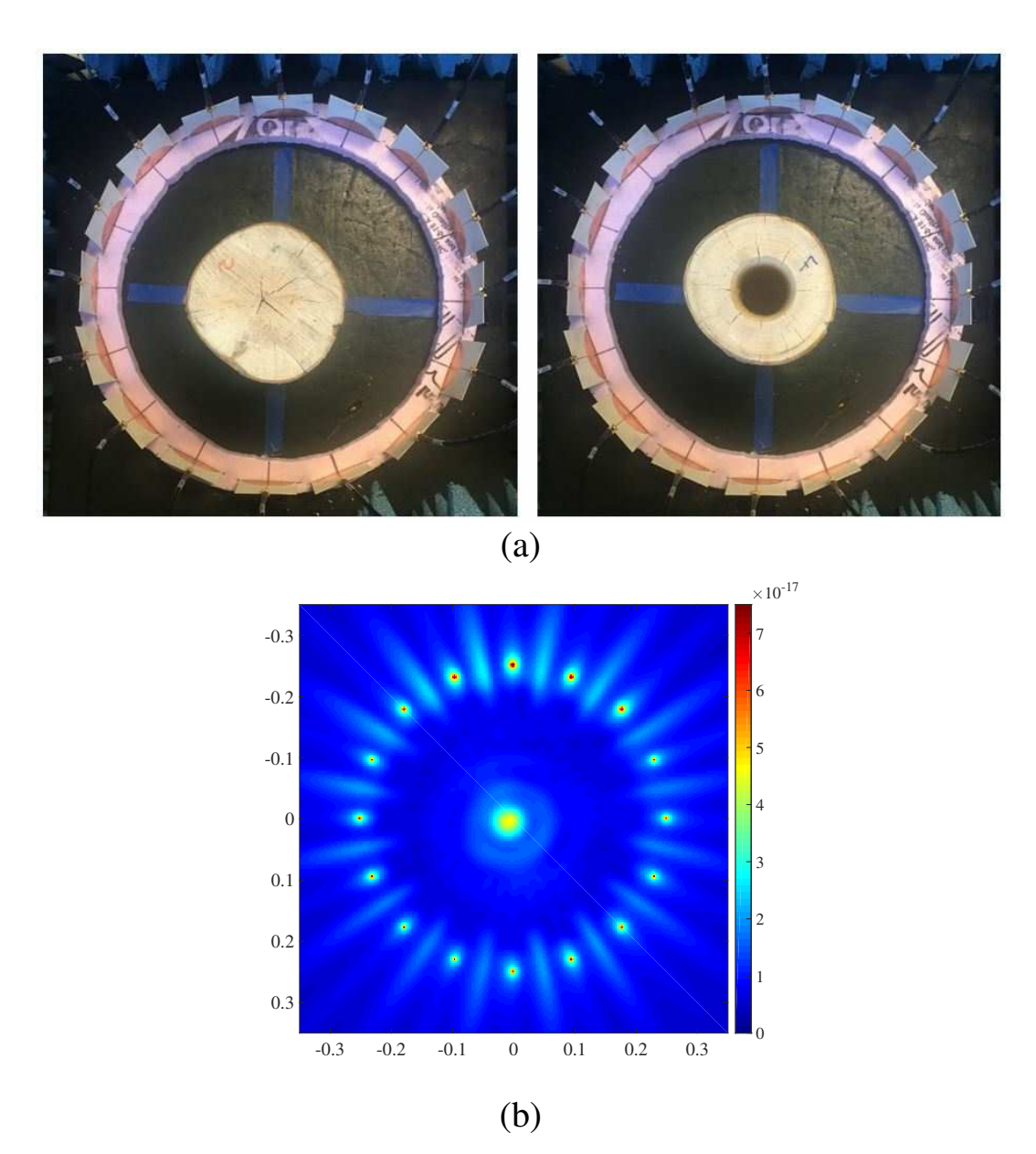


Figure 4.12 Imaging results of a 2" diameter hole in a completely dried sugar maple sample. The solid portion of the trunk (left (a)) was subtracted from the portion with the hole (right (a)). (b) Reconstruction.

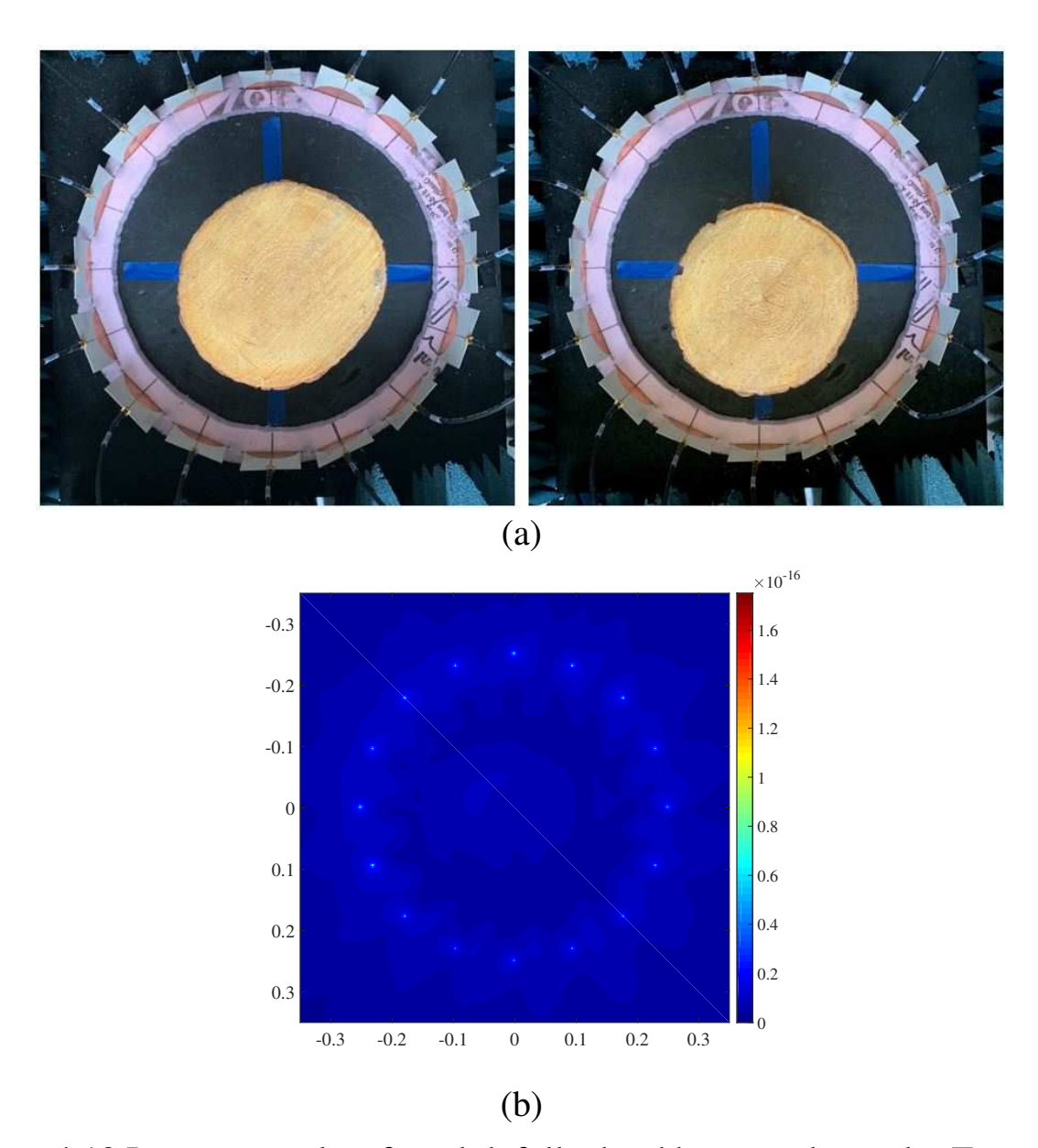


Figure 4.13 Imaging results of a solid, fully dried basswood sample. Two solid portions of the trunk (a) were subtracted from each other and only noise remains in the reconstructed image (b).

# **4.3.2.2** Metal Inclusion Images

This section will show images of logs that have metal inclusions embedded in their trunks. Figs. 4.14 and 4.15 show the results of a bolt added to a basswood and a maple trunk sample, respectively. The pictures seen in these figures have 1" holes drilled in them. Measurements of these logs (completely dried) were taken with the log and then again with a bolt added to these 1" holes. These two measurements were subtracted from each other and the images were obtained. Although this measurement situation is not necessarily feasible in a real world scenario, it is an important first step to confirming the use of this system to image metal inclusions.

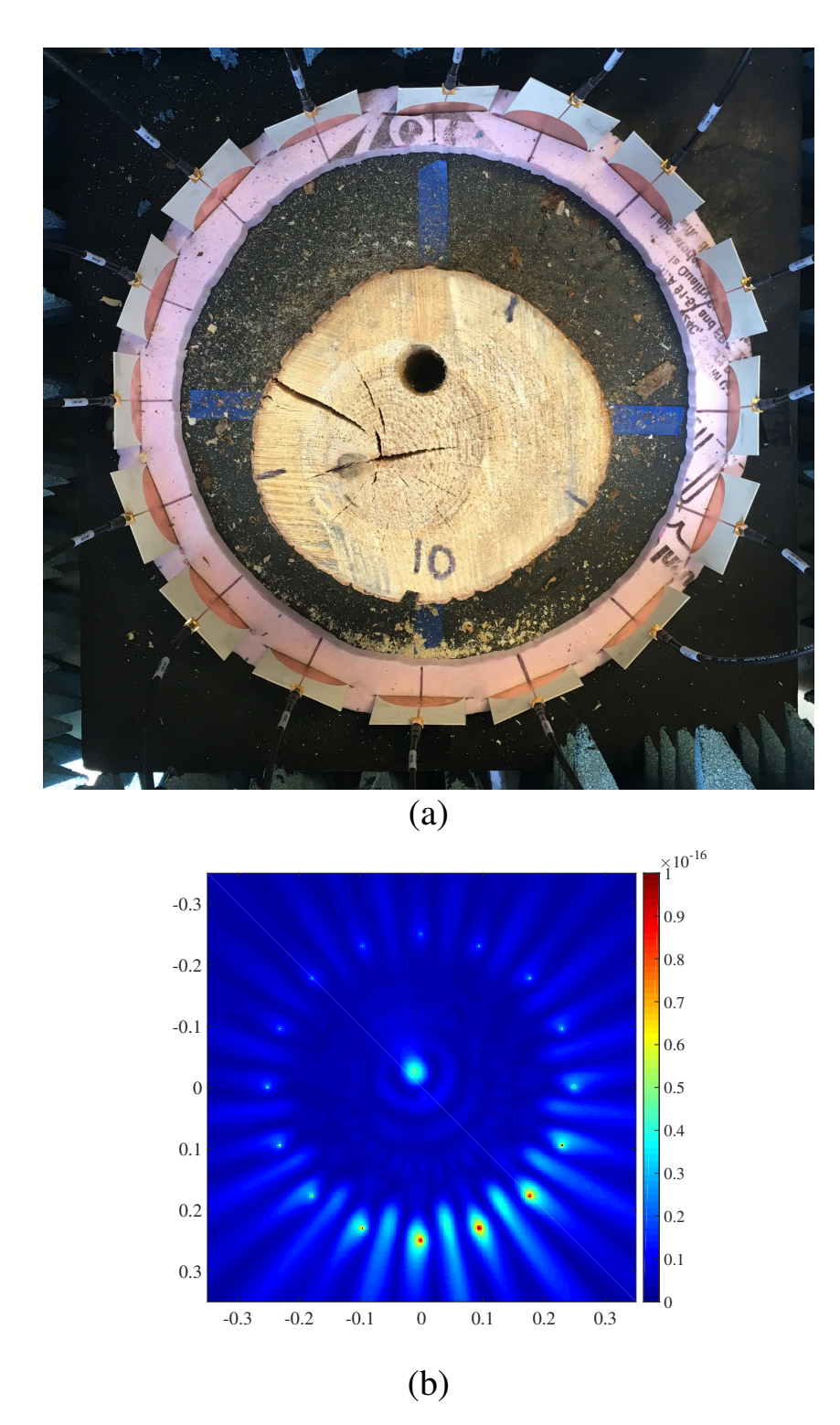


Figure 4.14 Imaging results of a bolt added to a 1" hole in a completely dried basswood sample (a). (b) Reconstruction.

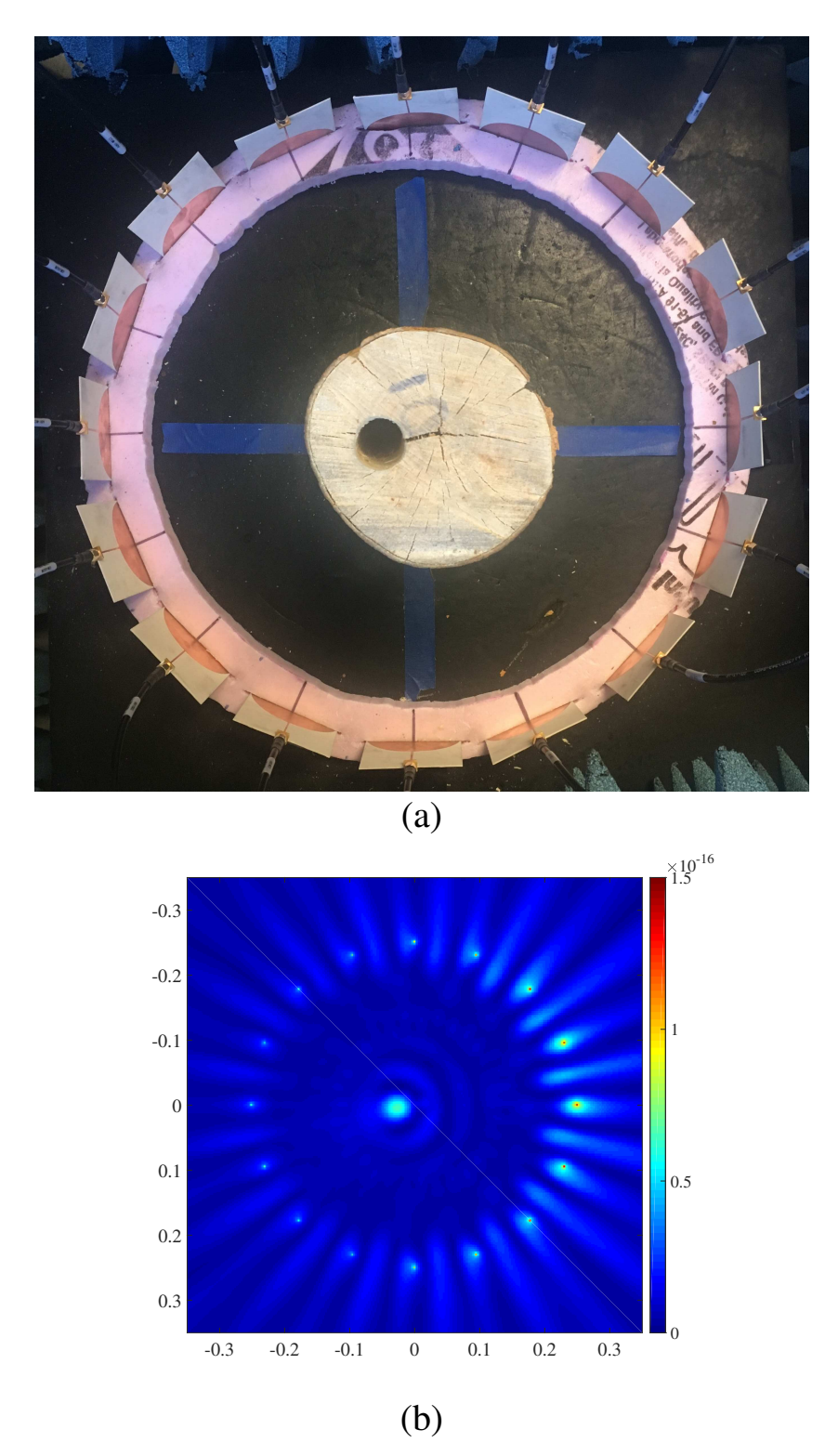


Figure 4.15 Imaging results of a bolt added to a 1" hole in a completely dried sugar maple sample (a). (b) Reconstruction.

Figs. 4.16 and 4.17 show the imaging results of nails added to a sample subtracted from a solid sample of basswood and sugar maple trees, respectively. Again, these samples were completely dried in order to properly image the metal inclusions. Unlike the above bolt images, these images were obtained by subtracting solid portions from the nail-added portions, which is a more realistic testing scenario. Fig. 4.18 shows the imaging result of a nail added horizontally to the outside of a basswood log subtracted from a solid sample of basswood log. The orientation of this nail is a more lifelike scenario, but the quality of the image is drastically less clear than the vertical nails. This is likely due to the size of the nail and the very little energy that is actually being reflected off of it. This issue and the sensitivity will need to be explored further.

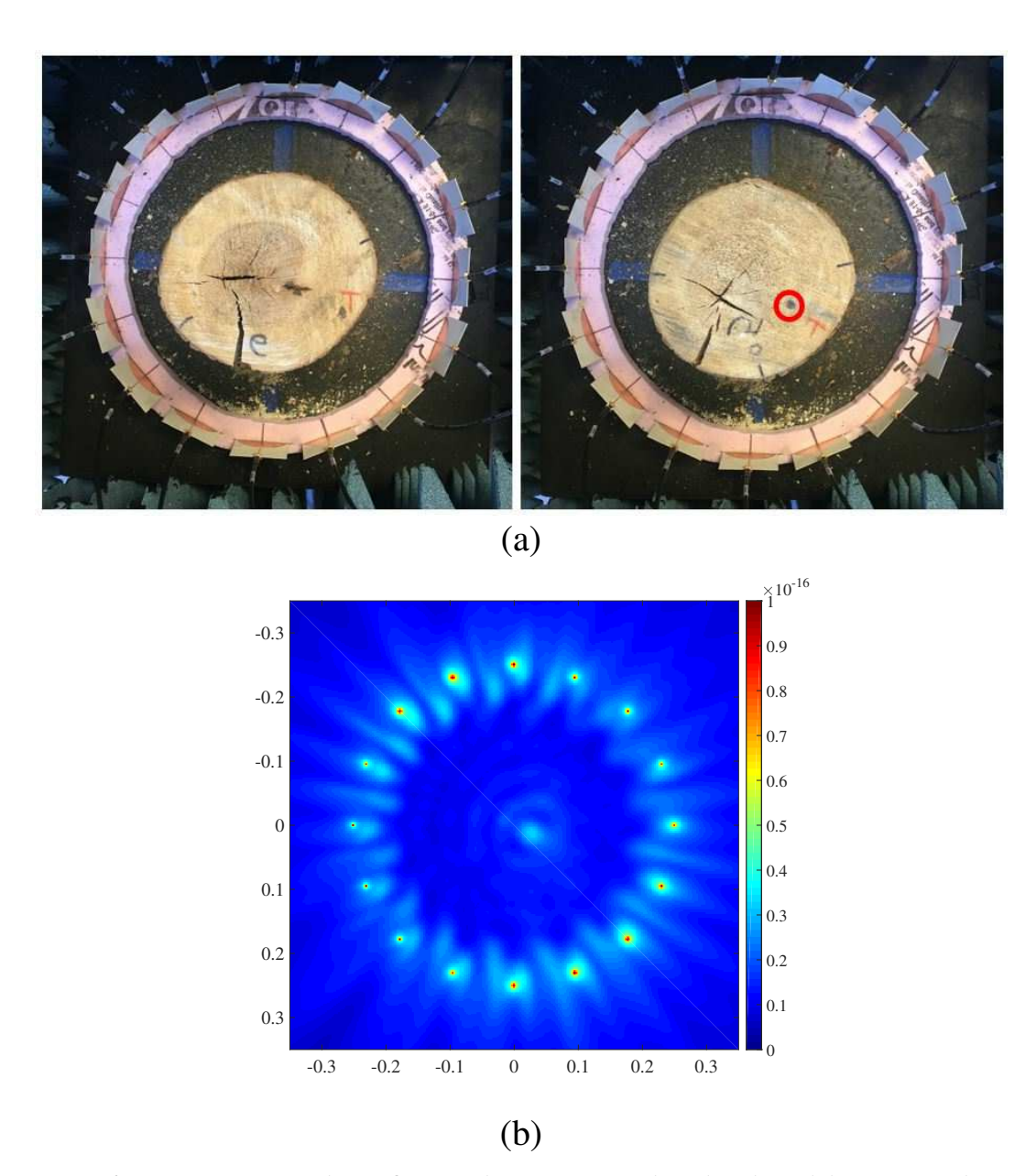


Figure 4.16 Imaging results of a nail in a completely dried basswood sample. The solid portion of the trunk (right (a)) was subtracted from the portion with the nail (left (a)). (b) Reconstruction.

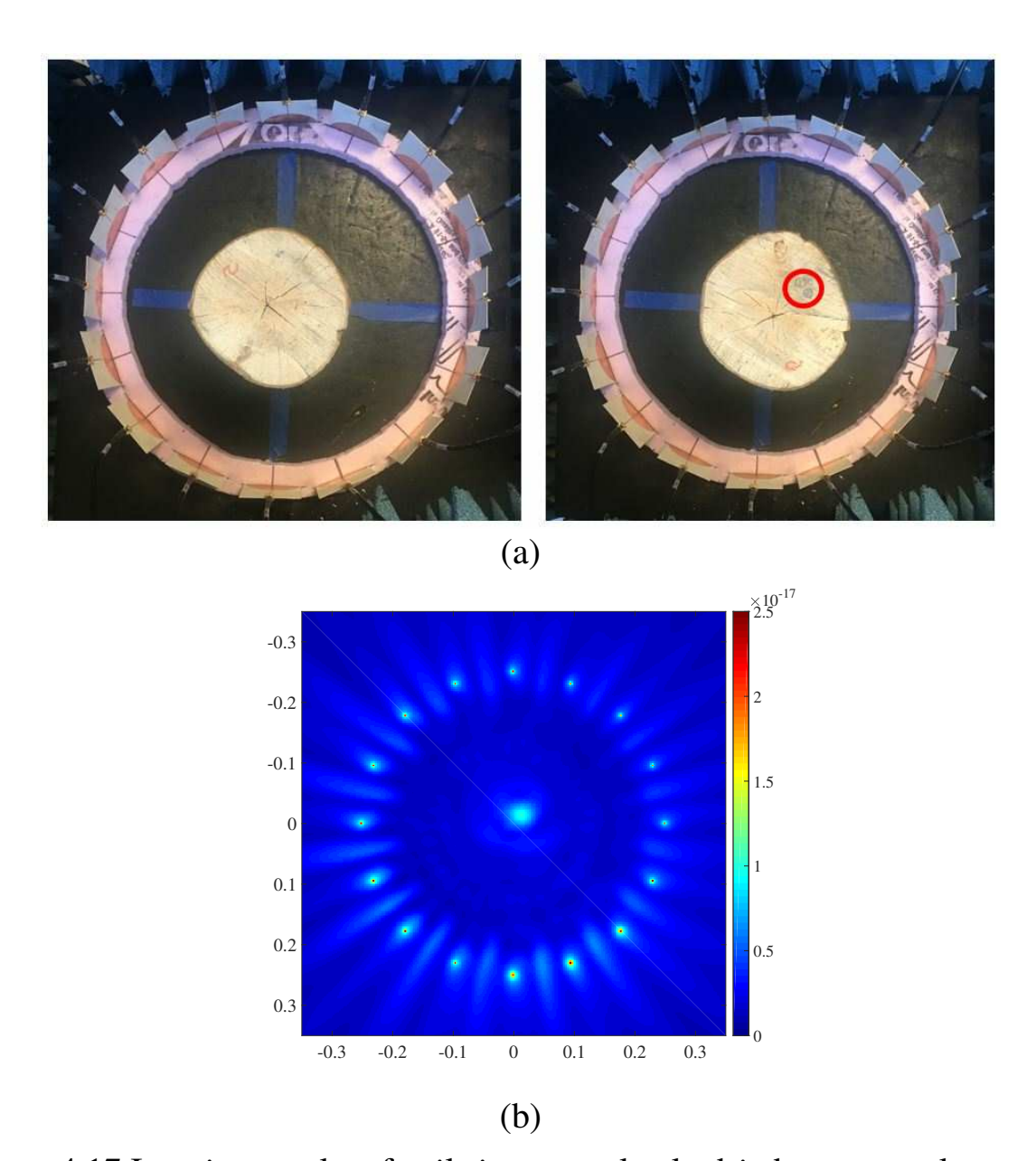


Figure 4.17 Imaging results of nails in a completely dried sugar maple sample. The solid portion of the trunk (left (a)) was subtracted from the portion with nails (right (a)). (b) Reconstruction.

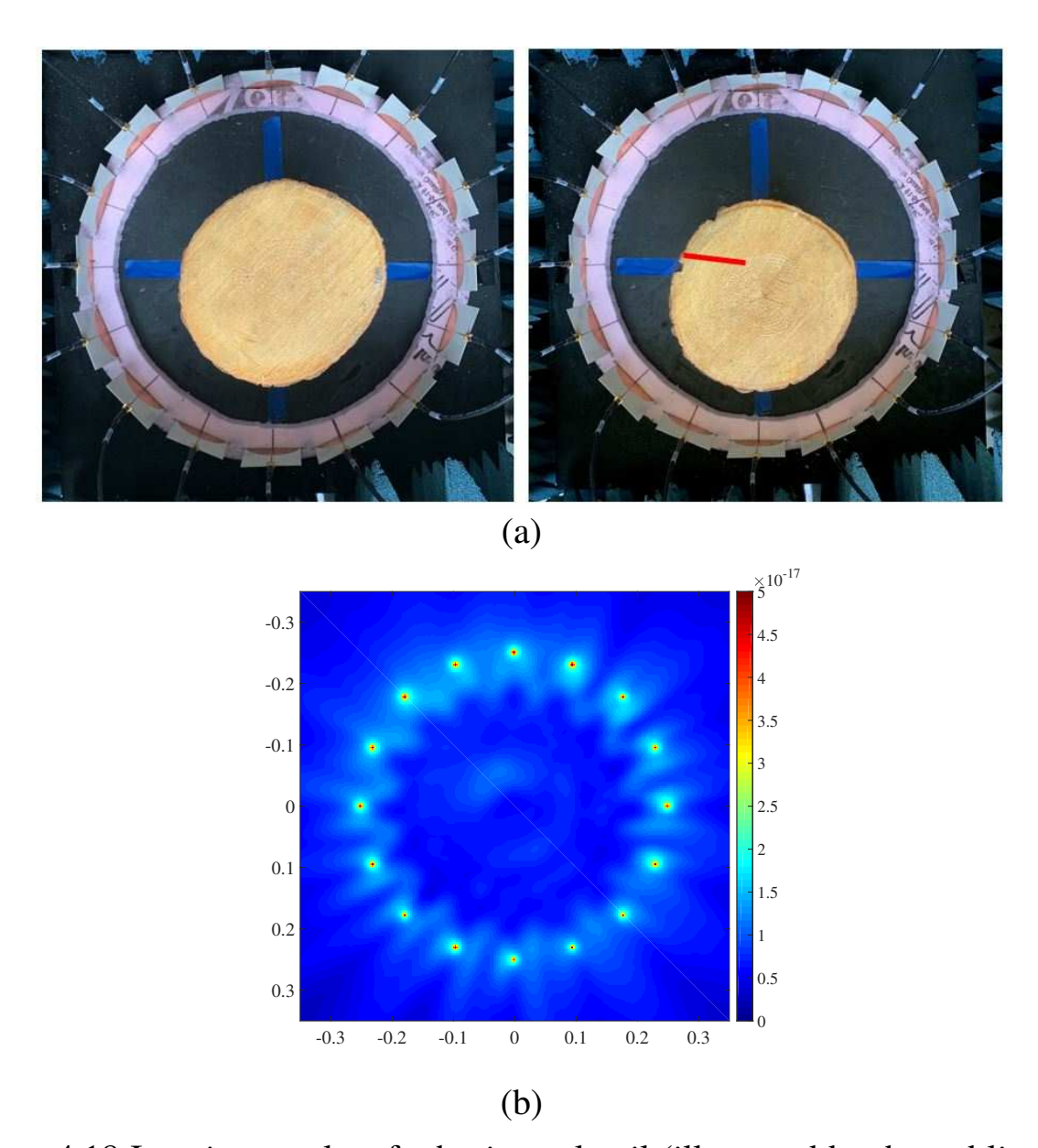


Figure 4.18 Imaging results of a horizontal nail (illustrated by the red line) in a completely dried basswood sample. The solid portion of the trunk (right (a)) was subtracted from the portion with the nail (left (a)). (b) Reconstruction.

## 4.4 Review

In this chapter, the use of the microwave tomography system was successfully demonstrated in many different scenarios, including tree trunk samples. The system is very successful at imaging simple targets such as homogeneous cylinders and rectangular prisms. While the system does not produce ideal results, there is evidence pointing toward the use of this system for the imaging of tree trunks. Usable results are not attainable unless the logs are completely dried of their water content. This is likely due to the lack of penetration of the waves into the sample due to the increase of lossy water within the trunk. More power could help mitigate these issues, the use of a very lossy switch matrix and the power limitations of the network analyzer could be contributing to these issues.

## **CHAPTER 5**

#### CONCLUSION

## 5.1 Overview

A microwave tomography system that is intended for use in several forestry applications was presented. This system consists of a frequency domain sampling transceiver, a 2-to-16 port switch matrix, and a ring of 1-5 GHz planar monopole antennas that are used to image an environment using microwave tomography. The system collects the transmission coefficient between each pair of antennas in the ring. After the data is collected, the wideband frequency domain data is transformed into time domain pulses for each transmit-receive pair. Once the time domain pulses are obtained, they are back propagated in free space using a 2D FDTD simulation, a process known as time reversal. At each time step of the time reversal simulation, the energy per mesh cell is calculated from the electric field. At the end of this process, the time integrated energy per mesh cell is averaged for each transmitting case. The energy focuses around scatterers in the imaging environment, providing a 2D tomographic image.

This system was used to image both simple targets such as cylinders and rectangular prisms made of brass, plastic, and wood to demonstrate the imaging capabilities of the system. These images were very conclusive and the location of the objects in the ring were easily discernible. The system was also used to image more complex targets, specifically samples of tree trunks of various species of wood. These results were less conclusive and required an extra subtraction step but there was evidence pointing towards the feasibility of using it for forestry applications. The images were much more successful using completely dried wood as compared to freshly cut green wood. The penetration

of the antennas is a major concern, the lossy switch matrix and limitations of the network analyzer are possible reasons for this issue, which will need to be further explored.

# 5.2 Cost Analysis

The price and complexity of this system was consistently the motivation behind the decisions made during this process. Since this system was designed for forestry applications, the cost and ease of use of the system was of the utmost importance. The system requires cheap hardware and software that requires as little computing power as possible.

The system hardware cost about \$5,000, not considering the transceiver. The largest hardware cost is the network analyzer and the cables that connect it to the antennas as well as the transceiver. This cost about \$4,500 in total for all the components, with the other \$500 accounting for the price of the antenna substrate as well as other small miscellaneous costs. This is a reasonable cost for a final product that would be used by natural parks, power companies, etc., however, this is ignoring the price of the transceiver. The transceiver used in this study is a large, heavy network analyzer that costs thousands to tens of thousands of dollars and is not portable, which is vital to performing in vivo measurements of trees. This is where the use of a software defined radio, discussed in Section 2.4, becomes important. Software defined radios are much cheaper and portable, making them a good alternate to the current system and a good option for the next prototype.

In terms of the software, the system was able to create an image in about an hour using the low computational method of time reversal. All the simulations were run on a single core of an Intel Core i5-2500T CPU that runs at 2.30 GHz. The computer had 8 GB of RAM to do the calculations. This is a relatively

low computational cost and can easily be found in an inexpensive portable laptop, another major selling point of the prototype. The low cost of signal processing in comparison with other imaging systems makes it very attractive for its intended application.

## **5.3** Future Work

Section 5.2 outlines the future work required for this system before it is able to perform in vivo measurements of tree trunk. The first goal is to make the system portable. The substitution of an SDR for the network analyzer will greatly improve the portability of the system. Since the processing power is low enough to be reasonably done on a laptop, it is not of great importance but vectorizing the code could cut down on processing requirements and help reduce the time from measurement to final image. The last requirement of the system to create a fully portable system is to create a housing system for the antennas on the ring. Currently, the ring rests on a stationary stage that has slots for the antennas. A better, portable ring will need to be designed for the next prototype of the system. This will add a slight cost to the final system but it should not be anywhere on the magnitude of the switch matrix, keeping the cost in a reasonable price range. With these few additions and optimizations, a portable, low cost, near-real-time microwave tomography system can be created.

**APPENDICES** 

#### **APPENDIX A**

# PYTHON CODE TO TAKE DATA OFF HP8753D NETWORK ANALYZER

```
# tomography_capture.py
#
# Utility to control switch matrix and capture
  measurements to be used to
# reconstruct images of tree/subject.
#
# Ver 1.0
# Updated 1/10/2018
#
# Change Log
#
                                          # Tracebacks
import sys
   and interrupt handling
                                          # Sigint (
import signal
  ctrl-c) handling
import traceback
                                          # Traceback
  printing
import time
                                          # Sleeping
  between samples
import datetime
                                          # Naming
  save folder
```

```
import serial
                                             # Switch
   matrix communication
                                             # Serial
import serial.tools.list_ports
  port listing
import hp8735_na as na
                                             # HP-8735-NA
   GPIB communication
from itertools import permutations
                                             #
  Combination of ports to switch
# Port constants
PORT = 'COM4'
BAUD = '115200'
# Sampling constants
SAMPLE DELAY = 10e-3 # seconds
# Text formatting
class color:
    PURPLE = ' \ 033[95m']
    CYAN = ' \ 033[96m']
    DARKCYAN = ' \setminus 033[36m']
    BLUE = ' \033[94m']
    GREEN = '\033[92m']
    YELLOW = ' \cdot 033[93m']
    RED = '033[91m']
    BOLD = ' \setminus 033[1m']
```

```
UNDERLINE = ^{\prime} \sqrt{033} [4m]^{\prime}
    END = ' \setminus 033[0m']
class tomography_capture(object):
    11 11 11
    Class to manage tomography_capture
    11 11 11
    def __init__(self, port, baud):
        super(tomography_capture, self).__init__()
        self.port = port
         self.baud = baud
        # Initialize serial port object
        self.ser = self.open_serial()
        # Initialize network analyzer, returns NA
           object
         self.ena = na.init_8735d()
        # Bind signal handler to gracefully shutdown
        signal.signal(signal.SIGINT, self.
           exit handler)
    def exit_handler(self, sig, frame):
        print('Closing serial port...')
```

```
self.ser.close()
    print('Exiting tomography_capture...')
    exit()
def open_serial(self):
    # List all available ports
    ports = serial.tools.list_ports.comports()
    print("Available serial ports")
    print('-'*60)
    for i, port in enumerate (ports):
        if port.name is None:
            print('{:}. {:}'.format(i+1, port.
              device))
        else:
            print('{:}. {:}'.format(i+1, port.
              name))
    print('-'*60)
    print('')
   # Open port
    try:
        # print(color.GREEN)
        print('Using: "{:}" @ {:} baud'.format(
          PORT, BAUD))
        print('')
        # print(color.END)
```

```
ser = serial. Serial (PORT, BAUD, timeout
          =1)
    except serial. serialutil. SerialException as
      e :
        print(e)
        print('Exiting...')
        exit()
    except Exception:
        print("Unknown exception in open_serial
           ")
        print ('-'*60)
        traceback.print_exc(file=sys.stdout)
        print('-'*60)
        exit()
    return ser
def collect_data(self, delay=100e-3):
    # Generate hex value array [0-F]
    hex_array = [format(x, '01X') for x in range]
      (0, 16)]
    # Get network analyizer smapling frequencies
    freq_array = na.get_freqs(self.ena)
            # Get current time for naming save
               folder
```

```
("%Y-%m-%d-%H%M%S")
        # Iterate over antenna rx/tx pairs
        for pair in permutations(hex_array, 2):
            print("Sampling ports: " + str(pair))
            # Select ports
            self.ser.write(('{:}{:}'.format(*pair)).
              encode ('utf-8')
            # Settling time delay
            time.sleep(delay)
            polReal , polImag = na.record_measurement
              (self.ena)
            na. save measurement (polReal, polImag,
              freq_array , pair , time_str)
def main():
    tc = tomography_capture(PORT, BAUD)
    tc.collect data(delay=SAMPLE DELAY)
if __name__ == "__main__":
    main()
```

time\_str = datetime.datetime.now().strftime

[style

# **APPENDIX B**

# SWITCH MATRIX SCHEMATIC AND PART NUMBERS

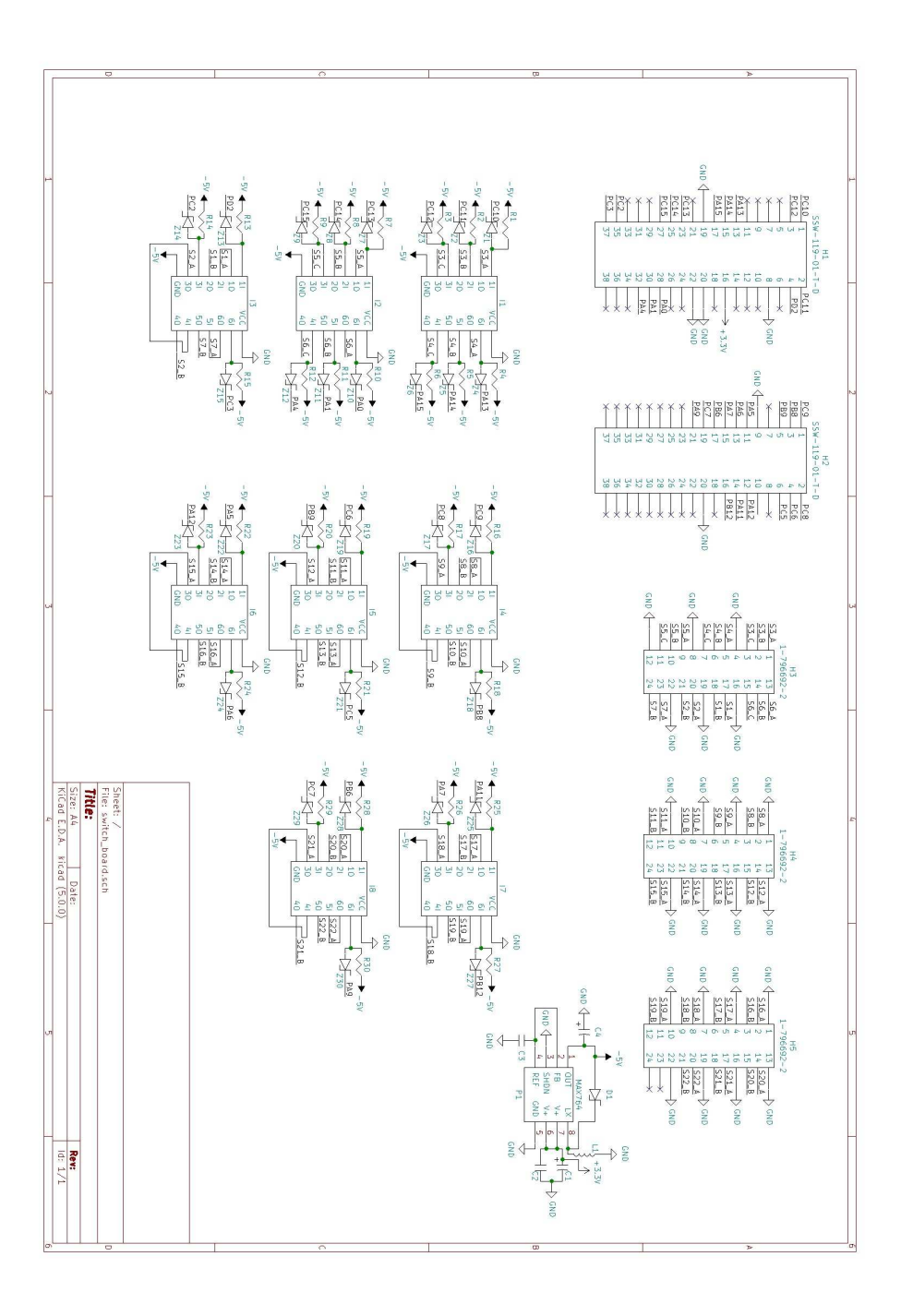


Figure B.1 Switch matrix schematic.

# **B.1** Part Numbers

R1-R29 ESR03EZPF1002

Z1-Z29 CMDZ5L1

I1-I8 SN74HCT04DRG4

P1 MAX764

C1 TPSD107K020R0085

C2-C3 T491A104M035AT

C4 T510X686K025ATE045

D1 1N5817

L1 CDRH8D58

H1-H2 SSW-119-01-T-D

H3-H5 1-796692-2

#### APPENDIX C

## NUCLEO CODE FOR CONTROLLING SWITCH MATRIX

```
#include "mbed.h"
void reset_switches();
void set_tx();
void set_rx();
Serial pc(SERIAL_TX, SERIAL_RX);
//TX and RX 2-way switches
DigitalOut tx_sw(PD_2);
DigitalOut rx_sw(PC_2);
//TX 8-way lower half switch
DigitalOut tx_low_A(PC_10);
DigitalOut tx_low_B(PC_11);
DigitalOut tx_low_C(PC_12);
//TX 8-way upper half switch
DigitalOut tx_high_A(PA_13);
DigitalOut tx_high_B (PA_14);
```

```
DigitalOut tx_high_C(PA_15);
//RX 8-way lower half switch
DigitalOut rx_low_A(PC_13);
DigitalOut rx_low_B(PC_14);
DigitalOut rx_low_C(PC_15);
//RX 8-way upper half switch
DigitalOut rx_high_A(PA_0);
DigitalOut rx_high_B(PA_1);
DigitalOut rx_high_C(PA_4);
// Antenna ports
DigitalOut port01(PC_3);
DigitalOut port02(PC_9);
DigitalOut port03 (PC_8);
DigitalOut port04(PB_8);
DigitalOut port05 (PC_6);
DigitalOut port06(PB_9);
DigitalOut port07(PC_5);
DigitalOut port08(PA_5);
DigitalOut port09(PA_12);
DigitalOut port10(PA_6);
DigitalOut port11 (PA_11);
```

```
DigitalOut port12(PA_7);
DigitalOut port13 (PB_12);
DigitalOut port14(PB_6);
DigitalOut port15(PC_7);
DigitalOut port16(PA_9);
char buff[4];
char tx_ant;
char rx_ant;
int main()
{
    // Set baud rate of UART
    pc.baud(115200);
    // reset_switches();
    while(1)
    {
        pc.printf("Waiting....\r\n");
        pc.gets(buff, 2);
        tx_ant = buff[0];
        //pc.printf("Got this far\r\n");
```

```
if (tx_ant == 'r')
{
    reset_switches();
    pc.printf("Now I am here\r\n");
    continue;
}
pc.gets(buff, 2);
rx_ant = buff[0];
if (rx_ant == 'r')
{
    reset_switches();
    pc.printf("Wooow.\r\n");
    continue;
}
pc.printf("Setting switches....\r\n");
```

```
reset_switches();
        set_tx();
        set_rx();
   }
}
void set_tx()
{
    switch (tx_ant)
    {
        case '0':
            break;
        case '1':
            tx_low_A = 0;
            break;
        case '2':
             tx\_low\_B = 0;
            break;
        case '3':
```

```
tx_low_A = 0;
    tx_low_B = 0;
    break;
case '4':
    tx\_low\_C = 0;
    break;
case '5':
   tx_low_A = 0;
    tx low C = 0;
    break;
case '6':
    tx\_low\_B = 0;
    tx_low_C = 0;
    break;
case '7':
   tx_low_A = 0;
    tx low B = 0;
    tx\_low\_C = 0;
    break;
case '8':
    tx_sw = 0;
    break;
case '9':
    tx_sw = 0;
    tx_high_A = 0;
    break;
case 'A':
```

```
tx_sw = 0;
    tx_high_B = 0;
    break;
case 'B':
    tx_sw = 0;
    tx_high_A = 0;
    tx_high_B = 0;
    break;
case 'C':
    tx_sw = 0;
    tx_high_C = 0;
    break;
case 'D':
    tx_sw = 0;
    tx_high_A = 0;
    tx_high_C = 0;
    break;
case 'E':
    tx_sw = 0;
    tx_high_B = 0;
    tx_high_C = 0;
    break;
case 'F':
    tx_sw = 0;
    tx_high_A = 0;
    tx_high_B = 0;
    tx_high_C = 0;
```

```
break;
        default:
             break;
    }
}
void set_rx()
{
    switch (rx_ant)
    {
        case '0':
             port01 = 0;
             break;
        case '1':
             port02 = 0;
            rx_low_A = 0;
             break;
        case '2':
             port03 = 0;
             rx_low_B = 0;
             break;
        case '3':
             port04 = 0;
            rx_low_A = 0;
             rx_low_B = 0;
             break;
        case '4':
```

```
port05 = 0;
    rx_low_C = 0;
    break;
case '5':
    port06 = 0;
    rx_low_A = 0;
    rx low C = 0;
    break;
case '6':
    port07 = 0;
    rx_low_B = 0;
    rx_low_C = 0;
    break;
case '7':
    port08 = 0;
    rx_low_A = 0;
    rx low B = 0;
    rx_low_C = 0;
    break;
case '8':
    port09 = 0;
    rx_sw = 0;
    break;
case '9':
    port10 = 0;
    rx_sw = 0;
    rx_high_A = 0;
```

```
break;
case 'A':
    port11 = 0;
    rx_sw = 0;
    rx_high_B = 0;
    break;
case 'B':
    port12 = 0;
    rx_sw = 0;
    rx_high_A = 0;
    rx_high_B = 0;
    break;
case 'C':
    port13 = 0;
    rx_sw = 0;
    rx_high_C = 0;
    break;
case 'D':
    port14 = 0;
    rx_sw = 0;
    rx_high_A = 0;
    rx_high_C = 0;
    break;
case 'E':
    port15 = 0;
    rx_sw = 0;
    rx_high_B = 0;
```

```
rx_high_C = 0;
            break;
        case 'F':
             port16 = 0;
            rx_sw = 0;
            rx_high_A = 0;
            rx_high_B = 0;
            rx_high_C = 0;
            break;
        default:
            break;
    }
}
void reset_switches()
{
    tx_sw = 1;
    rx_sw = 1;
    tx_low_A = 1;
    tx\_low\_B = 1;
    tx_low_C = 1;
    tx_high_A = 1;
    tx_high_B = 1;
```

```
tx_high_C = 1;
rx_low_A = 1;
rx_low_B = 1;
rx_low_C = 1;
rx_high_A = 1;
rx_high_B = 1;
rx_high_C = 1;
port01 = 1;
port02 = 1;
port03 = 1;
port04 = 1;
port05 = 1;
port06 = 1;
port07 = 1;
port08 = 1;
port09 = 1;
port10 = 1;
port11 = 1;
port12 = 1;
```

```
port13 = 1;
port14 = 1;
port15 = 1;
port16 = 1;
```

## APPENDIX D

## MATLAB CODE TO PLACE ANTENNA LOCATIONS

```
close all
clear all
clc
circle_d = .500;
                       %distance between opposite
  pair ends
circle_r=circle_d/2; %radius
antenna_n = 16;
                     %number of antennas
antenna_location=zeros(antenna_n,2);
for i_antenna=0:antenna_n-1
    antenna_location(i_antenna+1,1)=circle_r*cos(pi
      /2+2*pi*i_antenna/antenna_n);
    antenna_location(i_antenna+1,2)=circle_r*sin(pi
      /2+2*pi*i_antenna/antenna_n);
end
save vars/antenna_location.mat antenna_location
```

## **APPENDIX E**

## MATLAB CODE TO READ IN DATA

```
close all
clc
% s parameter matracies are material (freq, rx, tx)
  where S_21 is tx=1 rx=2
%
empty_zeros = zeros(2001, 16, 16);
block_zeros = zeros(2001, 16, 16);
for i_rx = 1:16
    for i_t x = 1:16
         if i_t x \sim = i_r x
             name='vars/empty/sample_%d_%d.csv';
              str = sprintf (name, i_tx, i_rx);
              data=csvread(str);
             empty_zeros (401:2001, i_rx, i_tx)=data
                (:,2)+1j*data(:,3);
             name='vars/PEC/sample_%d_%d.csv';
```

```
str = sprintf(name, i_tx, i_rx);
             data=csvread(str);
             block_zeros (401:2001, i_rx, i_tx)=data
                (:,2)+1j*data(:,3);
         e1se
         end
    end
    disp(i_rx)
end
%%
empty_full = zeros(4001, 16, 16);
empty_full(2001:4001,:,:)=empty_zeros;
block_full = zeros(4001, 16, 16);
block full (2001:4001,:,:)=block zeros;
window=zeros(4001,1);
window (2001:4001) = ones(1,2001);
for i_freq = 1:2000
    for i rx = 1:16
         for i tx = 1:16
             empty_full(2001-i_freq, i_rx, i_tx) = conj(
                empty_full(2000+i_freq,i_rx,i_tx));
             block_full(2001-i_freq, i_rx, i_tx) = conj(
```

```
block_full(2000+i_freq,i_rx,i_tx));
            window(2001-i_freq)=window(2000+i_freq);
        end
    end
end
empty_time=zeros(4001,16,16);
empty TR full=zeros(4001, 16, 16);
empty_TR_pulse=zeros(250,16,16);
block\_time = zeros(4001, 16, 16);
block_TR_full = zeros(4001, 16, 16);
block_TR_pulse=zeros(250,16,16);
for i rx = 1:16
    for i_t x = 1:16
        empty_time(:,i_rx,i_tx)=ifftshift(ifft(
           empty_full(:,i_rx,i_tx).*window(:),
           symmetric'));
        empty_TR_full(:,i_rx,i_tx)=flip(empty_time
           (:,i_rx,i_tx));
        empty_TR_pulse(:,i_rx,i_tx)=empty_TR_full
           (1450:1699, i_rx, i_tx);
```

```
block time (:, i rx, i tx)=ifftshift(ifft(
           block_full(:,i_rx,i_tx).*window(:),'
           symmetric'));
        block_TR_full(:,i_rx,i_tx)=flip(block_time
           (:, i_rx , i_tx));
        block_TR_pulse(:,i_rx,i_tx)=block_TR_full
           (1450:1699, i_rx, i_tx);
    end
end
save vars/empty_TR.mat empty_TR_pulse
save vars/block_TR.mat block_TR_pulse
figure;
for i rx = 1:16
    plot (linspace (0, 499, 250)/10, (flip (empty_TR_pulse
       (:, i_rx, 1)) + i_rx *.02, `LineWidth', 1.25)
    hold on
end
xlabel('Time (ns)')
set (gca, 'FontSize', 24)
figure;
```

```
for i rx = 1:16
       plot(abs(block_TR_pulse(:,i_rx,8))+i_rx*.01)
%
    plot (linspace (0,499,250)/10, (flip (block_TR_pulse
       (:, i_rx, 1)) + i_rx *.02, `LineWidth', 1.25)
    hold on
end
xlabel('Time (ns)')
set (gca, 'FontSize', 24)
figure;
for i rx = 1:16
       plot (abs (block_TR_pulse (:, i_rx, 8)) - abs (
%
  empty_TR_pulse(:,i_rx,8))+i_rx*.01)
    plot (linspace (0,499,250)/10, (flip (block_TR_pulse
       (:, i_rx ,1))-flip(empty_TR_pulse(:,i_rx ,1)))+
       i rx *.02, 'LineWidth', 1.25)
    hold on
end
xlabel('Time (ns)')
set (gca, 'FontSize', 24)
```

#### **APPENDIX F**

# MATLAB CODE TO BACK PROPAGATE THE MEASURED DATA

```
close all
clear all
clc
% Load data and locations
% load time_matrix.mat
load vars/antenna_location.mat
load vars/empty_TR.mat
load vars/block_TR.mat
tic
% Medium Parameters
c = 3e8;
                                       %speed of light
f_c = 3e9;
                                       %center
  frequency
mu0=4*pi*1e-7;
                                       %mu naught
epsilon0 = 8.85e - 12;
                                       %epsilon naught
epsilon_r = 1;
```

```
% FDTD Mesh Parameters
                                       %scaling factor
kk=4;
delta_p = ((c/f_c)/10)/kk;
                                          %grid size
  based on center frequency
delta_t = ((delta_p)/(c*sqrt(2)));
                                      %sampling time
timesteps = floor((1/10e9)/(delta_t)*250);
ts_i fft = (0:249)*1/10e9;
ts_fdtd = (0:timesteps_{-1})*delta_t;
input=zeros(timesteps, 16, 16);
for i rx = 1:16
    for i tx = 1:16
         input(:,i_rx,i_tx)=interp1(ts_ifft,
           block_TR_pulse(:,i_rx,i_tx)-
           empty_TR_pulse(:,i_rx,i_tx),ts_fdtd);
%
           input(:,i_rx,i_tx)=interp1(ts_ifft,
  empty_TR_pulse(:,i_rx,i_tx),ts_fdtd);
    end
end
\% timesteps = 8485;
```

```
% Spatial Grid
xlim = .600;
             %.330
ylim = .600;
xref=-xlim:delta_p:xlim;
yref=-ylim:delta_p:ylim;
if mod(length(xref),2) \sim = 1
    xlim=xlim+delta_p;
    xref(length(xref)+1)=xlim;
end
if mod(length(yref),2) \sim = 1
    ylim=ylim+delta_p;
    yref(length(yref)+1)=ylim;
end
xn=length(xref);
yn=length (yref);
% Finding positions of each antenna
antenna_n = 16;
antenna_grid_x = zeros (antenna_n, 1);
```

```
antenna_grid_y=zeros (antenna_n, 1);
antenna_x = zeros (antenna_n, 1);
antenna_y=zeros (antenna_n, 1);
for im=1:antenna_n
    [~, antenna_grid_x (im)]=min(abs(xref-
       antenna_location(im,1));
    [~, antenna_grid_y (im)]=min(abs(xref-
       antenna location (im, 2));
    antenna_x (im) = antenna_grid_x (im) * delta_p - xlim;
    antenna_y (im) = antenna_grid_y (im) * delta_p - ylim;
end
% FDTD initialization
sumador=zeros (yn, xn);
Ez new2D=zeros (yn, xn);
Ez_old2D = zeros(yn, xn);
Hx_new2D = zeros(yn-1,xn);
Hx_old2D = zeros(yn-1,xn);
Hxm new2D=zeros(2,xn);
Hxm old2D=zeros (2, xn);
Hy new2D=zeros (yn, xn-1);
Hy old2D=zeros (yn, xn-1);
Hym_new2D = zeros(yn,2);
```

 $Hym_old2D = zeros(yn, 2);$ 

 $er_m = ones(yn, xn);$ 

```
sigma_m = zeros(yn, xn);
ij = 1;
% Coefficients for Maxwell's Equations
coef1 = ((c*delta_t) - delta_p) / ((c*delta_t) + delta_p);
  % Coeficient of MUR boundary condition
coef2 = (delta_t / (mu0*delta_p));
                                                         %
  %Coeficient of correction eq. for H field
coef3 = (delta_t ./(epsilon0*er_m*delta_p));
coefinc = (delta_t ./(epsilon0*er_m));
coeff3 = (1 - sigma_m .* delta_t ./(2 * er_m)) ./(1 + sigma_m .*
   delta_t./(2*er_m));
coeff4 = 1./(1 + sigma_m.* delta_t./(2 * er_m)).*(delta_t
   ./(epsilon0*er_m.*delta_p));
A = [];
% FDTD Simulations
for i_antenna=1:antenna_n
clc
i_antenna
toc
sumador=zeros (yn, xn);
Ez_new2D = zeros(yn, xn);
Ez_old2D = zeros(yn, xn);
```

```
Hx new2D=zeros (yn-1,xn);
Hx_old2D = zeros(yn-1,xn);
Hxm_new2D = zeros(2, xn);
Hxm_old2D = zeros(2,xn);
Hy_new2D = zeros(yn, xn-1);
Hy_old2D = zeros(yn, xn-1);
Hym_new2D = zeros(yn, 2);
Hym_old2D = zeros(yn, 2);
er m = ones(yn, xn);
sigma_m = zeros(yn, xn);
i i = 1;
for n=1: time steps
%
      t ref(n)=n*delta t;
    % Updating H Fields
    Hy new2D((1:(yn-1)),(1:(xn-1)))=Hy old2D((1:(yn
       -1)), (1:(xn-1))+coef2*(Ez_new2D((1:(yn-1)))
       (2:(xn))-Ez_new2D((1:(yn-1)),(1:(xn-1)));
      %Update of the Hy fields no boundaries
    Hx_new2D((1:(yn-1)),(1:(xn-1)))=Hx_old2D((1:(yn-1)))
       -1)), (1:(xn-1)))-coef2*(Ez_new2D((2:(yn)))
       (1:(xn-1))-Ez new2D((1:(yn-1)),(1:(xn-1)))
       ; %Update of the Hx fields no boundaries
    Hym_new2D((1:yn),1)=Hy_old2D((1:yn),1)+coef1*(
      Hy_new2D((1:yn),1)-Hym_old2D((1:yn),1));
```

```
%Hy ABCs for left and right
Hym_new2D((1:yn),2)=Hy_old2D((1:yn),xn-1)+coef1
  *(Hy_new2D((1:yn),xn-1)-Hym_old2D((1:yn),2));
      %Hy ABCs for top and bottom
Hxm new2D(1,(1:xn))=Hx old2D(1,(1:xn))+coef1*(
  Hx_new2D(1,(1:xn))-Hxm_old2D(1,(1:xn));
           %Hx ABCs for left and right
Hxm new2D(2,(1:xn))=Hx old2D(yn-1,(1:xn))+coef1
  *(Hx_new2D(yn-1,(1:xn))-Hxm_old2D(2,(1:xn)));
      %Hx ABCs for top and bottom
                             %%Old fields become
Hy_old2D=Hy_new2D;
  the fields just found at each iteration
Hx \text{ old2D=}Hx \text{ new2D};
Hym_old2D=Hym_new2D;
Hxm old2D=Hxm new2D;
% Updating E fields
% elseif l==1 \&\& j\sim=1 \&\& j\sim=yn
% The E field is found using one of the ABCs
1 = 1;
jj = 2:(yn-1);
Ez_{new2D(jj,1)}=Ez_{old2D(jj,1)}+coef3(jj,1).*(
  Hy_new2D(jj,1)-Hym_new2D(jj,1))-coef3(jj,1)
  .*(Hx_new2D(jj,1)-Hx_new2D(jj-1,1));
```

```
%elseif l == xn \&\& j == 1 \&\& j == yn
% The E field is found using one of the boundary
    conditions
l = xn;
jj = 2:(yn-1);
Ez_{new2D(jj,1)}=Ez_{old2D(jj,1)}+coef3(jj,1).*(
  Hym_new2D(jj, 2) - Hy_new2D(jj, 1-1)) - coef3(jj, 1)
  *(Hx_new2D(jj, 1)-Hx_new2D(jj-1, 1));
\%elseif j==1 && 1~=1 && 1~=xn
% The E field is found using the ABC for the
  places around the boundaries
j = 1;
11 = 2 : (xn - 1);
Ez_{new2D(j,11)}=Ez_{old2D(j,11)}+coef3(j,11).*(
  Hy_new2D(j, 11) - Hy_new2D(j, 11-1)) - coef3(j, 11)
   *(Hx_new2D(j, 11)-Hxm_new2D(1, 11));
% elseif j == yn && 1 == 1 && 1 == xn
% The E field is found using the ABC for the
  places around the boundaries
j = yn;
11 = 2:(xn-1);
Ez_{new2D(j,11)}=Ez_{old2D(j,11)}+coef3(j,11).*(
  Hy_new2D(j, 11) - Hy_new2D(j, 11-1)) - coef3(j, 11)
  .*(Hxm_new2D(2,11)-Hx_new2D(j-1,11));
```

```
\% elseif l==1 && j==1
% The E field is found using the ABC for the
  places around the boundaries
1 = 1;
j = 1;
Ez_{new2D(j,1)}=Ez_{old2D(j,1)}+coef3(j,1)*(Hy_{new2D})
  (i, 1)-Hym_new2D(i, 1))-coef3(i, 1)*(Hx_new2D(i, 1))
  1)-Hxm_new2D(1,1));
\%elseif l==xn \&\& j==yn
% The E field is found using the ABC for the
  places around the boundaries
1 = xn;
j = yn;
Ez new2D(j,1)=Ez old2D(j,1)+coef3(j,1)*(
  Hym_new2D(j, 2)-Hy_new2D(j, 1-1))-coef3(j, 1)*(
  Hxm_new2D(2,1)-Hx_new2D(j-1,1);
\% elseif l==1 && j==yn
% The E field is found using the ABC for the
  places around the boundaries
1 = 1;
j = yn;
Ez_{new2D(j,1)}=Ez_{old2D(j,1)}+coef3(j,1)*(Hy_{new2D(j,1)})
  (i, 1)-Hym_new2D(i, 1))-coef3(i, 1)*(Hxm_new2D
```

```
(2,1)-Hx_new2D(j-1,1);
 \%elseif 1 == xn \&\& j == 1
 % The E field is found using the ABC for the
    places around the boundaries
 1 = xn;
 j = 1;
 Ez_{new2D(j,1)}=Ez_{old2D(j,1)}+coef3(j,1)*(
   Hym new2D(i, 2)-Hy new2D(i, 1-1))-coef3(i, 1)*(
   Hx_new2D(j, 1)-Hxm_new2D(1, 1);
%else
 % The electric field is found for all the other
    places in the computational domain.
    are the locations that are not around the
   boundaries.
 ii = 2:(yn-1);
 11 = 2:(xn-1);
 Ez_{new2D(jj,11)}=Ez_{old2D(jj,11)}+coef3(jj,11).*(
   Hy_new2D(jj, 11) - Hy_new2D(jj, 11-1)) - coef3(jj,
   11) .*(Hx_new2D(jj, 11) - Hx_new2D(jj-1, 11));
 % Placing Fields at Receivers
 if (n \le length (input) - 16)
      ll=antenna_grid_x;
                                  j=antenna_grid_y;
               l = length(11);
     for i = 1:1
```

```
if i~=i antenna
             Ez_{new2D(j(i), 11(i))} = (Ez_{old2D(j(i), i)})
                11(i)+coef3(j(i),11(i))*(
               Hy_new2D(j(i),11(i))-Hy_new2D(j(i
               ), 11(i)-1))-coef3(i(i), 11(i))*(
               Hx_new2D(j(i), 11(i))-Hx_new2D(j(i)
                )-1,11(i))))- 5*coefinc(j(i),11(i
               ))*input(n,i,i_antenna);
         end
    end
end
% Localization techniques
    % Integrated Energy
Ez old2D=Ez new2D;
if n > 1000
sumador = ((Ez_old2D).^2*delta_t)+sumador;
end
energia { i_antenna }= sumador;
% Entropy
ent2(n) = (sum(sum((Ez new2D.^2)))^2)/(sum(sum(
  Ez new2D.^4)));
entropy { i_antenna } = ent2;
p = (Ez_new2D.^2)./(sum(sum(Ez_new2D.^2)));
                                               p(p
  ==0)=1e-13;
```

```
ent3(n)= - sum(sum(p.*log(p)))/(max(max(p)));
                                                       if((mod(n,10) == 0))
%
%
                                                                                        n
%
                                                       end
                                              Display Iterative Electric Fields
%
                     if((mod(n,1000)==0))
%
                                                                                        uu=real(Ez old2D);
                                                                                         imagesc(yref, xref, uu);
%
                                                                                         colormap (hsv (128))
%
                                                                                         hold on
%
                                                                                          plot(antenna_grid_x, antenna_grid_y, 'ow')
%
                                                                                          plot(antenna_x, antenna_y, 'ow')
% \frac{1}{2} \left( \frac{1}{2} \right) = \frac{
                                                                                                            circle([0,0],r_t,1000,'w-'); % Target
% %
                                                                         iteration = n
%
                                                                                          colorbar
%
                                                                                        frame = getframe;
                    end
90
                                     if n > 8480
%
                                                                         iteration=n
%
                                     end
% % Fields at entropy minima
% if (n=3475 \mid | n=5038)
                                                  A(ij,:,:) = Ez_new2D;
%
```

```
%
    ij = ij + 1;
% end
end % End of iterations
% %% Focusing Images
figure; plot(ent2/max(ent2)) % Entropy plot
title ('Entropy Plot')
% figure; imagesc(xref, yref, energia { i_antenna })%
  Energy plot
% colorbar
% colormap jet
\% \ caxis([0 \ 1e-15])
% hold on
% % plot(source_pos_x, source_pos_y, 'ok'); plot(
  sensor_x, sensor_y, '+k'); plot(0,0,'+k'); % Target
% title ('Time Integrated Energy')
% Plot of fields
\% field1 (:,:) = A(1,:,:);
% figure; imagesc(xref, yref, (field1))
% title ('Field at Entropy Minima Time')
% hold on
% % plot(source_pos_x, source_pos_y, 'ok'); plot(
  sensor_x, sensor_y, '+k'); plot(0,0,'+k'); % Target
```

#### end

```
900
energy=zeros(size(energia{i_antenna}));
for im=1:antenna_n
       energy=energy+energia {im } (: ,:) / max(max(energia
  { im } (:,:) ));
    energy=energy+energia(im)(:,:);
end
energy = energy / antenna_n;
% figure;
% plot(ent2/max(ent2))
figure; imagesc (xref, yref, energy)
hold on
% plot(antenna_grid_x, antenna_grid_y)
plot (antenna_x, antenna_y, 'or', 'MarkerSize', 15)
colorbar
colormap jet
axis equal
axis ([-.35 .35 -.35 .35])
\% caxis([0 .9e-16]);
caxis([0 100e-22])
toc
```

**BIBLIOGRAPHY** 

## **BIBLIOGRAPHY**

- [1] D. J. Nowak and E. J. Greenfield, "Tree and impervious cover change in us cities," <u>Urban Forestry & Urban Greening</u>, vol. 11, no. 1, pp. 21–30, 2012.
- [2] J. F. Dwyer, E. Mcpherson, H. Schroeder, and R. A. Rowntree, "Assessing the benefits and costs of the urban forest," J. Arbor., vol. 18, 01 1992.
- [3] F. E. Kuo, "Social aspects of urban forestry: The role of arboriculture in a healthy social ecology," 2003.
- [4] D. W. MacFarlane and B. Kane, "Neighbour effects on tree architecture: functional trade-offs balancing crown competitiveness with wind resistance," Functional Ecology, vol. 31, no. 8, pp. 1624–1636, 2017. [Online]. Available: https://besjournals.onlinelibrary.wiley.com/doi/abs/10.1111/1365-2435.12865
- [5] G. Dahle, J. Grabosky, B. Kane, J. Miesbauer, W. Peterson, F. W. Telewski, A. Koeser, and G. W. Watson, "Tree biomechanics: A white paper from the 2012 international meeting and research summit at the morton arboretum (lisle, illinois, us)." <u>Arboriculture & Urban Forestry</u>, vol. 40, pp. 309–318, 11 2014.
- [6] V. Bucur, "Techniques for high resolution imaging of wood structure: a review," Measurement Science and Technology, vol. 14, no. 12, pp. R91–R98, oct 2003. [Online]. Available: https://doi.org/10.1088%2F0957-0233%2F14%2F12%2Fr01
- [7] G. L. Clark, "X rays-what should we know about them?" Transactions of the American Institute of Electrical Engineers, vol. 54, no. 1, pp. 3–14, Jan 1935.
- [8] R. Chandra, H. Zhou, I. Balasingham, and R. M. Narayanan, "On the opportunities and challenges in microwave medical sensing and imaging," IEEE Transactions on Biomedical Engineering, vol. 62, no. 7, pp. 1667–1682, July 2015.
- [9] A. C. Kak, M. Slaney, and G. Wang, "Principles of computerized tomo-

- graphic imaging," Medical Physics, vol. 29, no. 1, pp. 107–107, 2002.
- [10] M. Onoe, H. Yamada, H. Nakamura, H. Kawamura, and M. Yoshimatsu, "Computed tomography for measuring annual rings of a live tree," Proceedings of the IEEE, vol. 71, no. 7, pp. 907–908, July 1983.
- [11] F. G. Wagner, F. W. Taylor, D. S. Ladd, C. W. McMillin, and F. L. Roder, "Ultrafast ct scanning of an oak log for internal defects," vol. 39, pp. 62–64, 11 1989.
- [12] S. Rust, "Comparison of three methods for determining the conductive xylem area of scots pine (pinus sylvestris)," Forestry, vol. 72, no. 2, pp. 103–108, 1999.
- [13] G. Catena and A. Catena, "Evidenziazione mediante la termografia di cavità e tessuti degradati negli alberi," Agricoltura ricerca, vol. 185, pp. 47–64, 2000.
- [14] A. Catena, "Thermography reveals hidden tree decay," <u>Arboricultural Journal</u>, vol. 27, no. 1, pp. 27–42, 2003. [Online]. Available: <a href="https://doi.org/10.1080/03071375.2003.9747360">https://doi.org/10.1080/03071375.2003.9747360</a>
- [15] A. A. Ray, D. Ghiculete, K. T. Pace, and R. J. D. Honey, "Limitations to ultrasound in the detection and measurement of urinary tract calculi," Urology, vol. 76, no. 2, pp. 295–300, 2010.
- [16] E. Biagi, G. Gatteschi, L. Masotti, A. Zanini, M. Cerofolini, and A. Lorenzi, "Tomografia ad ultrasuoni per la caratterizzazione difettologica del legno," <u>Alta frequenza–Rivista di elettronica</u>, vol. 6, no. 2, pp. 48–57, 1994.
- [17] E. Comino, L. Socco, R. Martinis, G. Nicolotti, and L. Sambuelli, "Ultrasonic tomography for wood decay diagnosis," MITTEILUNGEN-BIOLOGISCHEN BUNDESANSTALT FUR LAND UND FORSTWIRTSCHAFT, pp. 279–279, 2000.
- [18] V. Socco, R. Martinis, L. Sambuelli, E. Comino, and G. Nicolotti, "Open problems concerning ultrasonic tomography for wood decays diagnosis. 12th symp," NDT of Wood, University of Western Hungary, Sopron, vol. 468, 2000.

- [19] L. Socco, L. Sambuelli, and G. Nicolotti, "Ultrasonic tomography for non destructive testing of living trees," GNGTS–Atti del, vol. 19, 2004.
- [20] L. V. Socco, L. Sambuelli, R. Martinis, E. Comino, and G. Nicolotti, "Feasibility of ultrasonic tomography for nondestructive testing of decay on living trees," Research in Nondestructive Evaluation, vol. 15, no. 1, pp. 31–54, 2004. [Online]. Available: https://doi.org/10.1080/09349840490432678
- [21] D. I. Hoult and B. Bhakar, "Nmr signal reception: Virtual photons and coherent spontaneous emission," Concepts in Magnetic Resonance: An Educational Journal, vol. 9, no. 5, pp. 277–297, 1997.
- [22] R. Pearce, B. Fisher, T. Carpenter, and L. Hall, "Water distribution in fungal lesions in the wood of sycamore, acer pseudoplatanus, determined gravimetrically and using nuclear magnetic resonance imaging," New phytologist, vol. 135, no. 4, pp. 675–688, 1997.
- [23] M. Merela, P. Oven, A. Sepe, and I. Serša, "Three-dimensional in vivo magnetic resonance microscopy of beech (fagus sylvatica 1.) wood," Magnetic Resonance Materials in Physics, Biology and Medicine, vol. 18, no. 4, pp. 171–174, 2005.
- [24] M. Pastorino, A. Randazzo, A. Fedeli, A. Salvadè, S. Poretti, M. Maffongelli, R. Monleone, and M. Lanini, "A microwave tomographic system for wood characterization in the forest products industry," <u>Wood Material Science & Engineering</u>, vol. 10, no. 1, pp. 75–85, 2015.
- [25] F. Boero, A. Fedeli, M. Lanini, M. Maffongelli, R. Monleone, M. Pastorino, A. Randazzo, A. Salvadè, and A. Sansalone, "Microwave tomography for the inspection of wood materials: imaging system and experimental results," IEEE Transactions on Microwave Theory and Techniques, vol. 66, no. 7, pp. 3497–3510, 2018.
- [26] E. C. Fear, S. C. Hagness, P. M. Meaney, M. Okoniewski, and M. A. Stuchly, "Enhancing breast tumor detection with near-field imaging," <u>IEEE Microwave Magazine</u>, vol. 3, no. 1, pp. 48–56, March 2002.
- [27] Z. Wang, E. G. Lim, Y. Tang, and M. Leach, "Medical applications of microwave imaging," The Scientific World Journal, vol. 2014, 2014.

- [28] E. C. Fear, P. M. Meaney, and M. A. Stuchly, "Microwaves for breast cancer detection?" IEEE Potentials, vol. 22, no. 1, pp. 12–18, Feb 2003.
- [29] T. C. Guo, W. W. Guo, and L. E. Larsen, "Microwave-induced thermoacoustic effect in dielectrics and its coupling to external medium a thermodynamical formulation," <u>IEEE Transactions on Microwave Theory and Techniques</u>, vol. 32, no. 8, pp. 835–843, Aug 1984.
- [30] R. Kruger, W. Kiser, D. Reinecke, G. Kruger, and R. Eisenhart, "Thermoacoustic computed tomography of the breast at 434 mhz," in 1999 IEEE MTT-S International Microwave Symposium Digest (Cat. No. 99CH36282), vol. 2. IEEE, 1999, pp. 591–594.
- [31] R. A. Kruger, K. K. Kopecky, A. M. Aisen, D. R. Reinecke, G. A. Kruger, and W. L. Kiser Jr, "Thermoacoustic ct with radio waves: A medical imaging paradigm," Radiology, vol. 211, no. 1, pp. 275–278, 1999.
- [32] L. V. Wang, X. Zhao, H. Sun, and G. Ku, "Microwave-induced acoustic imaging of biological tissues," Review of scientific instruments, vol. 70, no. 9, pp. 3744–3748, 1999.
- [33] G. Ku and L. V. Wang, "Scanning thermoacoustic tomography in biological tissue," Medical physics, vol. 27, no. 5, pp. 1195–1202, 2000.
- [34] P. M. Meaney, M. W. Fanning, D. Li, S. P. Poplack, and K. D. Paulsen, "A clinical prototype for active microwave imaging of the breast," <u>IEEE Transactions on Microwave Theory and Techniques</u>, vol. 48, no. 11, pp. 1841–1853, 2000.
- [35] P. M. Meaney, K. D. Paulsen, and M. W. Fanning, "Microwave imaging for breast cancer detection: preliminary experience," in <u>SPIE proceedings</u> series. Society of Photo-Optical Instrumentation Engineers, 2000, pp. 308–319.
- [36] A. E. Souvorov, A. E. Bulyshev, S. Y. Semenov, R. H. Svenson, and G. P. Tatsis, "Two-dimensional computer analysis of a microwave flat antenna array for breast cancer tomography," <u>IEEE Transactions on Microwave Theory and Techniques</u>, vol. 48, no. 8, pp. 1413–1415, 2000.
- [37] S. C. Hagness, A. Taflove, and J. E. Bridges, "Two-dimensional fdtd

- analysis of a pulsed microwave confocal system for breast cancer detection: Fixed-focus and antenna-array sensors," <u>IEEE Transactions on Biomedical</u> Engineering, vol. 45, no. 12, pp. 1470–1479, 1998.
- [38] ——, "Three-dimensional fdtd analysis of a pulsed microwave confocal system for breast cancer detection: Design of an antenna-array element," IEEE Transactions on Antennas and Propagation, vol. 47, no. 5, pp. 783–791, 1999.
- [39] C. Gilmore, A. Abubakar, W. Hu, T. M. Habashy, and P. M. van den Berg, "Microwave biomedical data inversion using the finite-difference contrast source inversion method," IEEE Transactions on Antennas and Propagation, vol. 57, no. 5, pp. 1528–1538, 2009.
- [40] P. Mojabi and J. LoVetri, "Microwave biomedical imaging using the multiplicative regularized gauss—newton inversion," <u>IEEE Antennas and Wireless Propagation Letters</u>, vol. 8, pp. 645–648, 2009.
- [41] T. Rubæk, P. M. Meaney, P. Meincke, and K. D. Paulsen, "Nonlinear microwave imaging for breast-cancer screening using gauss—newton's method and the cgls inversion algorithm," <u>IEEE Transactions on Antennas and Propagation</u>, vol. 55, no. 8, pp. 2320–2331, 2007.
- [42] P. J. Gibson, "The vivaldi aerial," in 1979 9th European Microwave Conference, Sep. 1979, pp. 101–105.
- [43] E. Gazit, "Improved design of the vivaldi antenna," <u>IEE Proceedings H Microwaves</u>, Antennas and Propagation, vol. 135, no. 2, pp. 89–92, April 1988.
- [44] M. Abbak, M. Cayoren, and I. Akduman, "Microwave breast phantom measurements with a cavity-backed vivaldi antenna," <u>IET Microwaves, Antennas Propagation</u>, vol. 8, no. 13, pp. 1127–1133, October 2014.
- [45] M. Ostadrahimi, P. Mojabi, S. Noghanian, L. Shafai, S. Pistorius, and J. LoVetri, "A novel microwave tomography system based on the scattering probe technique," <u>IEEE Transactions on Instrumentation and Measurement</u>, vol. 61, no. 2, pp. 379–390, Feb 2012.
- [46] S. Semenov, R. Planas, M. Hopfer, A. Hamidipour, A. Vasilenko, E. Stoeg-

- mann, and E. Auff, "Electromagnetic tomography for brain imaging: Initial assessment for stroke detection," in 2015 IEEE Biomedical Circuits and Systems Conference (BioCAS), Oct 2015, pp. 1–4.
- [47] M. A. Al-Joumayly, S. M. Aguilar, N. Behdad, and S. C. Hagness, "Dualband miniaturized patch antennas for microwave breast imaging," <u>IEEE</u> Antennas and Wireless Propagation Letters, vol. 9, pp. 268–271, 2010.
- [48] M. Lanini, S. Poretti, A. Salvadè, and R. Monleone, "Design of a slim wideband-antenna to overcome the strong reflection of the air-to-sample interface in microwave imaging," in 2015 International Conference on Electromagnetics in Advanced Applications (ICEAA), Sep. 2015, pp. 1020–1023.
- [49] S. Poretti, M. Lanini, A. Salvadè, M. Maffongelli, and R. Monleone, "Antenna design for microwave tomography imaging of high contrast mediums," in 2017 11th European Conference on Antennas and Propagation (EUCAP), March 2017, pp. 1699–1702.
- [50] M. Maffongelli, S. Poretti, A. Salvadè, R. Monleone, C. Pagnamenta, A. Fedeli, M. Pastorino, and A. Randazzo, "Design and experimental test of a microwave system for quantitative biomedical imaging," in 2018 IEEE International Symposium on Medical Measurements and Applications (MeMeA), June 2018, pp. 1–6.
- [51] T. M. Grzegorczyk, P. M. Meaney, P. A. Kaufman, R. M. diFlorio Alexander, and K. D. Paulsen, "Fast 3-d tomographic microwave imaging for breast cancer detection," <u>IEEE Transactions on Medical Imaging</u>, vol. 31, no. 8, pp. 1584–1592, Aug 2012.
- [52] S. K. Padhi, A. Fhager, M. Persson, and J. Howard, "Measured antenna response of a proposed microwave tomography system using an efficient 3-d fdtd model," IEEE Antennas and Wireless Propagation Letters, vol. 7, pp. 689–692, 2008.
- [53] N. Ojaroudi, M. Ojaroudi, and N. Ghadimi, "Uwb omnidirectional square monopole antenna for use in circular cylindrical microwave imaging systems," IEEE Antennas and Wireless Propagation Letters, vol. 11, pp. 1350–1353, 2012.
- [54] A. M. Abbosh, M. E. Bialkowski, and W. C. Khor, "Design of an uwb pla-

- nar monopole antenna for use in a circular cylindrical microwave imaging system," in 2006 International Conference on Microwaves, Radar Wireless Communications, May 2006, pp. 947–950.
- [55] C. Svensson, "Software defined radio vision or reality," in 2006 NORCHIP, Nov 2006, pp. 149–149.
- [56] T. B. Welch, T. Kent, C. H. G. Wright, and M. G. Morrow, "An affordable software defined radio," in 2009 IEEE 13th Digital Signal Processing Workshop and 5th IEEE Signal Processing Education Workshop, Jan 2009, pp. 791–796.
- [57] K. Ma, K. C. B. Liang, J. Zhang, and R. M. Jayasuriya, "2 16ghz microwave synthesizer for wideband software defined radio system," in 2009 European Wireless Technology Conference, Sep. 2009, pp. 226–229.
- [58] Y. Peng, Y. Liu, F. Yang, X. L. Zhang, X. P. Yu, Z. H. Lu, W. M. Lim, and C. H. Hu, "A 100mhz 2ghz wireless receiver in 40-nm cmos for software-defined radio," in 2011 IEEE International Conference of Electron Devices and Solid-State Circuits, Nov 2011, pp. 1–2.
- [59] R. Chen and H. Hashemi, "A 0.5-to-3 ghz software-defined radio receiver using sample domain signal processing," in 2013 IEEE Radio Frequency Integrated Circuits Symposium (RFIC), June 2013, pp. 315–318.
- [60] T. Helaly and N. Adnani, "A new category of software-defined instrumentation for wireless test," in <u>2016 IEEE AUTOTESTCON</u>, Sep. 2016, pp. 1–8.
- [61] —, "A fourth category of software-defined instrumentation for wireless test," <u>IEEE Instrumentation Measurement Magazine</u>, vol. 20, no. 4, pp. 3–10, August 2017.
- [62] J. Marimuthu, K. S. Bialkowski, and A. M. Abbosh, "Software-defined radar for medical imaging," <u>IEEE Transactions on Microwave Theory and Techniques</u>, vol. 64, no. 2, pp. 643–652, Feb 2016.
- [63] A. E. Stancombe, K. Bialkowski, and A. Abbosh, "Portable microwave head imaging system using software-defined radio and switching network," IEEE Journal of Electromagnetics, RF and Microwaves in Medicine and

- Biology, pp. 1–1, 2019.
- [64] B. Bogert, "Demonstration of delay distortion correction by time-reversal techniques," <u>IRE Transactions on Communications Systems</u>, vol. 5, no. 3, pp. 2–7, December 1957.
- [65] K. E. Schreiner, H. L. Funk, and E. Hopner, "Automatic distortion correction for efficient pulse transmission," <u>IBM Journal of Research and Development</u>, vol. 9, no. 1, pp. 20–30, Jan 1965.
- [66] F. Wu, J. . Thomas, and M. Fink, "Time reversal of ultrasonic fields. il. experimental results," <u>IEEE Transactions on Ultrasonics</u>, Ferroelectrics, and Frequency Control, vol. 39, no. 5, pp. 567–578, Sep. 1992.
- [67] M. Fink, C. Prada, F. Wu, and D. Cassereau, "Self focusing in inhomogeneous media with time reversal acoustic mirrors," in <u>Proceedings., IEEE</u> Ultrasonics Symposium,, Oct 1989, pp. 681–686 vol.2.
- [68] N. Chakroun, M. A. Fink, and F. Wu, "Time reversal processing in ultrasonic nondestructive testing," <u>IEEE Transactions on Ultrasonics</u>, <u>Ferroelectrics</u>, and <u>Frequency Control</u>, vol. 42, no. 6, pp. 1087–1098, Nov 1995.
- [69] G. Lerosey, J. de Rosny, A. Tourin, A. Derode, G. Montaldo, and M. Fink, "Time reversal of electromagnetic waves," Phys. Rev. Lett., vol. 92, p. 193904, May 2004. [Online]. Available: https://link.aps.org/doi/10.1103/PhysRevLett.92.193904
- [70] Kyritsi, Papanicolaou, Eggers, and Oprea, "Miso time reversal and delay-spread compression for fwa channels at 5 ghz," <u>IEEE Antennas and Wireless Propagation Letters</u>, vol. 3, pp. 96–99, 2004.
- [71] D. Liu, G. Kang, L. Li, Y. Chen, S. Vasudevan, W. Joines, Q. H. Liu, J. Krolik, and L. Carin, "Electromagnetic time-reversal imaging of a target in a cluttered environment," <u>IEEE Transactions on Antennas and Propagation</u>, vol. 53, no. 9, pp. 3058–3066, Sep. 2005.
- [72] A. J. Devaney, "Time reversal imaging of obscured targets from multistatic data," <u>IEEE Transactions on Antennas and Propagation</u>, vol. 53, no. 5, pp. 1600–1610, May 2005.

- [73] L. Li, W. Zhang, and F. Li, "A novel autofocusing approach for real-time through-wall imaging under unknown wall characteristics," IEEE Transactions on Geoscience and Remote Sensing, vol. 48, no. 1, pp. 423–431, Jan 2010.
- [74] S. M. Moghadasi and M. Dehmollaian, "Buried-object time-reversal imaging using uwb near-ground scattered fields," <u>IEEE Transactions on Geoscience and Remote Sensing</u>, vol. 52, no. 11, pp. 7317–7326, Nov 2014.
- [75] P. Kosmas and C. M. Rappaport, "Time reversal with the fdtd method for microwave breast cancer detection," <u>IEEE Transactions on Microwave Theory and Techniques</u>, vol. 53, no. 7, pp. 2317–2323, July 2005.
- [76] ——, "Fdtd-based time reversal for microwave breast cancer detection-localization in three dimensions," IEEE Transactions on Microwave Theory and Techniques, vol. 54, no. 4, pp. 1921–1927, June 2006.
- [77] M. D. Hossain and A. S. Mohan, "Breast cancer detection in highly dense numerical breast phantoms using time reversal," in 2013 International Conference on Electromagnetics in Advanced Applications (ICEAA), Sep. 2013, pp. 859–862.
- [78] S. Mukherjee, "A hybrid electromagnetic imaging system for nde and biomedical applications," Ph.D. dissertation, 2018, copyright Database copyright ProQuest LLC; ProQuest does not claim copyright in the individual underlying works; Last updated 2018-07-09. [Online]. Available: http://ezproxy.msu.edu.proxy1.cl.msu.edu/login?url=https://search-proquest-com.proxy1.cl.msu.edu/docview/2061619242? accountid=12598
- [79] A. F. Peterson, S. L. Ray, and R. Mittra, Computational methods for electromagnetics. IEEE press New York, 1998, vol. 24.
- [80] S. Mukherjee, L. Udpa, S. Udpa, and E. J. Rothwell, "Target localization using microwave time-reversal mirror in reflection mode," <u>IEEE Transactions on Antennas and Propagation</u>, vol. 65, no. 2, pp. 820–828, Feb 2017.
- [81] K. Yee, "Numerical solution of initial boundary value problems involving maxwell's equations in isotropic media," <u>IEEE Transactions on Antennas</u>

- and Propagation, vol. 14, no. 3, pp. 302–307, May 1966.
- [82] R. Courant, K. Friedrichs, and H. Lewy, "On the partial difference equations of mathematical physics," IBM Journal of Research and Development, vol. 11, no. 2, pp. 215–234, March 1967.
- [83] G. Mur, "Absorbing boundary conditions for the finite-difference approximation of the time-domain electromagnetic-field equations," <u>IEEE Transactions on Electromagnetic Compatibility</u>, vol. EMC-23, no. 4, pp. 377–382, Nov 1981.
- [84] J.-P. Berenger, "A perfectly matched layer for the absorption of electromagnetic waves," <u>Journal of Computational Physics</u>, vol. 114, no. 2, pp. 185 200, 1994. [Online]. Available: http://www.sciencedirect.com/science/article/pii/S0021999184711594
- [85] J. A. Roden and S. D. Gedney, "Efficient implementation of the uniaxial-based pml media in three-dimensional nonorthogonal coordinates with the use of the fdtd technique," Microwave and Optical Technology Letters, vol. 14, no. 2, pp. 71–75, 1997. [Online]. Available: https://onlinelibrary.wiley.com/doi/abs/10.1002/%28SICI%291098-2760%2819970205%2914%3A2%3C71%3A%3AAID-MOP1%3E3.0.CO%3B2-I
- [86] J. Alan Roden and S. Gedney, "Convolution pml (cpml): An efficient fdtd implementation of the cfs-pml for arbitrary media," Microwave and Optical Technology Letters, vol. 27, pp. 334–339, 12 2000.
- [87] X. Xu, E. L. Miller, and C. M. Rappaport, "Minimum entropy regularization in frequency-wavenumber migration to localize subsurface objects," <u>IEEE Transactions on Geoscience and Remote Sensing</u>, vol. 41, no. 8, pp. 1804–1812, 2003.